# DIRECT POWDER ROLL COMPACTION OF α- β TITANIUM ALLOYS WITH Al, V, and Fe

by

Shannon Cathleen Clemens

Submitted in partial fulfilment of the requirements for the degree of
Master of Applied Science

at

Dalhousie University
Halifax, Nova Scotia
July 25th 2022

**TABLE OF CONTENTS**

# List of Tables

# List of Figures

# ABSTRACT

Compared to other metals, titanium has good corrosion and oxidation resistance, strength-weight ratio, and retains strength at relatively high temperatures. Despite being an excellent engineering material, its cost of production using the traditional methods is prohibitive. This work explores direct powder rolling (DPR) as an alternative production method for two titanium alloys with target compositions of Ti-6Al-4V and Ti-5Al-2.5Fe, using low-cost Ti powder.

Grain size, composition, and oxygen content were determined to be the most influential factors in determining the mechanical properties of the strip which negatively impacted the ability to conclusively compare effects of the rolling path variations. DPR was used to create near full density strips with tensile and hardness properties comparable to the wrought Ti-6Al-4V counterparts cold rolled via the same roll path. With further development, DPR has the potential to produce titanium strip while being more cost effective and less energy intensive than the current methods.

Keywords: Titanium Alloys, Powder Metallurgy, Direct Roll Compaction, Ti-6Al-4V, Ti-5Al-2.5Fe, Aluminium, Iron, Vanadium, Cold Rolling, Sheet, Sintering

# List of Symbols and Abbreviations

| | |
|---|---|
| $\alpha$ | Alpha |
| $\alpha'$ | Alpha prime (hexagonal martensitic microstructure) |
| $\beta$ | Beta |
| °C | Degrees Celsius |
| $\varepsilon$ | Engineering strain |
| $\varepsilon_{true}$ | True strain |
| $\mu$ | Coefficient of friction |
| $\rho_s$ | Density of sample |
| $\rho_w$ | Density of distilled water |
| $\sigma$ | Engineering stress |
| $\sigma_{true}$ | True stress |
| $\sigma_{0.2\%}$ | Proof stress, 0.02% offset yield stress |
| $\Theta$ | Nip angle (or grip angle) |
| ± | Plus or minus |
| | |
| A | Cross sectional area |
| a | Particle radius |
| ASTM | American Society for Testing and Materials |
| at% | Atomic percentage |
| b | Length of grip section |
| BCC | Base centered cubic |
| BE | Blended elemental |

| | |
|---|---|
| BTT | Beta transus temperature |
| c | Length of reduced parallel section |
| CIP | Cold isostatic pressing |
| CP | Commercially pure |
| d | Width of grip section |
| $d_{50}$ | Median particle size |
| DIL | Dilatometry |
| DPR | Direct powder rolling |
| DSC | Differential scanning calorimetry |
| E | Modulus of elasticity |
| EDS | Energy dispersive X-ray spectroscopy |
| F | Applied force |
| FEM | Finite element modeling |
| f | Radius of fillet |
| g | Gauge length |
| GF | Green feeder |
| GPa | Gigapascal |
| GS | Grain size |
| GW | Gap width |
| h | Sample height |
| HCP | Hexagonal closed packed |
| HDH | Hydride-dehydride |
| HTTAL | High Temperature Thermal Analysis Laboratory |

| | |
|---|---|
| HV | Vickers hardness |
| K | Strength coefficient |
| K | Degrees Kelvin |
| kN | Kilonewton |
| L | Contact length |
| LA-ICPMS | Laser ablation inductively coupled mass spectroscopy |
| l | Overall tensile length |
| $M_a$ | Apparent mass in air |
| $M_w$ | Apparent mass in water |
| MA | Master alloy |
| MJ | Megajoule |
| MIM | Metal injection molding |
| MPa | Megapascal |
| n | Strain hardening coefficient |
| N | Newton |
| p | Applied pressure |
| $P_{EQ}$ | Equilibrium vapor pressure |
| PM | Powder metallurgy |
| P&S | Press & sinter |
| PSD | Powder size distribution |
| $Q_P$ | Pressure multiplication factor, homogeneous |
| $Q_i$ | Pressure multiplication factor, inhomogeneous |
| R | Roll radius |

| | |
|---|---|
| RC | Roll compaction |
| RPM | Revolutions per minute |
| S+A | Sinter + anneal |
| SEM | Scanning electron microscopy |
| SLPS | Solid liquid phase sintering |
| SO | Sintered only |
| SSS | Solid state sintering |
| $t_i$ | Initial sheet thickness |
| $t_f$ | Final sheet thickness |
| $\Delta t$ | Draft (change in sheet thickness) |
| $v_i$ | Initial sheet velocity |
| $v_f$ | Final sheet velocity |
| $v_r$ | Roll velocity |
| USD | United States Dollars |
| UTS | Ultimate Tensile Strength |
| VAR | Vacuum arc remelting |
| W | Sheet width |
| w | Width of reduced section |
| wt% | Weight percentage |
| x | Neck size (between particles) |
| $\overline{Y}$ | Flow stress |
| YS | Yield Strength |

# Acknowledgements

Firstly, I would like to thank Dr. Stephen Corbin for teaching me the fundamentals of materials years ago and sparking my curiosity for materials engineering research that has led me here. Thank you for being an excellent graduate supervisor and mentor, inspiring me to always search for the answers, and guidance for when those answers lead to more questions.

I would like to acknowledge the researchers who have helped me throughout the course of this project, particularly Randy Cooke for his assistance with tensile and OHN testing, Owen Craig for his assistance with hardness testing, and Patricia Scallion for assistance in obtaining SEM images. I would like to acknowledge Julian O'Flynn and Hannah Kaufman for their previous work with titanium roll compaction without which, this research would not be possible. I would like to thank Addison Rayner for helping me with research advice, troubleshooting lab equipment, and being an excellent office mate. Thank you also to my supervisory committee Dr. Paul Amyotte and Dr. Paul Bishop.

Finally, I would like to thank my parents Geraldine Carlin and David Clemens, for unwavering support and encouragement.

# Chapter 1: Introduction

Titanium is the ninth most abundant element on earth, greater than chromium, nickel, and copper. Titanium, however, is often found in minerals from which extraction is not economical so high production costs are associated with final part production [1]. Figure 1-1 compares the strength and density of materials; titanium alloys have relatively high strength with only a moderate density when compared to other classes of alloys. Having high strength-to-weight ratios, good corrosion resistance and ductility, titanium and its alloys have found many useful engineering applications. However their high production costs have limited regular usage to aerospace, biomedical, and chemical industries [1], [2].

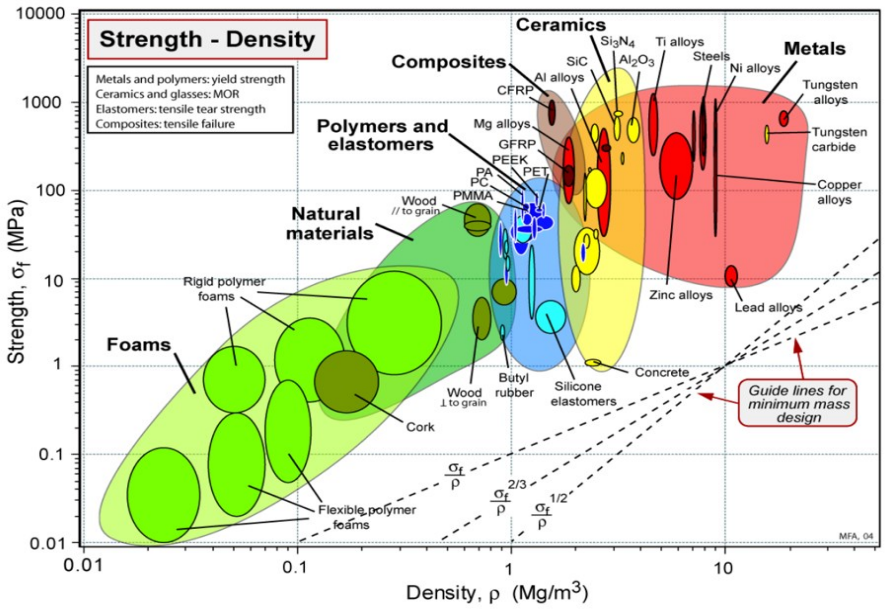


*Figure 1-1. CES Edupack comparison of strength and density [3]*

Embodied energy is a common metric used in the discussion of economic and environmental effects of a material's production; it is the energy which is required to

produce 1kg of the material. Figure 1-2 is a schematic of the traditional processing route beginning with titanium ore through the final production of a fully manufactured part. To the right of each step in the process, the estimated embodied energy and cost in USD circa 2004 is given [4].

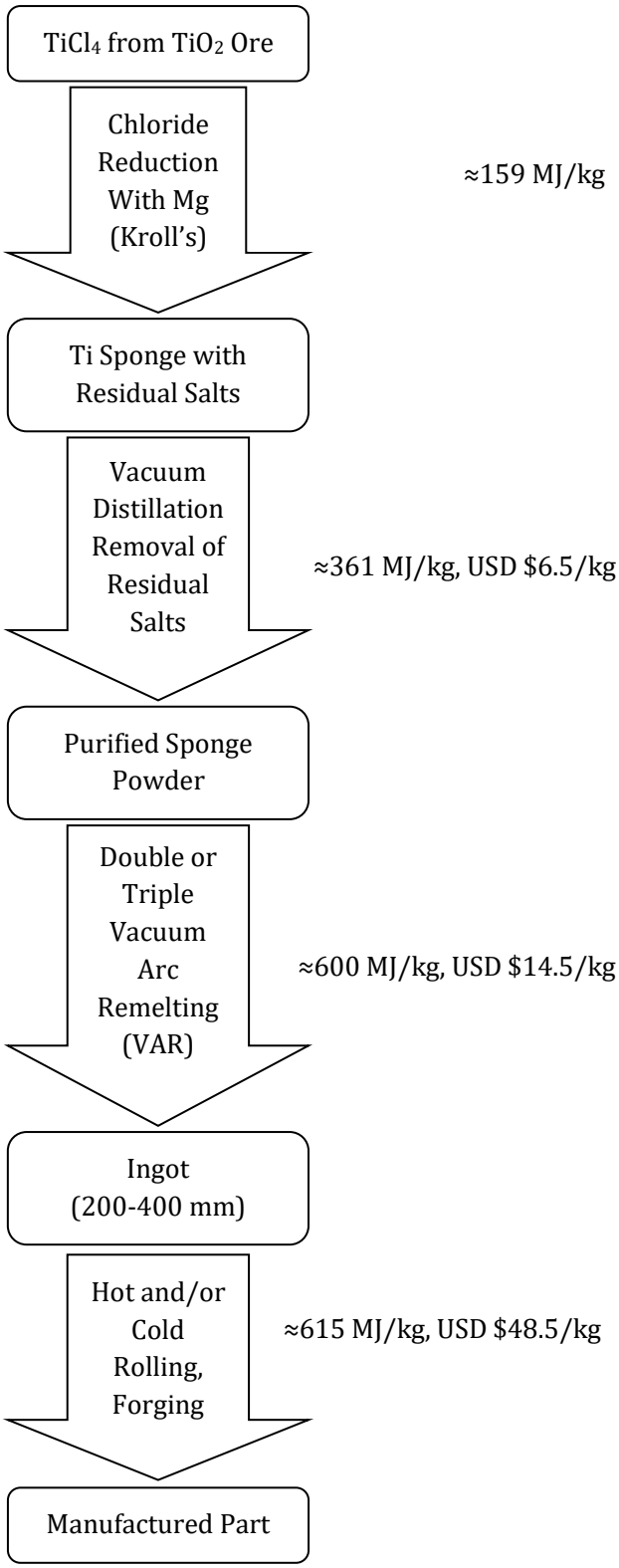


*Figure 1-2. Schematic of traditional titanium processing route with embodied energy and cost in USD circa 2004 [4]*

Figure 1-3 below compares the $CO_2$ footprint and embodied energy of primary production for a variety of materials. The metal and alloy class of materials have the highest embodied energy and $CO_2$ production.

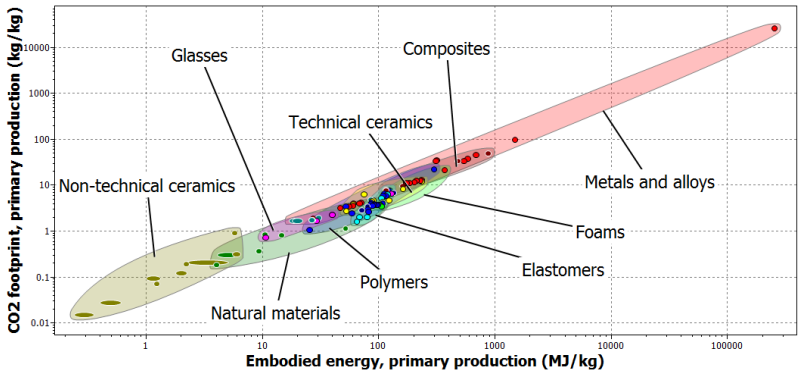


*Figure 1-3. CES Edupack Material Selection diagram comparing $CO_2$ footprint and embodied energy of various materials [5]*

A closer examination of the embodied energy-$CO_2$ footprint relationship for metallic materials in Figure 1-4 shows that cost and energy required per kilogram of titanium production via traditional methods is on the higher end of the scale compared to the other alloys. It is greater than several steel, aluminium, magnesium, and nickel super-alloys.

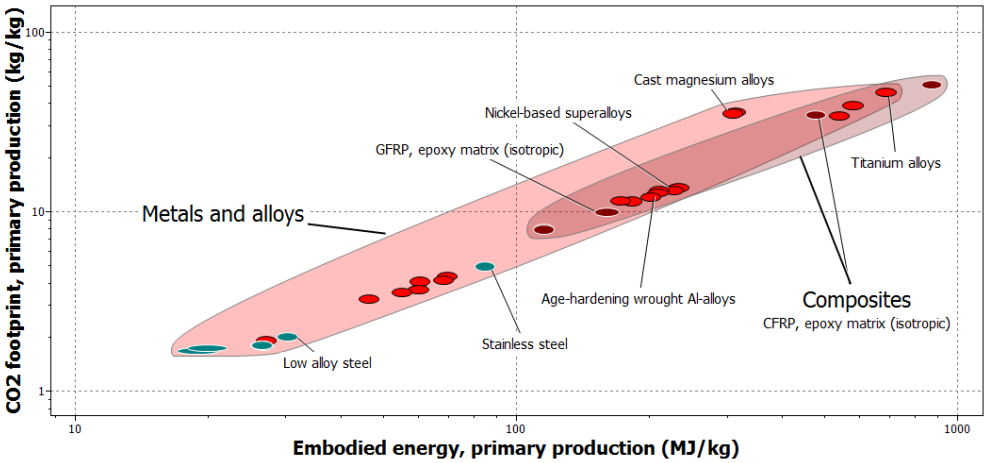


*Figure 1-4. CES Edupack Material Selection diagram comparing $CO_2$ footprint and embodied energy with a focus on metals and alloys [5]*

Despite the engineering benefits described earlier, the high cost of titanium is prohibitive for its use in many industries in addition to its undesirable $CO_2$ footprint. If these disadvantages could be addressed, potential areas for expansion include corrosion protection panels, fuel cell separators, condenser tubes, and heat exchange panels [6], [7].

Most noted, the transportation and aerospace industries could significantly benefit from lower costs of titanium production, where there is significant potential to decrease energy efficiency in two ways: firstly, service life of components in transportation, among other industries can be maximized by using material with improved properties. This reduces energy consumption related to remanufacturing of replacement parts in addition to decreasing downtime. Secondly, energy efficiency can be increased by reducing vehicle weight. Reducing the vehicle weight by 10% can result in a 6-8% reduction in fuel consumption [8]. Topology optimization using Finite Element Modeling (FEM) to eliminate material, which is not stress bearing from the design, is the first step in light weighting but has limitations. After this is complete, the only way to further reduce the weight is changing the materials from which the components are made [8]. With its abundance and good mechanical and anti-corrosion properties, it is desirable to find alternative, lower cost production methods which would allow for more wide-spread usage of titanium in transportation and other industries. From Figure 1-2, the highest cost and most energy intensive steps in the traditional Ti processing route are the Vacuum Arc Remelting (VAR) and rolling steps [4]. The following proposed route in Figure 1-5 replaces these steps with an alternative process called Direct Powder Rolling (DPR) [9]–[12].

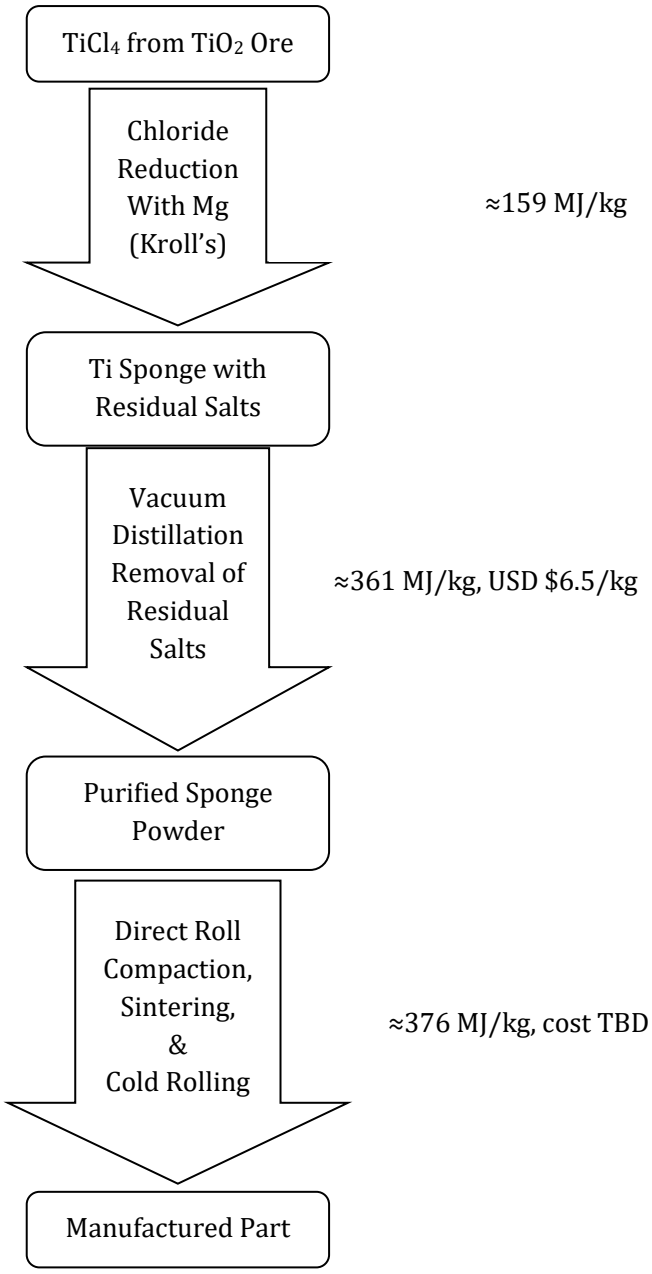


*Figure 1-5. Schematic of proposed alternative processing route for titanium sheets [4]*

Although the cost of commercial production has not yet been thoroughly analysed, there is a notable reduction in the amount of energy which would be required to produce titanium sheets via DPR. The mechanics of each step are discussed in later sections, however, the reasons for cost and energy savings can be summarized here. Firstly, the morphology of the purified sponge powder is desirable for the DPR process

unlike many powder metallurgy methods and does not require additional processing. Secondly, there is a significant difference in the initial thickness prior to rolling. In the traditional Ti processing method, the starting thickness of an ingot before the rolling steps ranges from 200-400 mm. This requires a combination of many hot rolling passes and/or cold rolling and heat treatment to achieve reductions to final heights of 0.5 mm or less, whereas the DPR process produces a strip with a starting thickness of 1-2 mm which is then further processed into the final sheet.

The open literature regarding titanium roll compaction is currently limited, especially regarding cold rolling procedures and alloys other than CP-Ti. A market review of DPR of titanium performed by Steytler and Knutsen has concluded that the current processes are not marketable commercially, particularly due to their failure to meet requirements for elongation and minimum oxygen content but could potentially with improvements to powder or DPR technologies. Cost per kg of wrought Titanium sheet was also examined in the 2020 review; above 1mm thickness, the cost per kg is relatively stable at $100-150/kg. As the sheet thickness is reduced, the cost increases exponentially reaching prices >$1000/kg due to the extensive cold rolling and annealing required [9]. The reduction in cold rolling involved in the DPR process could greatly reduce this cost. The current work seeks to address gaps in literature regarding DPR of titanium alloys, examine the potential of creating strips via DPR which satisfy required material properties of the alloys.

# Chapter 2: Background

## 2.1 Titanium and Its Alloys

At room temperature, pure titanium has a hexagonal closed packed (HCP) structure called α-Ti. At 882.5°C, titanium experiences an allotropic phase transformation and α-Ti transitions to a body centred cubic (BCC) structure called β-Ti; the temperature at which the α-β transformation takes place is known as the β transus temperature (BTT). The three determing factors of a titanium alloy's microstructure at room temperature are chemical composition, processing history, and thermal treatment.

### 2.1.1 Chemical Composition

Pure titanium transforms at 882.5°C, however alloying elements will alter the BTT by stabilizing either the α or β phase. Non-transition metals are generally α-stabilizing elements, increasing the BTT. Conversely, transition metals are generally β-stabilizing elements, which can be divided into two categories, isomorphous and eutectoid, both of which lower the BTT. The differentiation between isomorphous and eutectoid β-stabilizing elements is related to their solubility in titanium. The effects of alloying elements on the titanium phase diagram are summarized in Figure 2-1.

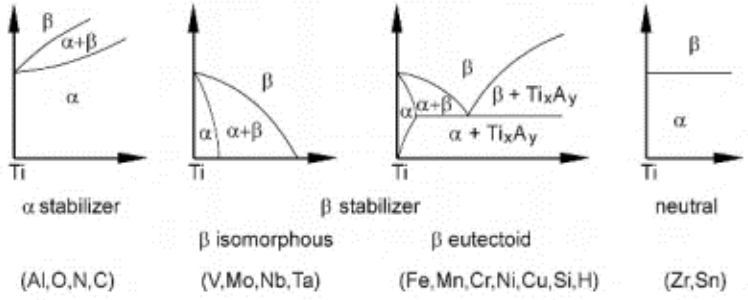


*Figure 2-1. Schematic summarizing the four possible effects of an element on the BTT of a titanium alloy [13]*

Titanium alloys are often described in terms of Al equivalents of α-stabilizing elements and Mo equivalents of β-stabilizing elements, given by the following equations [14]:

$$[Al]_{eq} = [Al] + \frac{[Zr]}{6} + \frac{[Sn]}{3} + 10[O] \quad (1)$$

$$[Mo]_{eq} = [Mo] + \frac{[Ta]}{5} + \frac{[Nb]}{3.6} + \frac{[W]}{2.5} + \frac{[V]}{1.5} + 1.25[Cr] + 1.25[Ni] + 1.7[Mn] + 1.7[Co] + 2.5[Fe] \quad (2)$$

The critical concentration of Mo or equivalent to retain β-Ti at room temperature is 10 wt% [14]. Titanium alloys may be classified as α, near α, α+β, metastable β, and stabilized β based on their microstructure, which effects the mechanical properties of the material.

Ti-6Al-4V is the most widely used titanium alloy at over 50% of the titanium market [14], [15]. It is often used in biomedical applications, however vanadium being classified as a toxic biometal, its presence in the Ti-6Al-4V alloy has been cited as potentially leading to adverse reactions in a patient's body [16]–[18]. In conjunction with alternate processing routes, alloy design is another avenue which is being explored to lower the cost of titanium alloys while maintaining or improving material properties. Replacement of vanadium, an isomorphous β-stabilizer with eutectoid β-stabilizers such as iron must be done cautiously as eutectoid elements can result in the formation of intermetallic compounds which reduces the ductility of the material. Despite this, Ti-xAl-yFe has been explored as a lower cost alternative with higher biocompatibility and a similar phase distribution [17], [19]. It is very economical compared to other β-stabilizing elements and has a stong β-factor, meaning that less

iron would need to be added compared to other elements to achieve the same stabilizing effect. Further, iron has excellent diffusivity in titanium [19].

When Fe contents of 1-5 wt% were studied by Sjafrizal et al., it was determined that the Ti-6Al-3Fe yielded the most productive balance of high strength and low modulus. Sintering response, microstructure, and mechanical properties were considered [17]. The current work will study two α+β alloys; Ti-6Al-4V, which the most widely used Ti-alloy and Ti-5Al-2.5Fe.

### 2.1.2 Effects of Processing on Microstructures of Ti-6Al-4V

Figure 2-2 compares the microstructures of water quenched, air and furnaced cooled Ti-6Al-4V.

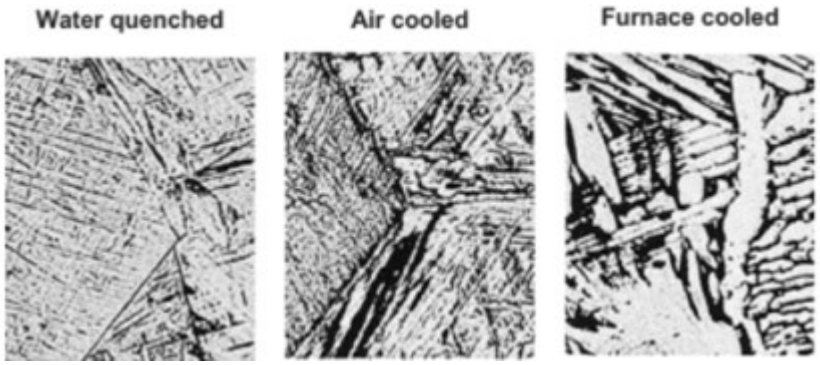


*Figure 2-2. Comparison of Ti-6Al-4V microstructure solutionized at 1065°C and cooled at various rates via water, air, and furnace [1]*

#### *2.1.2.1 Water Cooling*

Titanium, when cooled at a fast rate of speed results in a hexagonal martensitic microstructure (α') via a diffusionless transformation mechanism similar to steels and with a similar appearance. Prior β-grain boundaries are visible, within which the fine basketweave structure is present.

*2.1.2.2 Air Cooling*

When cooling at an intermediate rate, such as air, from a solutionizing temperature above the BTT, an acicular α-Ti is observed. At the α-β transition, α grains nucleate at the prior β grain boundaries and grow along preferential planes yielding a basketweave morphology as in Figure 2-3, commonly referred to as a Whidmanstätten microstructure. When cooling rate is fast, but the rate is not fast enough to induce formation of α', or the composition of the alloy is such that the martensitic transformation temperature is below room temperature, some β-Ti can be retained at room temperature [20].

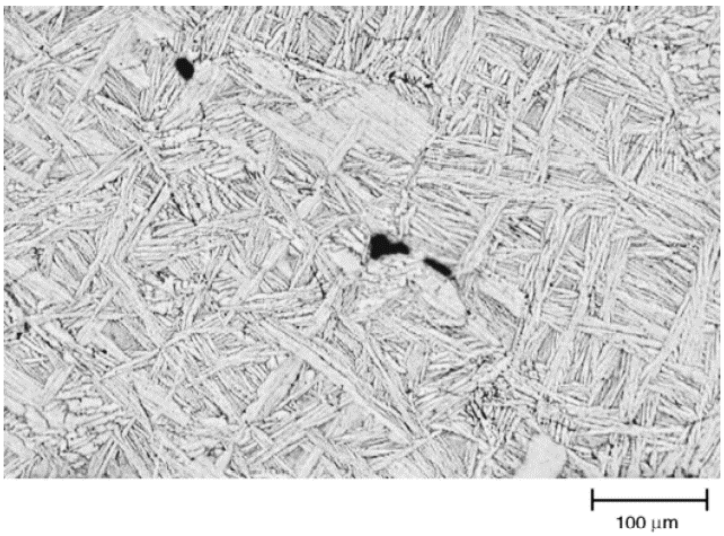


*Figure 2-3. Micrographs of slowly cooled Ti-6Al-4V etched with Kroll's reagent [21]*

While the acicular α and α' do appear similar, the *ASTM Handbook on Selection and Properties of Non-Ferrous Alloys* notes that α' may be differentiated from acicular α-Ti by the more curved edges and greater definition [20].

*2.1.2.3 Furnace Cooling*

At slowest cooling rates, as in furnace cooling, the α-Ti microstructure becomes platelike with retained β-Ti between the α-Ti plates. In Figure 2-4 below, the α-Ti

appears as a light grey when etched with Kroll's reagent, while the β-Ti at the grain boundaries appear as a dark grey. Slower cooling rates favor the mechanics of grain growth rather than grain nucleation; slower cooling rates result in larger distances between plates and larger colonies of α-Ti.

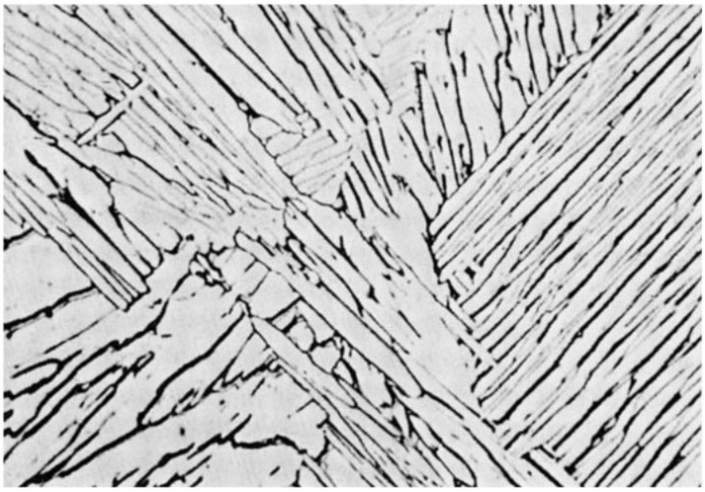

*Figure 2-4. Micrograph of Ti-6Al-4V cooled slowly from above the BTT [1], micrograph obtained at 500x magnification*

### 2.1.3 Microstructures of Ti-5Al-2.5Fe

The microstructure of Ti-5Al-2.5Fe reported in literature presented in Figure 2-5, is similar to that of Ti-6Al-4V in Figure 2-4. The matrix is primarily α-Ti, with β-Ti at the grain boundaries. This micrograph was obtained from a BE powder mixture sintered for 30 minutes at 950°C under vacuum atmosphere [22]. In a separate study, a BE Ti-5Al-2.5Fe mixture had sintering parameters of 1250°C for 2 hours, also under vacuum atmosphere [23]. The resultant microstructure is shown in Figure 2-6. The lamellar α-β structure remains; however, the plate thickness is more homogeneous as the sintering times are longer and temperatures are elevated, promoting greater diffusion.

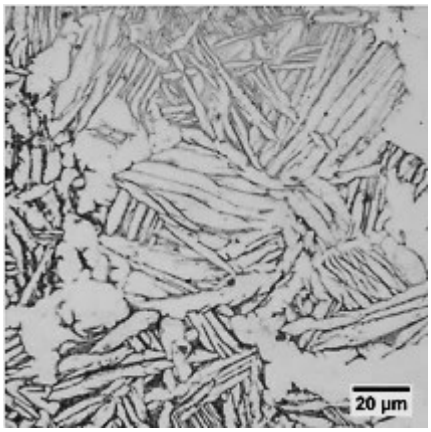


*Figure 2-5. Micrograph of Ti-5Al-2.5Fe obtained from Yamanoglu et. al [22]*

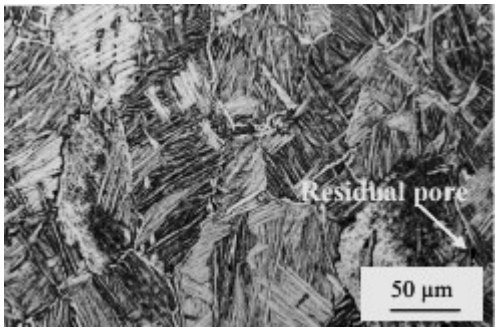


*Figure 2-6. Micrograph of Ti-5Al-2.5Fe from Jia et al. [23]*

Examining the effect of sintering temperature on Ti-5Al-2.5Fe alloy at higher magnifications, the following sequence in Figure 2-7 shows the evolution of iron

particles when sintered for 2 hours at various temperatures as reported by Siqueira et al. In these Scanning electron microscopy (SEM) images, the iron appears as bright white and residual non-reacted aluminium at lower temperatures are dark, cloudy regions. The titanium matrix as shades of grey under backscatter imaging.

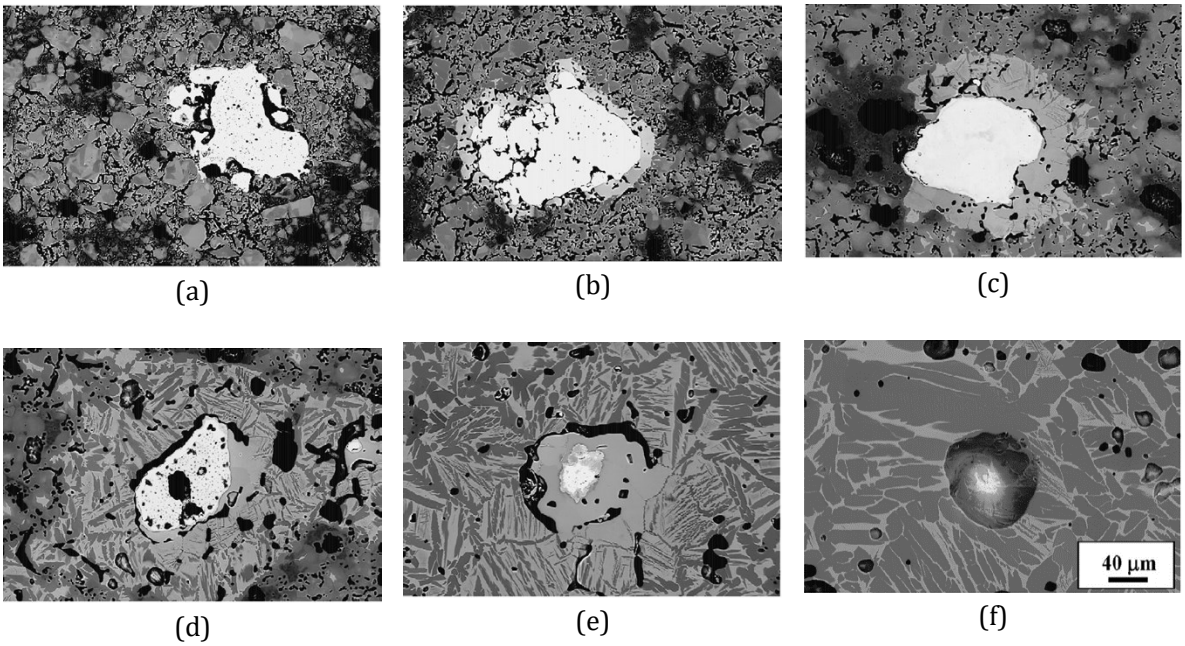


*Figure 2-7. SEM images of blended elemental Ti-5Al-2.5Fe from Siqueira et al. [24] sintered at various temperatures for 2 hours (a) 700°C (b) 800°C (c) 900°C (d) 1000°C (e) 1100°C (f) 1200°C*

As expected, the dissolution of iron is more effective at higher temperatures. As the alloying elements aluminium and iron stabilize alpha and beta respectively, β-Ti appears lighter grey and α-Ti darker in the SEM.

### 2.1.4 Mechanical properties

As with microstructure, the mechanical properties are also dependent on material processing. As literature regarding titanium roll compaction is not widely available, a collection of mechanical values has been formed from literature for both of the selected alloys processed by a variety of methods. The following Table 2-1 and Table 2-2 present hardness and tensile properties respectively.

*Table 2-1. Collection of hardness values for selected alloys from literature*

| Alloy | Processing | HV | Source |
|---|---|---|---|
| **Ti-6Al-4V** | Annealed grade 5 | 349 | [20] |
| **Ti-5Al-2.5Fe** | Vacuum sintered, BE powder alloy | 268 | [22] |

*Table 2-2. Collection of tensile properties for selected alloys from literature*

| Alloy | Processing | Yield Strength (MPa) | UTS (MPa) | Elongation (%) | Source |
|---|---|---|---|---|---|
| **Ti-6-4** | As-cast | 896 | 1000 | 8 | [20] |
| | Unidirectionally rolled sheet from ingot, 0.737mm | 945 | 870 | 7 | [1] |
| | BE P&S at 98% density | 827 | 896 | 12 | [20] |
| | Sponge fines + Al:V MA, P&S | 868 | 945 | 15 | [25] |
| | Wrought mill annealed | 923 | 978 | 16 | [25] |
| **Ti-5-2.5** | BE PS 1250°C 2h vac | 710 | 812 | 0.7 | [23] |
| | BE P&S 1250°C 2h vac + forging | 947 | 1020 | 4.2 | |
| | Mill annealed | 996 | 1068 | 11 | |

The small elongation of 0.7% measured In Ti-5Al-2.5Fe by Jia et al. in a press and sinter compact is attributed to residual porosity in the samples and improves to 4.2% in the same material after forging. Other properties of yield strength (YS) and Ultimate Tensile Strength (UTS) are also improved by forging and are comparable to the ranges observed in variations of Ti-6Al-4V.

## 2.2 Roll Compaction

While powder metallurgy technologies may be implemented for a wide variety of metals, it is particularly useful for those which are refractory or reactive and materials for which parts cannot easily or economically be produced by conventional fusion (casting) processes. Powder metallurgy may be used to create unique alloys, porous metals, composite materials such as cermets and cemented carbides which are also not producible by fusion due to segregation. In addition to the unique capabilities of PM, it is also an economical production method in many cases due to the near-net shape components produced. The high precision of the process reduces further costs associated with machining time and tools, as well as lowers material costs with only a small percentage of the material being lost as waste [26].

Roll compaction is a PM process wherein material is consolidated by rollers to a continuous sheet. A schematic of a continuous roll compaction process is given in Figure 2-8. Metal powder flows from a hopper to the shaping rolls which produces a green strip, generally having a density of approximately 80-85%. This process can be performed at room or elevated temperatures. From the rolls, the green sheet material flows through a sintering furnace where heat is used to further consolidate the powder, which increases the strength of the strip and may also remove some surface oxide impurities. [27], [28]. The sintering mechanism discussed in greater detail in Section 0. From the sintering furnace, additional processing may be performed such as cold rolling as will be examined in the current work, or hot rolling as shown in the schematic.

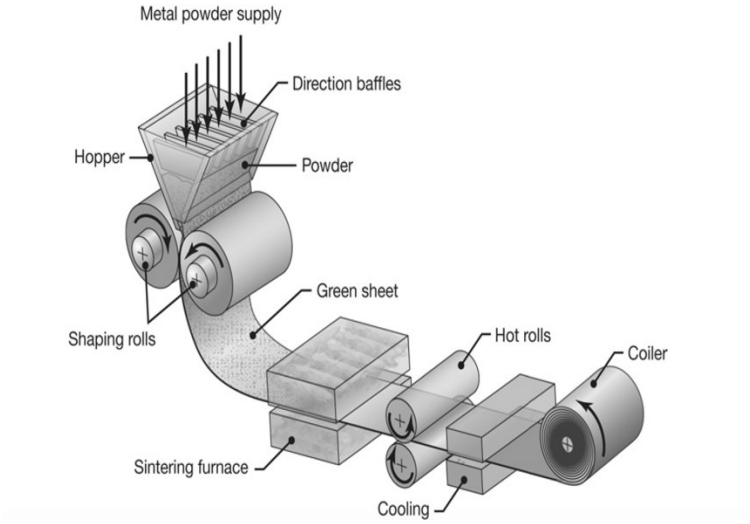


*Figure 2-8. Schematic of the continuous roll compaction process [27]*

The resultant microstructure, and therefore the mechanical properties are dependent on the processing route [7]. Initial exploration of the roll compaction process occurred between the years of 1843-1938 by a number of researchers using converted horizontal rolling mills. Since then, it has been determined that vertical roll compaction is preferable as the powder supply is either assisted or entirely controlled by gravitational forces. A saturated feed is one where the frictional forces between the rolls and powder particles, as well as the flow properties, are limiting the amount of powder fed to the rolls. When additional controls are implemented to limit the amount of powder which is being compacted, the feed is unsaturated. Conversely, screw systems can be implemented to increase the amount of powder fed to the system compared to a saturated feed which operates using gravitational forces alone [28].

### 2.2.1 Roll Compaction Zones

Powder passes through four zones during the roll compaction process: (a) the free flow, (b) feed, (c) compaction, and (d) deformation zones. A schematic of these zones relative to the rolls is given in Figure 2-9 below. The free flow zone is where powder

falls by gravitational forces. The following feed zone is where the powder is pulled by friction with rolls rather than gravity. No deformation of particles occurs at this stage; however, densification may begin as particles rearrange to achieve a higher packing density. In the third zone, compaction begins, and the powder particles form a coherent strip. The final zone of roll compaction is deformation and is cited as the step which produces the green strength of the strip. Compaction and deformation zones often overlap [28].

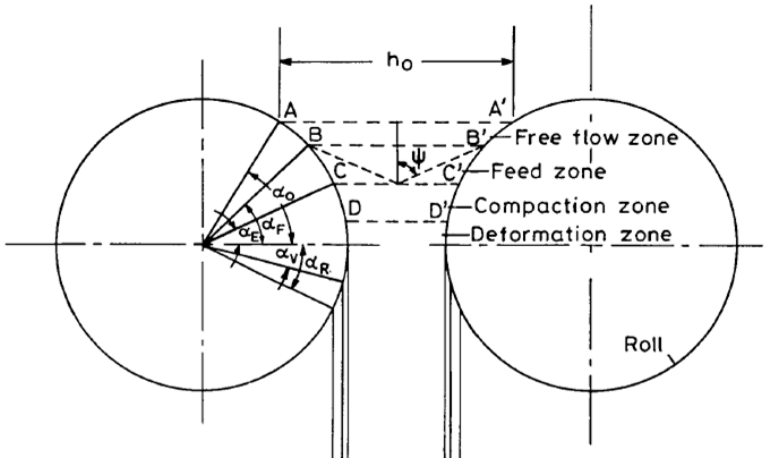


*Figure 2-9. Schematic of roll compaction zones [28]*

The nip angle, (also called grip angle in some literature) is shown as $\alpha_F$ in Figure 2-9 but is referred to as Θ through the duration of this writing; Θ is measured from the end of the feed zone to the neutral plane. The neutral plane (also referred to as neutral plane and no-slip point) is the point in the system at which the strip velocity is equal to the roll velocity [27]. Dube estimates this angle to be approximately 7-8° in roll compaction [28].

### 2.2.2 Effect of Rolling Parameters

This section discusses the general effects of different system parameters that can be varied and the powder properties on the roll compaction process.

#### *2.2.2.1 Rolls*

Larger rolls produce strips with a greater thickness as more powder can be pulled into the nip region. Using ridged or roughened rolls increases the friction between the rollers and the powder, which also increases the amount of powder which can be drawn into the nip region. The gap width (GW) is the space between the rollers; larger GW produces thicker green compacts. A maximum thickness does exist for a set of conditions, over which a coherent strip cannot be produced [28].

#### *2.2.2.2 Roll Force*

Increasing applied force has been found to decrease sheet thickness and increase density; this effect was found to be more prominent when increasing from low to intermediate forces compared to increasing from intermediate to high forces [29].

#### *2.2.2.3 Roll Speed*

The density of produced green strips remains relatively constant at lower ranges of roll speeds. There is a point called the transition speed, at which point the density and other properties of the strip begin to decrease. It is hypothesized that lower density strips are produced when using faster roll speeds since the material is subjected to pressure for a shorter amount of time.

Further, the roll speed must be optimized in conjunction with the powder feed rate. In addition to ensuring an adequate amount of powder is present and able to be drawn into the nip region of the rollers, a fluidization of particles also occurs. This effect occurs during compaction as air is pressed from the compaction region, backwards through the powder bed. As roll speed is increased, so does fluidization. A number of methods have been found to mitigate the effects such as rolling under vacuum or gas

atmospheres having lower viscosity than air such as hydrogen or argon, however, these are not viable on an industrial scale continuous roll compaction process [28].

### 2.2.3 Effect of Powder Properties

In roll compaction, as in all powder metallurgy processes, both size distribution and shape of the particles impact the compactability and flowability of the powder, which in turn affect the mechanical and physical properties of the produced component.

#### *2.2.3.1 Size*

Finer particle sizes are used in the production of roll compacted strips; the greater number of particle-particle contacts in the mixture compared to larger particles produces stronger green compacts. Smaller particles are also preferable as average density and thickness are inversely correlated to the particle size. There is a lower limit however, to the size which can be effectively compacted; small particles sizes and irregularly shaped particles increase the surface area within the mixture which increases the interparticle friction relative to larger particles, preventing the particles from properly bonding. Small particle sizes also lower the packing density and flowability of the powder [28], [30].

#### *2.2.3.2 Size Distribution*

Broad particle size distributions (PSD) or bimodal distributions are desirable to maximize the packing density of the powder [31]. Lower apparent density and flowability leads to difficulty feeding powder into the rollers [28].

#### *2.2.3.3 Morphology*

Spherical particles offer good flowability and high packing density due to lack of interlocking; however, this results in relatively poor compactability [26], [28]. In roll

compaction, this results in sheets with a relatively low green strength but greater thickness compared to spongy and irregularly shaped powders [29].

#### *2.2.3.4 Chemistry*

Material properties are also influenced by the powder chemistry. Bulk powder properties are important as softer particles are more easily deformed and produce more stable green compacts. Roll compaction favors blended elemental or master alloy mixtures rather than highly alloyed powders. The surface chemistry is also important as oxide layers on the surface prevent proper particle bonding [28].

## 2.3 Sintering

The type of sintering which takes place is dependent on the temperature at which sintering is performed relative to the solidus, liquidus, etc. of the alloy. A schematic of a binary phase diagram is given below in Figure 2-10. Solid state sintering (SSS) will be principally examined in the current work as temperatures being employed are below the solidus temperatures of the alloys.

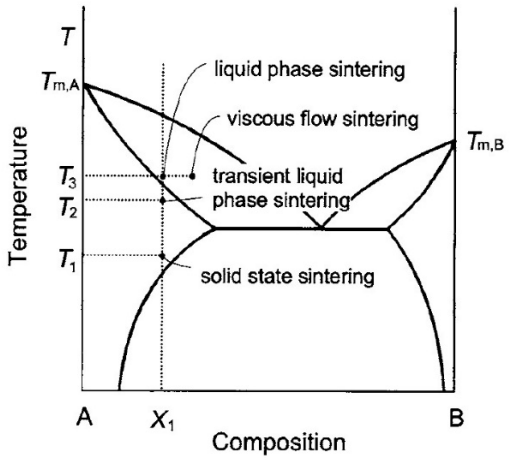


*Figure 2-10. Schematic of a phase diagram showing the categories of sintering [32]*

### 2.3.1 Solid State Sintering

Figure 2-11 below shows the evolution of particle contacts from a loose powder to the final stage of the solid-state sintering process. In the initial stage, adjacent particles will begin to form necks and contact between particles increases. At this stage, interaction occurs only between adjacent particles. In the intermediate stage of sintering, pores become spherical as neighboring necks begin to interact with each other. Finally, tubular pores are pinched closed, forming spherical or lenticular pores [33]. Some pores begin to close when material contains approximately 15% porosity and all pores are generally closed by 5% porosity. The closing of pores, specifically the vapor which is trapped within them, is a limiting factor of sintered density in the compact.

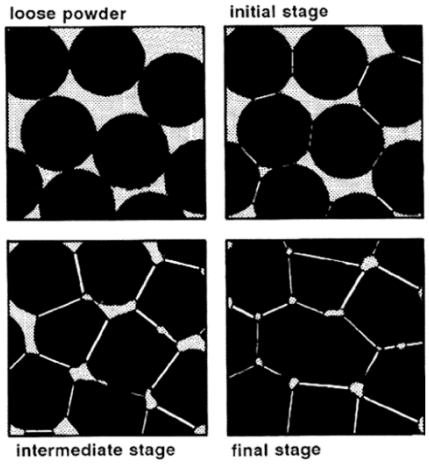


*Figure 2-11. Stages of sintering [31]*

Mechanisms of mass transport may be categorized as either surface transport, which includes evaporation-condensation, surface diffusion, and volume diffusion or bulk transport, which includes volume diffusion and grain boundary diffusion [31]. It is helpful throughout the discussion of sintering to consider pores as regions with high

concentrations of vacancies; as the system tends towards equilibrium, diffusion of atoms will be opposite to the diffusion of vacancies [26].

Figure 2-12 shows a schematic of two particles connected by a pendular bond with a summary of sintering mechanisms, where *x* is the neck radius and *a* is the particle radius. The centre of each particle is noted by cross hairs. The surface transport mechanisms are dominant at lower sintering temperatures. No shrinkage or densification takes place as the result of surface transport, the neck size *x*, however, does increase [30]. At higher temperatures, bulk transport mechanisms of volume diffusion and grain boundary diffusion become dominant [31]. These mechanisms result in densification of the compact.

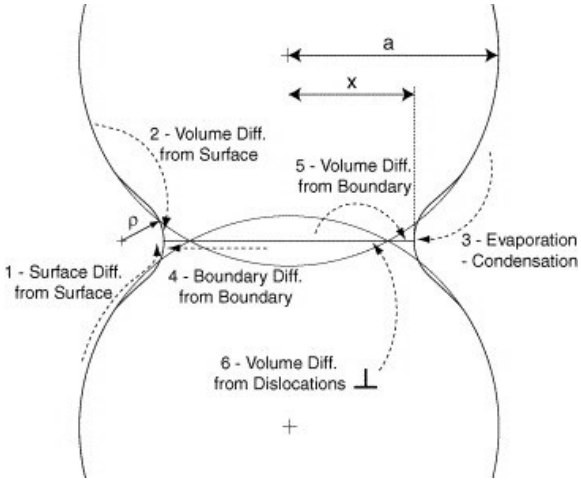


*Figure 2-12. Schematic of sintering mechanisms [34]*

### 2.3.2 Surface Diffusion

The surface diffusion mechanism is highly active during the early stages of sintering, even in the time during which the compact is being heated to the sintering temperature due to its low activation energy. The surface of the particle on the atomic level has many defects including vacancies, adatoms, terraces, and kinks, despite

appearing smooth at lower magnifications. A schematic of these defects is given in Figure 2-13.

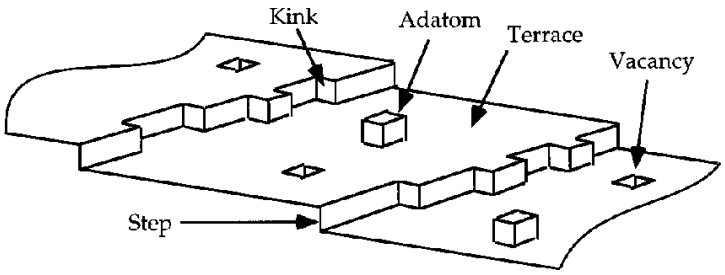


*Figure 2-13. Schematic of possible defects on a crystal surface [35]*

The first step of surface diffusion is the breaking of bonds between an atom and the particle; the atom usually originates from a kink. A kink is the edges of terraces, which are raised defects on the particle surface. From there, the atom moves along the surface of the particle until it finds a new attachment site, often a vacancy or other kink. The motion of the atom follows no particular path, but it does tend to move from, convex to concave surfaces, resulting in particle rounding but not shrinkage [33]. This mechanism is described by Path 1 in Figure 2-12.

### 2.3.3 Volume Diffusion (Surface)

Factors affecting volume diffusion are temperature, composition, and stress (either from pressure or curvature). Temperature affects both rates of vacancy creation as well as vacancy movement, where both are increased as temperature are increased. Concentrations of vacancies are higher in convex regions and lower in concave regions relative to equilibrium, which creates a diffusion path between these convex and concave regions. No shrinkage occurs when the atom both begins and ends at a particle surface. This type of volume diffusion corresponds to Path 2 in Figure 2-12.

### 2.3.4 Evaporation-Condensation

All metals have an associated equilibrium vapor pressure ($P_{EQ}$). This $P_{EQ}$ is higher at convex surfaces than at concave surfaces, such as the necks of sintered bonds, which results in concentration gradients in the regions directly above the powder surfaces. As the $P_{EQ}$ is higher above the convex surfaces, metal vapors diffuse towards the regions above the sintered bonds; this results in a pressure which is greater than the $P_{EQ}$ of the region, so the vapor condenses on the concave surface. The evaporation-condensation path is indicated by Path 3 in Figure 2-12.

### 2.3.5 Grain Boundary Diffusion

The grain boundary is a region of mismatch between two crystal lattices; the grain boundary is only about 5 atoms in width but acts as an effective path of motion for mass within the system. Grain boundary diffusion, Path 4 in Figure 2-12, is the dominating mechanism of sintering in metallic systems as the activation energy required is intermediate compared to surface and volume diffusion (low and high respectively) [30].

Grain boundaries are present both in the particles and at the sintered bonds between particles. Mass moves along the boundaries to be deposited at the sintered bond between particles, while vacancies are annihilated at the grain boundaries. The rate of grain boundary diffusion is dependent on the amount of grain boundaries per unit volume of the material. As the amount of grain boundaries peaks at the intermediate stage of sintering, so does grain boundary diffusion [33].

### 2.3.6 Volume Diffusion (Bulk)

Volume diffusion can also take place as a bulk transport mechanism; this corresponds to Paths 5 in Figure 2-12. Vacancies can be created and annihilated at

particle surfaces, pores, grain boundaries, and dislocations, while the number of atoms in the system remains constant. Atoms diffuse from the grain boundary through the particle to the surface while there is a counter diffusion of vacancies. When occurring as a bulk transport mechanism, volume diffusion does result in shrinkage and densification.

Path 6 in Figure 2-12 is dislocation climb. In this scenario, vacancies are annihilated at dislocations within the material. This promotes bulk volume diffusion as it reduces the concentration of vacancies within the material.

The volume diffusion mechanism occurs at higher temperatures, however, does not contribute as significantly to the sintering process. This is especially true of systems with small powder sizes, such as DPR, due to the high surface area of the particles [33]. Generally, shrinkage occurs during sintering as pores close and the PM parts densify. Occasionally, chemical reactions will occur upon heating that will cause swelling of the part. Excessive shrinkage in the sintering process is undesirable as it causes difficulties in final dimensioning of the part; however, some shrinkage may occur in during sintering efforts to eliminate porosity. Further, shrinkage may result in gradient densities throughout the part [33].

### 2.3.7 Solid-Liquid-Phase-Sintering

Sintering above the solidus temperature forms a liquid phase. Solid state sintering, which was previously discussed, is one stage of densification in SLPS. In addition to SSS, three additional stages of densification occur as a result of the liquid phase. Rearrangement, solution-reprecipitation, and then final densification may occur.

Rearrangement is the first stage of SLPS; upon melting the liquid moves, filling pores, and densifying the part. Full densification may be achieved by liquid formation alone should enough be present. In the example given by German [30], fully packed mono-sized spheres have a density of 74%, which would require a minimum of 26% liquid to achieve full density by rearrangements alone. The bonds formed during solid state sintering must also be considered as they will hinder densification by rearrangement.

## 2.4 Cold Rolling

Cold rolling is a deformation process which is used to reduce the thickness of sheets at low temperatures; rolling generally occurs at room temperature, but up to 200°C can still be considered cold rolling. Some benefits compared to hot rolling include a better surface finish, the ability to obtain thinner sheet thicknesses, and the ability to obtain high strength. Cold rolling does, however, require higher roll forces to cause deformation. Intermediate annealing steps may be required to increase the ductility of the material throughout the rolling process. Annealing can also be performed at the end of the processing line if a ductile product is desired.

Figure 2-14 shows a schematic of the cold rolling process where $v_r$ is the velocity of the rolls and $R$ is the radius. While some force imposed by the rollers results in densification if the material is porous, some produces elongation of the strip. The velocities of the sheet before and after it passes through the rolls are $v_o$ and $v_f$ respectively. Since the mass flow through the rollers is consistent, the velocity of the strip must increase to accommodate this. $L$ is the contact length between the sheet and the rolls, $p$ is the applied pressure. The change in strip thickness before and after cold

rolling, called the draft (Δt), where $t_I$ is the initial thickness, $t_f$ is the final thickness, is dependent on $R$ the radius of the rolls, and $\theta$ the nip angle according to:

$$t_i = t_f + 2R(1 - \cos\theta) \tag{3}$$

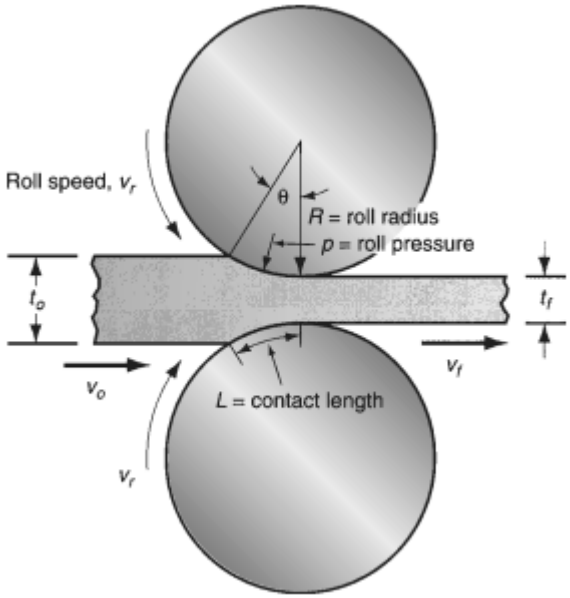


*Figure 2-14. Schematic of a workpiece undergoing cold rolling mill [36]*

$F$ is the force applied by the rollers described by (4). $Q_P$ is the pressure multiplication factor which is discussed further in Section 2.4.1. $W$ is the width of the strip and $L$ is the contact length calculated by Equation 5.

$$F = (1.15)\bar{Y}Q_P LW \tag{4}$$

$$L = \sqrt{R\Delta t} \tag{5}$$

Conventional roll mechanics analysis is focussed on determining the roll force $F$ required to cause a certain thickness reduction $\Delta t$, knowing the mechanical properties or flow curve of the sheet material being formed.

$$\bar{Y} = \mathrm{K}\varepsilon^n \tag{6}$$

The rolling mill used in the current research is capable of measuring roll force during cold rolling, which is a unique feature compared to many rolling systems. Equation 4 can be re-arranged to (7) for the purposes of this research to determine the flow curve of the roll compacted material.

$$\bar{Y} = \frac{F}{(1.15)Q_P LW} \tag{7}$$

### 2.4.1 Pressure Multiplication Factor

The pressure multiplication factor, $Q$, is a function of the frictional conditions of rolling, which depends on the reduction that occurs during a rolling pass and the contact length the roll has with the material [37]. The ratio between draft and contact length can be calculated to determine whether deformation is occurring inhomogeneously or homogeneously and further, whether $Q_p$ is valid. For inhomogeneous rolling, $Q_i$ is used, however this is not required for the current work. Homogeneous rolling will be the focus of the analysis as it is observed in all but three rolling passes.

$$When\ \frac{t_f}{L} < 1, \qquad deformation\ is\ homogeneous \tag{8}$$

## 2.5 Review of Contemporary Literature

### 2.5.1 Sintering and Homogenization of Selected Alloys

Using the DSC, Steedman, Corbin, and O'Flynn [38]–[40] have developed a quantitative method of determining the homogenization of titanium alloys by measuring of β-α phase transformation characteristics upon cooling. Measurements of the enthalpies of transformation as well as start and end temperatures of transformation were obtained. Throughout the studies, comparisons of quantitative measurements for various sintering times, powder sizes, and alloying methods were

performed and were successfully correlated to the qualitative observations of the sintered microstructures.

The effects of aluminium and vanadium as alloying elements in titanium were examined by comparing Ti6Al, Ti4V, and a BE Ti-6Al-4V alloy. While both aluminum and vanadium were individually successful sintering aids, the addition of both as elemental powders resulted in significant swelling due to the formation of both Ti-Al and V-Al intermetallics which negated any positive effects on the achievable shrinkage by the Al and V additions [38]. Use of Al-V MA in a Ti-6Al-4V sintering study showed complete homogenization of the microstructure with both fine and coarse MA particles, although the fine MA mixture appeared to homogenize more quickly [39].

The influence of iron powder size was studied in a BE Ti-2.5Fe alloy by O'Flynn [40]; a CP-Ti powder with a $d_{50}$ of 87 μm was mixed with iron powders having $d_{50}$ of 88, 20, and 6 μm, further referred to as coarse, medium, and fine respectively. Observations of large pores were made in the coarse powder, as expected. Interrupted DSC samples were created for temperatures of 1086, 1090, 1092, and 1094°C. The resultant microstructures were examined; the large porosity observed in the general sintering study was clearly visible from the 1092°C sample but not 1090°C and remaining iron particles became much more rounded at the higher temperature. Rapid diffusion of iron into the titanium matrix without counter diffusion of the titanium into iron creates a non-equilibrium condition and the potential for liquid formation at the eutectic. At the interrupted temperature of 1092°C, the rounded iron particles remain, surrounded by an intermetallic layer, followed by solidified eutectic, then a region of retained β-Ti due to elevated iron content. From the highest temperature of 1094°C, diffusion has

continued and almost no iron particles, intermetallic, or eutectic remain. Pores are observed with a surrounding layer of β-Ti. Further from the pore, unalloyed α-Ti remains. Kirkendall porosity is that which results from a non-reciprocal diffusion couple in a solid solution alloy. Where the diffusivity of element A is much higher in element B than vice versa, the Kirkendall effect occurs, resulting in porosity where element A was initially located [41]. This type of porosity is certainly a concern when using iron as an alloying element in titanium alloys.

### 2.5.2 Sintering Atmosphere

The effect of sintering atmosphere on oxygen content was studied for four CP-Ti powders, including powder produced by ADMA used in the current research. Powder was compacted via cold isostatic pressing (CIP) and sintered in the Sentro-tech tube furnace under both vacuum and argon atmospheres at 1200°C for 3 hours. Oxygen content was measured in the as-received condition and following sintering using each of the atmospheres [42]. Table 2-3 shows measurements for as-received and sintered conditions and the $d_{50}$ particle size.

*Table 2-3. Measured oxygen content in four CP-Ti powders before and after sintering [42]*

| **Powder** | ***$d_{50}$ (μm)*** | ***Oxygen (wt%)*** | | |
|---|---|---|---|---|
| | | ***As-Received*** | ***Argon*** | ***Vacuum*** |
| ***ITP*** | 109 | 0.24 | 0.38 | 0.38 |
| ***ADMA*** | 124 | 0.23 | 0.21 | 0.21 |
| ***Reading*** | 110 | 0.17 | 0.23 | 0.18 |
| ***Alfa Aesar*** | 35 | 0.31 | 0.34 | 0.33 |

Sintering under vacuum did yield some benefit for two of the powders, but oxygen content is equivalent in the other two. The oxygen content in the ADMA powder appears to have decreased under both sintering atmospheres compared to the as-received

condition. The ITP powder, for which the oxygen pick-up was most significant has a notably different morphology compared to the other three powders examined. It had a fully spongy morphology which corresponds to greater surface area to which oxygen can adhere.

### 2.5.3 Roll Compaction of Titanium and its Alloys

With the use of a binder and HDH Grade 2 titanium powder, Peter et al. roll compacted 380mm wide strips with thicknesses and green densities ranging from 2.5-2.9 mm and 75-85% respectively. After debinding, three processing routes were examined including hot rolling, cold rolling, and hot rolling twenty layers of titanium sheet in a steel cannister. It was found that the performance of the roll compacted sheet was highly dependant on the processing route by which it was densified. Hot rolling achieved the greatest elongation despite having the lowest formability and greatest number of observable microstructural defects. Cold rolling had the greatest formability and no observable microstructural defects. It was concluded that titanium powder could be used to produce sheets of material which satisfied ASTM specifications [7].

Defect free green strips of Ti-6Al-4V were roll compacted by Muchavi et al. [12] via DPR, using Ti powders with a $d_{50}$ of 125.1 μm, 60Al:40V master alloy powder additions with a $d_{50}$ of 45.7 μm and roll gaps of 0.3 and 0.5 mm. Densities ranged from 79-87% and thicknesses between 0.20-0.22 mm with rolling gap widths of 0.3 mm and 0.5mm. An explanation for the fact that rolled strip thickness was lower than the actual roll gap setting was not given by the authors; further, the minimal dependence of the strip thickness on the gap width observed is also unexpected. With 0.2 mm gap width, the powder did not compact at all. In another study by Chikosha et al. [11] four CP-Ti

powders were examined with a variety of sizes and morphologies; here, it was found that spongy powders yielded highest compactability and spherical powders did not compact at all. Of the compactable powder morphologies, the smaller sizes had higher green densities.

Neither of the above studies [11], [43] discuss sinterability or further densification processes of the material. It is unclear if any defects would present themselves downstream or what the resultant mechanical properties of these parts might be. The parameters of roll width, diameter, and speed were given, as was gap width in both cases but there was no consistency in parameters making it difficult to compare results between them. The applied pressure was not reported. The large number of variables in the roll compaction process necessitates optimization of each induvial step. The strips produced in both studies have green thicknesses of less than 0.25 mm which would only further be reduced by shrinkage and densification during later processing which also limits applications of the material.

A study by Govender et al. also performed DPR with CP-Ti powder. Values of gap width or sample thicknesses were not given but green density was reported at 89.9%. A CP-Ti powder with a $d_{50}$ of 27 μm was used. Compacts were sintered at temperatures of 1100, 1200, and 1300°C and times of 30, 60, and 90 minutes. The furnace chamber was evacuated and refilled with argon twice prior to beginning the run; continued flow of inert gas or vacuum were not used through the duration of the run. By sintering alone, near-full densities of approximately 99% were reported when the greatest sintering time and temperatures were used which is attributed to the excellent sinterability of the fine powder size used in this work.

An increase in hardness of the rolled strips compared to the powder substrate was observed which is attributed to the absorption of impurities interstitial elements [10]. It is postulated in this paper that it is the result of impurities in the argon atmosphere; however, the high area fraction of particle surfaces in the fine titanium powder may have these interstitial elements adsorbed onto the surface even in the as received state. During the sintering run, the contaminants evaporate at elevated temperatures and remain in the furnace chamber as a result of the stagnant atmosphere. This combined with the unideal sintering procedure can be the result of the increased impurities and hardness in the final part. Tensile testing revealed low ductilities of approximately 5%, compared to the minimum limit of 25% expected for wrought Grade 2 CP-Ti. Given the high densities achieved in the study, this low ductility is an indication of excessive oxygen contamination.

### 2.5.4 Optimization of Freund-Vector TFC 220 Parameters

O'Flynn and Corbin [29] worked to optimize roll compaction conditions for the Freund-Vector TFC 220 Roll Compactor used in this study. A more detailed description of this equipment is provided in Chapter 5. They explored the compactability of two different CP-Ti powders. The rolls were ridged and aligned horizontally and had a width of 30 mm and a diameter of 200 mm. Three roll force settings were tested (10, 30, and 50 kN) at three powder feed screw speed settings (10, 25, and 40 RPM) in addition to removing the screw and feeding the powder by gravity alone (saturated feed). The intermediate screw speed of 25 RPM was found to yield the highest densities and thicknesses with these powders of all four feed conditions; below this speed, powder flow was restricted by the screw and reducing flow to the rollers. Above this speed, the

powder was becoming compacted in the screw itself, again reducing flow to the rollers. Both conditions are undesirable and produced strips with low densities and thicknesses or did not compact the powder at all. Increasing roll force increased the density and reduced the thickness of the produced strips as expected. The effect was greater increasing roll force from 10-30kN than when increasing from 30-50 kN.

The run times for the testing matrix were relatively short, and it was not guaranteed that powder would not begin to compact within the screw system even at the intermediate screw speed of 25 RPM, a saturated feed appeared to produce strips with comparable density and thickness. As such, it was decided to proceed using only gravity to feed the powder with the intermediate roll force of 30 kN.

Roll compaction of two different CP-Ti powders, with 5 size ranges each, were performed with the system to study compactability. Powder supplied by Alfa Aesar produced using the Hunter Process had maximum mesh size ranges of 3-0.5 and the ADMA powder produced by ADMA using the Kroll Process had maximum mesh size ranges of 0.85-0.3. Smaller powder sizes, as in previous work by Chikosha [11] yielded better compactability compared to larger particles from the same lot. Comparing the two manufactures, the Alfa powder experienced significantly more compaction due to the high internal porosity. The densities observed in the Alfa powders were consistently lower than the ADMA at all mesh sizes in both green and sintered states. Additionally, the thicknesses observed, and maximum theoretical thicknesses were significantly smaller than those achieved with ADMA powder. While compactability is desirable, the benefits in this case are not sufficient to overcome the low apparent density. Based on these findings, the smallest cut of ADMA powder, with a $d_{50}$ of 133 μm will be used

moving forward. An applied force of 30 kN will be used with a saturated feed (gravitational).

In previous work using the Freund-Vector TFC-220 roll compactor using ridged rolls, significant density gradients were observed across the width of the produced strip (nearly full density in the centre of the strip decreasing to approximately 20% dense near the edges) [29]. This lead to the modifications performed to the HTTAL roll compacter, documented by a co-op student working with the HTTAL, H. Kaufman [44], which has replaced the ridged rolls with a die and punch roll system as shown in Figure 2-15. This significantly improved the variation in density gradient across the width of the sample. With the die and punch rolls, green densities ranging from 52-70% were achieved with CP-Ti sponge powder. Small flanges on the edge of the strips were produced; it was noted that these would not be acceptable on a commercial scale but are easily removed by grinding and were deemed acceptable at this stage of the research. The system, however, may be further optimised in the future to eliminate these flanges as well.

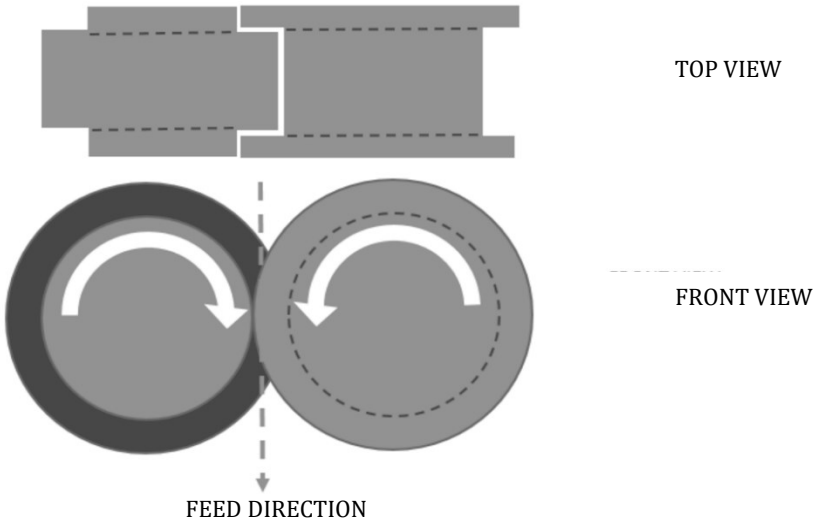


*Figure 2-15. Schematic of the die and punch rolls (not to scale) [44]*

The following Table 2-4 summarizes a number of parameters and results reported in the studies examined for the literature review of titanium roll compaction. An *X* listed in the table below indicates that the parameter was not reported by the author of the study.

*Table 2-4. Summary of titanium roll compaction studies reviewed*

| Study | Alloy | Binder | Rolling Parameters | | | | | Green Strip Properties | | Analysis of Sintering & Densification |
|---|---|---|---|---|---|---|---|---|---|---|
| | | | Diameter (mm) | Gap (mm) | Width (mm) | Speed (RPM) | Force (KN) | Density (%) | Thickness (mm) | |
| **Peter et al.**[7] | Ti-6-4 | Yes | X | X | 380 | X | X | 75-85 | 2.5-2.9 | Yes |
| **Muchavi et al.** [12] | Ti-6-4 & CP-Ti | No | 400 | 0.2, 0.3, 0.5 | 30 | 3, 5, 7, 10 | X | 52-86 | 0.20-0.22 | No |
| **Chikosha et al.** [11] | CP-Ti | No | 55 | 0.025-0.3 | 110 | 20 | X | 80-95* | 0.1-0.3* | No |
| **Govender et al.** [10] | CP-Ti | No | 80 | X | 40 | 14** | X | Max. 89.8 | 0.33 | Yes |
| **O'Flynn and Corbin** [29] | CP-Ti | No | 200 | X | 30 | 2 | 10, 30, 50 | 38-57 | 1.2-2.9 | Yes |
| **Kaufman** [44] | CP-Ti | No | 200 | X | 20 | 2 | 30 | 52-70* | X | Yes |

*Approximate values obtained from graphs

**Only one roller was driven

# Chapter 3: Objective

The use of titanium alloys has clear opportunities for more widespread use in current and new industries were it more economically and environmentally feasible. The use of roll compaction can address both of these issues for titanium alloys; it has already been successfully used for other alloys based in iron and nickel. There have been some articles published with positive outcomes that focus on a particular aspect of the process using CP-Ti and Ti-6Al-4V, but robust titanium roll compaction studies are notably lacking at this time.

In conjunction with advanced processing procedures, alloy design is cited as the second avenue by which cost reduction and advancements can be made; iron has been proposed as a suitable replacement for vanadium to produce a similar microstructure and properties with lower costs and improved biocompatibility.

This study seeks to analyse the roll compaction powder metallurgy method for the creation of thin gauge Ti-6Al-4V and Ti-5Al-2.5Fe strips from DPR, through densification and heat treatments, to a final product with a complete analysis of density, microstructure, and mechanical properties.

# Chapter 4: Materials

Grade 3 Titanium sponge powder was sourced from ADMA. A 60Al-40V intermetallic MA sourced from Reading Alloys was used to create a mixture with a targeted composition of Ti-6Al-4V which will be referred to as Ti-xAl-yV. The ADMA CP-Ti, with elemental Al (sourced from ECKA Granules) and Fe powders (sourced from Alfa Aesar) were used for an alloy with a target Ti-5Al-2.5Fe composition which will be referred to as Ti-xAl-yFe. In both cases, appropriate amounts of alloying elements were mixed with the ADMA Ti sponge and were milled for 1 hour in the Turbula Mixer. General labels are used to differentiate the alloys throughout the report rather than the target compositions to account for variations across samples. Powder size distributions obtained from a *Malvern* particle sizer through the Dalhousie Minerals Engineering Centre (MEC) for each powder are given in Table 4-1.

*Table 4-1. Powder properties for materials used*

| Powder | d10 (µm) | d50 (µm) | d90 (µm) | Source |
|---|---|---|---|---|
| **Ti** | 68.1 | 133 | 232 | [45] |
| **60Al-40V** | 8.7 | 24.2 | 45.1 | [45] |
| **Al** | 10.2 | 12.7 | 34.1 | [46] |
| **Fe** | 8.43 | 20.2 | 38.2 | [47] |

Samples of each powder were prepared for SEM. A monolayer of powder was distributed over a stub covered with carbon paste and was allowed to cure at room temperature for 24 hours. Images of the titanium powder are shown in Figure 4-1 and alloying powders in Figure 4-2.

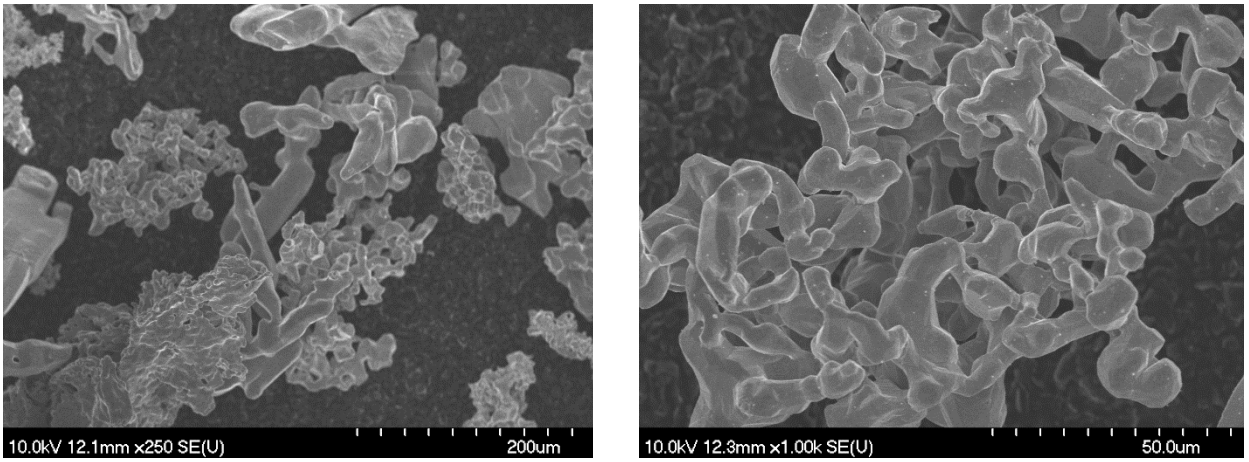


(a) (b)

*Figure 4-1. SEM images of Grade 3 Titanium Sponge powder at (a) 250x and (b) 100x*

The morphology of the titanium powder particles is irregular and variable; some particles are more block-like while others are highly irregular and with a low density as highlighted in Figure 4-1 (b).

All alloying powders are irregular in shape. The MA particle is angular and blocky. The Al and Fe powders are both more rounded. The Al has a smooth surface while the Fe powder is spongy.

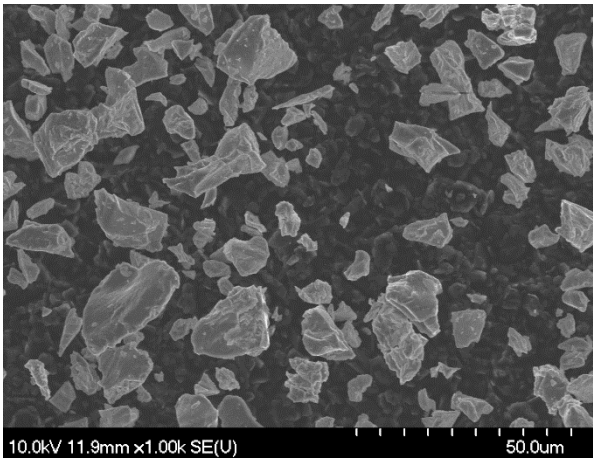


(a)

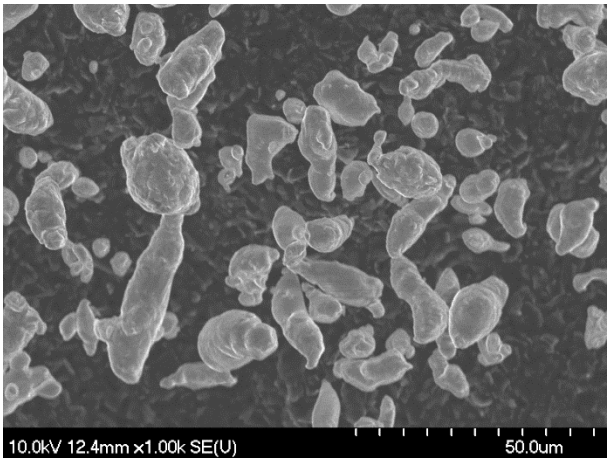


(b)

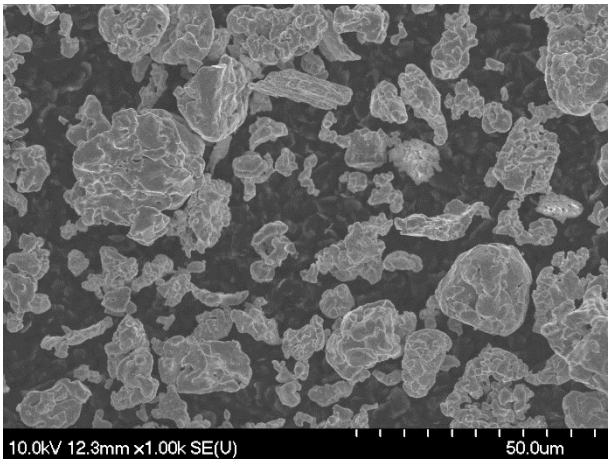


(c)

*Figure 4-2. SEM images of additive powders used (a) 60Al-40V master alloy (b) aluminium (c) iron sponge*

# Chapter 5: Procedure

## 5.1 DSC Study of Sintering

Sintering trials were performed with roll compacted samples of Ti-xAl-yV and Ti-xAl-yFe cut from green strips that had been previously created by H. Kauffman, a co-op student with the HTTAL, and repeated with samples prepared by the author using the same rolling parameters. A roll force of 30KN was used with a gravity fed powder system as was determined to be optimal by Corbin and O'Flynn [29]. The rolls however had been switched from ridged rolls to a smooth die and punch roll between these studies to achieve a more uniform density throughout. A 3D printed unit which streamlines powder feed was also used for compaction of the DSC samples unless specified otherwise.

The 3D printed green feeder (GF) was designed by H. Kaufman to sit in the bottom of the hopper and direct the powder flow towards the center of the rolls, reducing the flashing that was observed in earlier use of the die and punch rolls. Figure 5-1 shows a dimensioned schematic of the part.

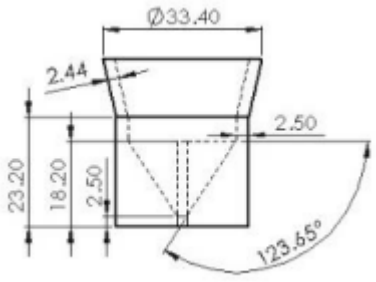


*Figure 5-1. Schematic of the 3D printed green feeder [44]*

A yttria crucible which was conditioned with titanium was used to minimize interaction between the sample and crucible. The furnace was evacuated and filled with

argon prior to each experiment; additionally, flowing 99.99% argon atmosphere of 50ml/min was used through the duration of each test. A zirconia getter ring was placed on the stem below the crucible to react with any residual oxygen in the furnace and gas flow. A heating rate of 20 K/min to 1200°C and a cooling rate of 40 K/min to room temperature was used for all samples. An isothermal hold at 1200°C ranged from 0-120 minutes. Thirty-minute intervals were used, yielding 5 samples per alloy. One sample of each Ti-xAl-yV and Ti-xAl-yFe was also heated to 1250°C with a 30 min hold time at temperature.

Following heat treatment, samples were mounted in cold epoxy under a vacuum and polished to a final step of 0.1 μm colloidal silica. Optical micrographs were taken before etching for analysis of density. The surface was then etched with Kroll's reagent (nitric acid, hydrofluoric acid, distilled water) and additional micrographs were obtained for microstructural characterization.

## 5.2 Press and Sinter Study of Powder Compactability

Cylindrical dilatometry (DIL) samples with a diameter of 6.3mm and a mass of approximately 500mg were pressed from CP-Ti, Ti-xAl-yV, and Ti-xAl-yFe alloys. A mixture of Licowax C and ethanol was applied to the walls of the punches to reduce die wall friction during compaction. A double action die and punch system was used in a manual *Carver* hydraulic press to compact to a range of pressures: 160, 275, 390, 505, and 620 MPa.

The sample was weighed following its extraction from the punch, in addition to 3 measurements of sample height which were averaged. The resulting green density of the sample was calculated and compared to the theoretical density of the element or

alloy. The pressed parts were then placed in an alumina crucible filled with zirshot and sintered in the Sentro-tech furnace. The heating rate was 5 K/min to 1200°C with a one-hour dwell time. The furnace elements were then turned off and the parts were allowed to furnace cool. From each alloy, samples of the lowest, middle, and highest pressures were mounted lengthwise in bakelite and ground to approximately halfway through the diameter using an autopolisher. They were polished to a final step of 0.1 μm colloidal silica, micrographed for optical density, then etched with Kroll's Reagent, and micrographed again.

Tap density was also calculated using the DIL die and punch. The height of the punch was fixed at 11.35 mm below the surface of the die and the diameter was 6.3 mm. The die was then slightly overfilled with powder and tapped against the benchtop. Any excess powder was scrapped from the top and the die surface was wiped with a Kimwipe. The powder was then dumped into a weigh boat, mass was measured, and tap density was calculated. This is later plotted as 0 MPa when compared to the pressed and rolled samples.

## 5.3 Density

### 5.3.1 Optical

Unetched micrographs taken at 5x magnification on a *Zeiss Axiotech* microscope with an *Infinity1 Lumenera* camera were used for all optical density measurements. A series of micrographs was taken so that the entire image was micrographed and that each image overlapped with approximately 30% of the previous. The micrographs were then stitched together using the *grid/collection* option of the *stitching* plugin in the Fiji ImageJ computer program [48], [49]. The image was rotated and cropped to a

rectangular area containing the maximum amount of sample possible while not including any of the surrounding bakelite. The excellent contrast of an unetched titanium alloy and the dark porosity allowed for a single step using the built-in *make binary* process was then applied to the image. An image may also be converted to 8-bit and the threshold of the binary may be adjusted manually for scenarios where isolating porosity is more difficult. Once the image is converted to a binary image, the *Measure* function was used to yield image data such as total area of the image and the area fraction of the porosity.

In cases where the sample was bent, or not reasonably rectangular, the stitched image was cropped to two separate, non-overlapping images and the same process as described above was performed on each. The porosity of the sample was then calculated as a weighted average of the area fraction of porosity and total areas of each image.

### 5.3.2 Archimedes

Apparent mass in air and in water was obtained for Archimedes Density using a *Sartorius* balance with the auxiliary density kit. Samples were submerged in a beaker filled with distilled water and 1-2 drops of *Kodak Photoflow* acting as a surfactant to help prevent the formation of air bubbles on the samples' surface. The temperature of the water was measured; all values were inputted in the following equation and the density was calculated, where $\rho$ is density of the sample, $\rho_w$ is the density of distilled water, taking temperature into account. $M_w$ and $M_a$ are the mass of the sample in water and air respectively.

$$\rho_s = \frac{\rho_w}{1 - \left({}^{M_w}/_{M_a}\right)} \tag{9}$$

## 5.4 Grain Size Measurements

Microscopy samples from selected rolling conditions were used for optical grain size analysis. After polishing to a final step of 0.1 μm colloidal silica, samples were etched with Kroll's Reagent for 8-10 seconds and rinsed with water. They were micrographed and grain boundaries were counted manually as per ASTM E112 – 13 *Standard Methods for Determining Average Grain Size* [50]. The circular intercept procedure was used to compensate for elongated grains.

## 5.5 Roll Compaction Sample Set 1: Process Optimization

### 5.5.1 Sample Preparation

The green strips used for this set of samples were compacted by H. Kaufman [44] using the following procedure. A *Freund-Vector TFC-220* roll compactor, pictured in Figure 5-2, was used to create strips of Ti-xAl-yV and Ti-xAl-yFe. The powder from the hopper was gravity fed through the 3D printed part to a die and punch-style roller set with a diameter of 200 mm rotated at a speed of 2RPM as described in Chapter 2.5.4. Roll pressure was held constant at 30 KN; the gap width adjusted automatically for each alloy but were measured by the instrumentation and recorded. Gaps ranged between 1.17 and 1.22 mm.

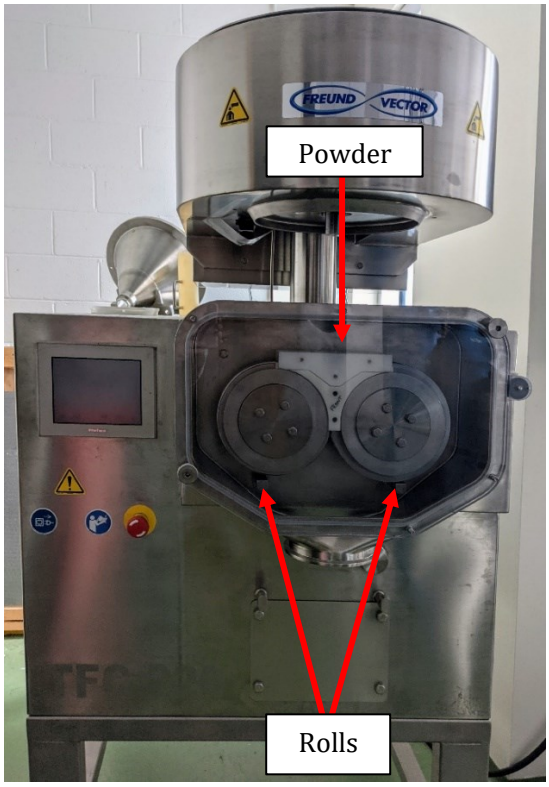


*Figure 5-2. Image of the Freund-Vector TFC 220 in the HTTAL at Dalhousie University*

The green strips were produced with densities of approximately 60-63% of the theoretical value. The average thickness and width were 1.3 mm and 20 mm respectively, and lengths ranged from 14-16 cm. Strips were placed on their side in an alumina crucible, supported by zirshot and sintered in the Sentro-tech furnace with a heating rate of 5 K/min to 1200°C and furnace cooled. The furnace chamber was evacuated and refilled twice with argon prior to the start of the run. A flowing argon atmosphere of 5 L/min was also used for the duration of the run. One strip of the sample of each alloy had a dwell time of 1 hour and the other for 2 hours. A photograph of a crucible taken prior to a sintering run is shown in Figure 5-3; three ridged samples on the left side are CP-Ti pieces used to getter any remaining oxygen in the system and six smooth pieces on the right side are titanium alloy roll compacted pieces.

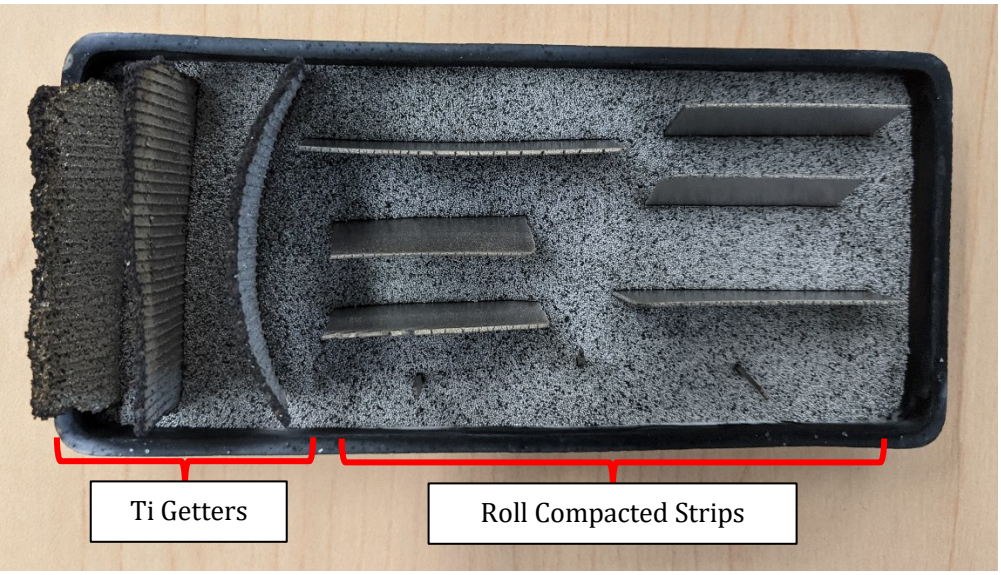


*Figure 5-3. Photograph of samples in alumina crucible supported by zirshot with titanium getters*

### 5.5.2 Cold Rolling

Cold rolling was performed on a two-high rolling mill photographed in Figure 5-4. The rolls in this machine were smooth, with a diameter of 102 mm (4 in). The roll gap was set manually using feeler gauges. Roll speed was 2 RPM, where each roll was independently driven. Two load sensors, one on each roll, were set to register the peak load reached during each rolling pass. The two peak loads were added together to give the peak load experienced during the pass.


*Figure 5-4. Image of the two-high cold rolling mill at Dalhousie University*

A schematic of the rolling procedure is given in Figure 5-5. The first rolling step included one pass at 1.0 mm was used to flatten the sample and reduce rolling defects later in the process, followed by two passes at a gap of 0.05 mm. At this point, the samples were cut into two. One half of the sample was annealed for 1 hour at 1200°C while the other half proceeded directly to the next rolling step. The second step consisted of two rolling passes at a 0.05 mm GW. Finally, all samples were then rolled with a zero-GW where the rolls were brought together and preloaded with 150-200 N. This was followed by a final anneal performed on all samples for 1 hour at 1200°C.


*Figure 5-5. Schematic summarizing the rolling path and heat treatments performed on Sample Set 1*

Between each rolling and heat treatment step, a small sample from the end of each strip was removed using a precision saw for optical microscopy and density analysis.

Physical dimensions of the full strip were recorded, and Archimedes density analysis was also performed on the strip between each rolling step.

## 5.6 Roll Compaction Sample Set 2: Tensile Specimen Production

### 5.6.1 Sample Preparation

Ti-xAl-yV and Ti-xAl-yFe alloy powder mixtures were rolled with the Freund-Vector TFC-220 with the same parameters in *Roll Compaction Sample Set 1* to produce green strips. The 3D printed powder feeder was not used for this set of samples as it hindered overall powder flow from the hoppers to the rolls. The overall increase to the sample thickness and density without the feeder was decided to be more beneficial than potential of slight improvements to density gradient at the edges of the sample.

The width and thickness of the green strips was approximately 20 mm and 1.5 mm respectively. Lengths of the DPR strips ranged from 15-34 cm. Average green density of the Ti-xAl-yV was 70.90% and Ti-xAl-yFe was 81.22%. They were then cut to approximate lengths of 100 mm, and the flashing was manually sanded with silicon carbide grinding paper.

All samples in Set 2 were sintered for 1 hour at 1200°C. A new support system was cut from 0.5 mm CP-Ti plate using a waterjet cutter, shown in Figure 5-6 to address the formation of surface defects. Zirshot was used to support the samples in the alumina crucible in the previous sample set; however, surface defects were noted where the titanium strips deformed during the sintering process around the zirshot. The zirshot could be removed by brushing. but left divots in the half of the sample that was submerged in the support. These divots were suspected of causing edge cracks during cold rolling.

The new support was comprised of two shorter pieces of wrought Ti sheet in a comb shape which interlock perpendicularly with a longer piece. There were two slots above and two below the center support in which roll compacted samples were placed. From the view in the photo below, the filled support is then flipped and placed into the alumina crucible for sintering so that the weight of the sample is distributed across its length and supported by the alumina crucible.

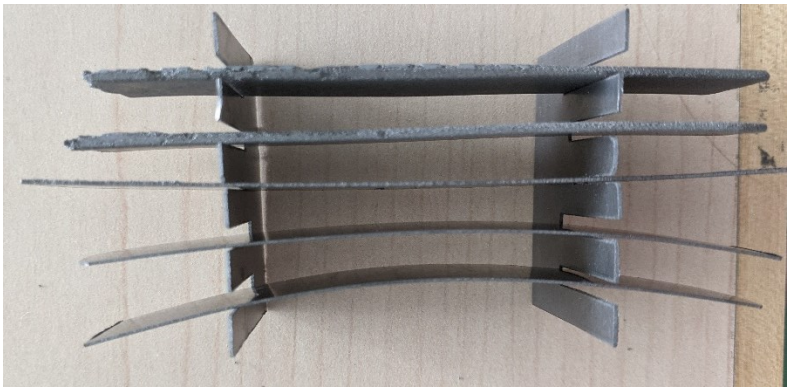

*Figure 5-6. Photograph of four roll compacted samples in CP-Ti comb support before being placed into the alumina crucible for sintering*

### 5.6.2 Cold Rolling

The rolling and heat treatment processing was similar for Set 2 as for Set 1. In this stage, all samples were sintered for 1 hour following roll compaction. The average thickness of the Set 2 strips was larger than set 1 (i.e., 1.5 mm increased from 1.2 mm) since the powder flow was less restricted without the use of the green feeder. When GW was reduced from 1.0 to 0.05 mm in one rolling pass, samples developed isolated edge cracks which propagated into the sample during the following reduction steps. To mitigate this problem, an additional rolling pass at 0.3 mm was added to the first rolling step to flatten more gradually any remaining flashing from the roll compaction step and reduce the aggressiveness of this initial reduction.

The intermediate anneal was again chosen as a variable in the rolling path. The importance of the additional "repeat" roll step containing two more passes at 0.05 mm GW was also studied. A total of four roll paths were determined where Paths A and B utilized the intermediate anneal and C and D did not. Paths A and C did not include the repeat rolling step, while Paths B and D did. These roll paths are summarized in the schematic Figure 5-7.

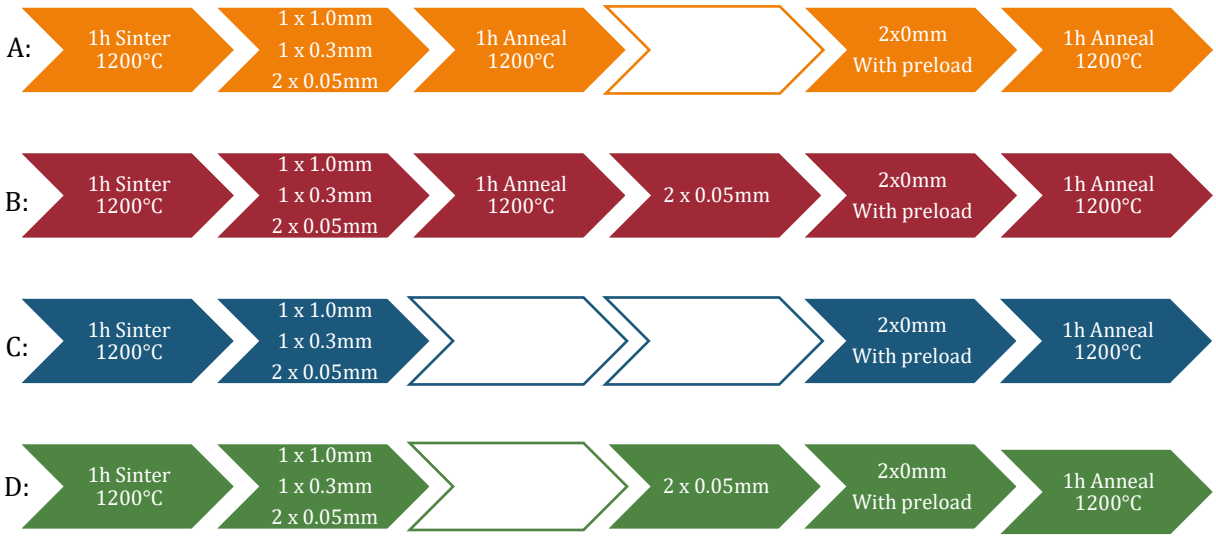


*Figure 5-7. Schematic summarizing the rolling path and heat treatments performed on Sample Set 2*

Both the order in which strips were created and direction of rolling were recorded during the roll compaction stage. Strips generally produced sufficient length to produce 1-2 tensile bars. One Ti-xAl-yV was long enough to produce three tensile strips. In the case that multiple samples were produced from one strip they were named using a letter A, B, C in addition to the number of the strip, where A was at the first part of the strip rolled. While data is presented throughout this report in terms of roll path, the record of when compaction occurred and where on the strip a sample was retrieved from was valuable information to maintain.

A minimum of two samples was desired for each roll path. This was achieved for all except Ti-xAl-yFe Path D for which only one sample was obtained. An extra Ti-xAl-yV tensile sample was available and used produce a third sample rolled via Path D. The rolling path of a sample was always randomized such that duplicate samples were not taken from the same roll compacted strip if multiples were available or same location on a different strip; for example, the two samples rolled under a particular path were not from the *B* position of different strips. This was done to remove any false correlations resulting from density gradients which may occur along the length of the strip.

## 5.7 Cold Rolling of Wrought Ti-6Al-4V

In parallel with the above work, wrought High Strength Grade 5 Ti-6Al-4V plate with a thickness of 1.6 mm was obtained from McMaster-Carr. Strips were cut to the approximate length and width of the roll compacted strips, 120 mm and 20 mm respectively using a water jet cutter. They were then annealed for one hour in lieu of sintering and cold rolled using the same procedure as used for Sample Set 2 (Figure 5-7). Three samples were rolled via Path C using only the first and final rolling steps. Path D was performed on three samples including the repeat rolling step of two passes at 0.05 mm. None of the wrought samples were annealed mid-rolling, and all samples were annealed following final rolling. This was done in order to compare the roll mechanics behaviour of a dense wrought alloy with the porous PM derived strips processed under the same conditions. It also allowed a measurement of the tensile properties of a wrought alloy processed in the same way for comparison purposes.

## 5.8 Tensile

Following the final annealing heat treatment, dogbone tensile bars were machined according to the ASTM E8 [51] standard for sub-sized samples as described in Figure 5-8 and Table 5-1. Thickness of the samples was not altered following the final annealing treatment. The lengths of the samples were also not altered and ranged from 100-130 mm where the gauge length was centered.

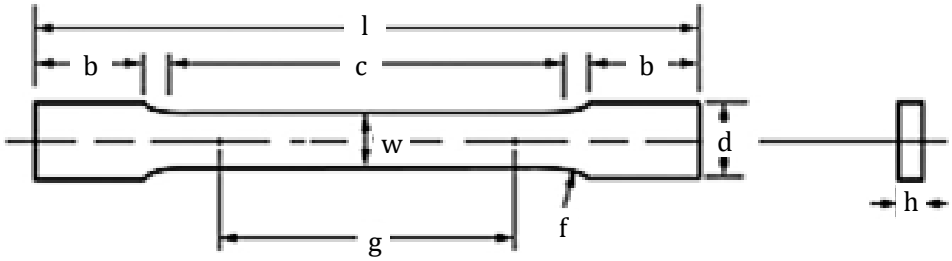


*Figure 5-8. Schematic of dog bone tensile sample modified from [51]*

*Table 5-1. Dimensions for sub-sized dog bone tensile samples modified from [51]*

| Dimensions | Label in Figure 5-7 | Requirements (mm) |
|---|---|---|
| **Gauge length** | g | 25 ± 0.1 |
| **Width of reduced section** | w | 6.0 ± 0.1 |
| **Radius of Fillet** | f | 6 |
| **Overall length** | l | Min. 100 |
| **Thickness** | h | Thickness of material |
| **Length of reduced parallel section** | c | Min. 32 |
| **Length of grip section** | b | Min. 30 |
| **Width of grip section** | d | Approx. 10mm |

Twenty-three tensile samples were produced: nine roll compacted Ti-xAl-yV, seven roll compacted Ti-xAl-yFe, six wrought Ti-6Al-4V in the as-rolled condition, and one wrought Ti-6Al-4V after the initial annealing treatment without any cold rolling which is referred to by "as-sintered". Testing was performed on an *Instron 1332* tensile

frame with hydraulically clamping diamond grips. A 25 mm strain gauge was used to measure elongation and force measurements were obtained directly from the MTS software controlling the frame. Maximum strain ($\epsilon_m$), Modulus of Elasticity (E), 0.02% Offset Yield Stress (YS), and Ultimate Tensile Stress (UTS) were calculated from the exported data. One end of the sample was marked as the "top" and three dots were marked along the length of the reduced section. Width and thickness dimensions were recorded at each dot in the reduced sections of each tensile prior to testing; the set of dimensions used in the calculation of area was determined by the location nearest to the break of the tensile bar. If the location of the break was closer to the middle two dots, an average of the two measurements was used.

## 5.9 Hardness

A *NANOVEA PB1000* mechanical tester was used to obtain Vickers microhardness measurements of wrought Ti-6Al-4V and roll compacted Ti-xAl-yV and Ti-xAl-yFe. Samples rolled via Paths A and C were selected from each material after each step of the rolling process (first roll step, intermediate anneal, final roll step, final heat treatment). Cross sections of the samples were mounted in polyfast and polished to a final step of 0.1 μm colloidal silica. A load of 2.5 N was used for all testing. Ten indents were placed across the width of the cross section in approximately the middle of the sample with a minimum or 1mm between indents.

## 5.10 Composition Analysis

### 5.10.1 LA-ICPMS

Samples were cut for Laser ablation inductively coupled mass spectroscopy (LA-ICPMS) from the grip end of broken tensile bars. Pieces were delivered to the Mineral

Engineering Center (MEC) at Dalhousie University. A report of the full analysis was provided by MEC. Data is normalized to the relevant alloying elements is reported throughout this study.

### 5.10.2 Oxygen Content

The *Eltra Elementrac OHN-p Analyser* was used to measure oxygen levels in the Ti-xAl-yV powder mixture and rolled strips. Rolled wrought Ti-6Al-4V rolled via Path C and samples of both Ti-xAl-yV and Ti-xAl-yFe roll compacted strips rolled under each of the Paths A, B, C, and D were measured.

For RC and wrought samples, pieces were cut from the grip end of tensile bars using a diamond precision saw. Each batch was cleaned by soxhlet ether extraction for a minimum of 1 hour then rinsed with acetone immediately prior to testing. One or two pieces of the strip samples were chosen to achieve a mass that best approximated that of the standard used for calibration. For powder material, a nickel capsule was used to hold the samples. The top was then folded over and pinched shut. Either the capsule of powder or rolled strip pieces were then placed in a nickel coil basket, pictured in Figure 5-9. The top end of the coil was then bent over the opening such that it could be flipped over without any pieces falling out.

*Figure 5-9. Image of nickel basket used for OHN testing*

The standard sample was a cylindrical sample of titanium with a mass of 100 mg. Sample masses, not including the capsules and baskets ranged from 62.4-153.6 mg for rolled samples and 85.2-103.1 mg for powders. Standard samples were run in the OHN

analyser which were used to calibrate the machine prior to running the first step and periodically throughout the duration of testing. Each calibration was then validated using another standard sample. Three repeats were performed for each item tested and the average is presented.

# Chapter 6: Results of Compactability and Sintering Study

## 6.1 Compaction and Sintering Under Die Pressing Conditions

The CP-Ti and alloy powder mixtures were compacted using a 6.3 mm radius die and punch system. The data point listed at 0 MPa is a tap density measurement with no applied pressure. Green density was determined using mass and compact dimensions. The compacts were then sintered for 1 hour. Sintered density was determined optically, using the image analysis methods described in Section 5.3.1, for the lowest, medium, and highest pressures. The results are presented below in Figure 6-1 where the solid points represent the green densities and hollow circles represent the sintered densities.

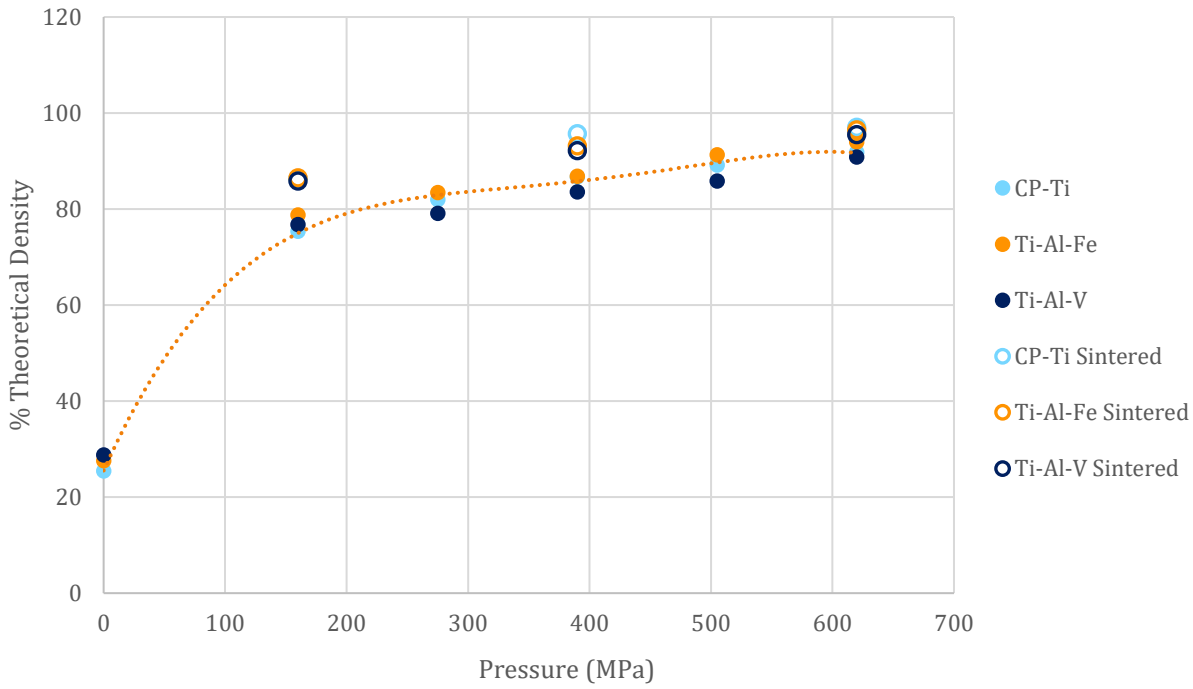


*Figure 6-1. Green and sintered densities of CP-Ti, and Ti-xAl-yV and Ti-xAl-yFe alloys from a die press operation as a function of compaction pressure (MPa)*

The Ti-xAl-yV was slightly less compactable than the CP-Ti and Ti-xAl-yFe, which is expected due to the presence of the 60Al:40V hard, intermetallic particles.

The Ti-xAl-yFe had a slightly higher compactability than CP-Ti, which can be attributed to the small aluminium powder size which fills the voids between the titanium powder. In addition, it is expected that the pure Fe and Al powders would be softer than the pure Ti powder. Green densities above 90% were achieved for all powders, where the maximum was 93.34% in CP-Ti. The CP-Ti powder used in this study was very porous and spongy, and therefore highly compactable. This appears to have an overwhelming effect compared to the benefits of a bimodal PSD or hindrance of poorly compactable powders on the compactability of the alloy mixtures as the observed green densities are very similar.

As the green densities of each alloy are similar to one another at each pressure, so are the sintered densities. The densification as a result of sintering decreases as compaction pressure increases. The maximum sintered density was 97.4%, also in CP-Ti compacted at 620 MPa. This relatively small increase in density during sintering is evidence of the poor sinterability of the coarse CP-Ti powder used.

Ti-xAl-yV is used as an example to show the progression of the porosity at different compaction pressures in Figure 6-2. Micrographs were taken of the unetched samples and stitched together using the *stitching* plug-in of *Fiji ImageJ* software [48]. As expected, the observed porosity decreases as the compaction pressure is increased. There are no observed density gradients throughout the compacted sample pressed in the DIL die.

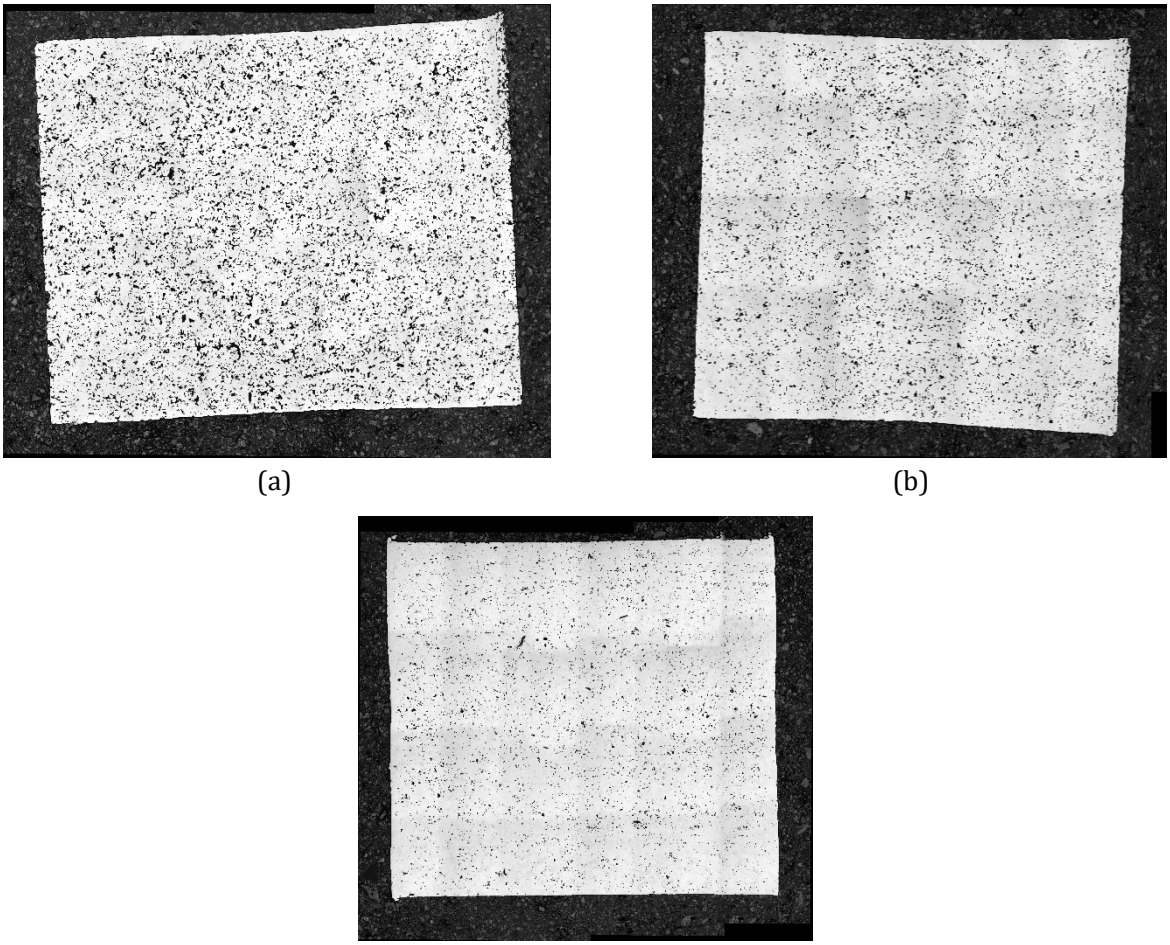

(a) (b)

(c)

*Figure 6-2. Unetched optical micrographs of Ti-xAl-yV samples compacted at (a) 160MPa (b) 370MPa and (c) 620MPa, sintered for 1 hour in the Setro-tech tube furnace*

Figure 6-3 (a-c) shows etched images of the compacted and sintered Ti-xAl-yV samples through the range of compaction pressures. The microstructure of the Ti-xAl-yFe compacted at 620MPa is also compared in Figure 6-3(d).

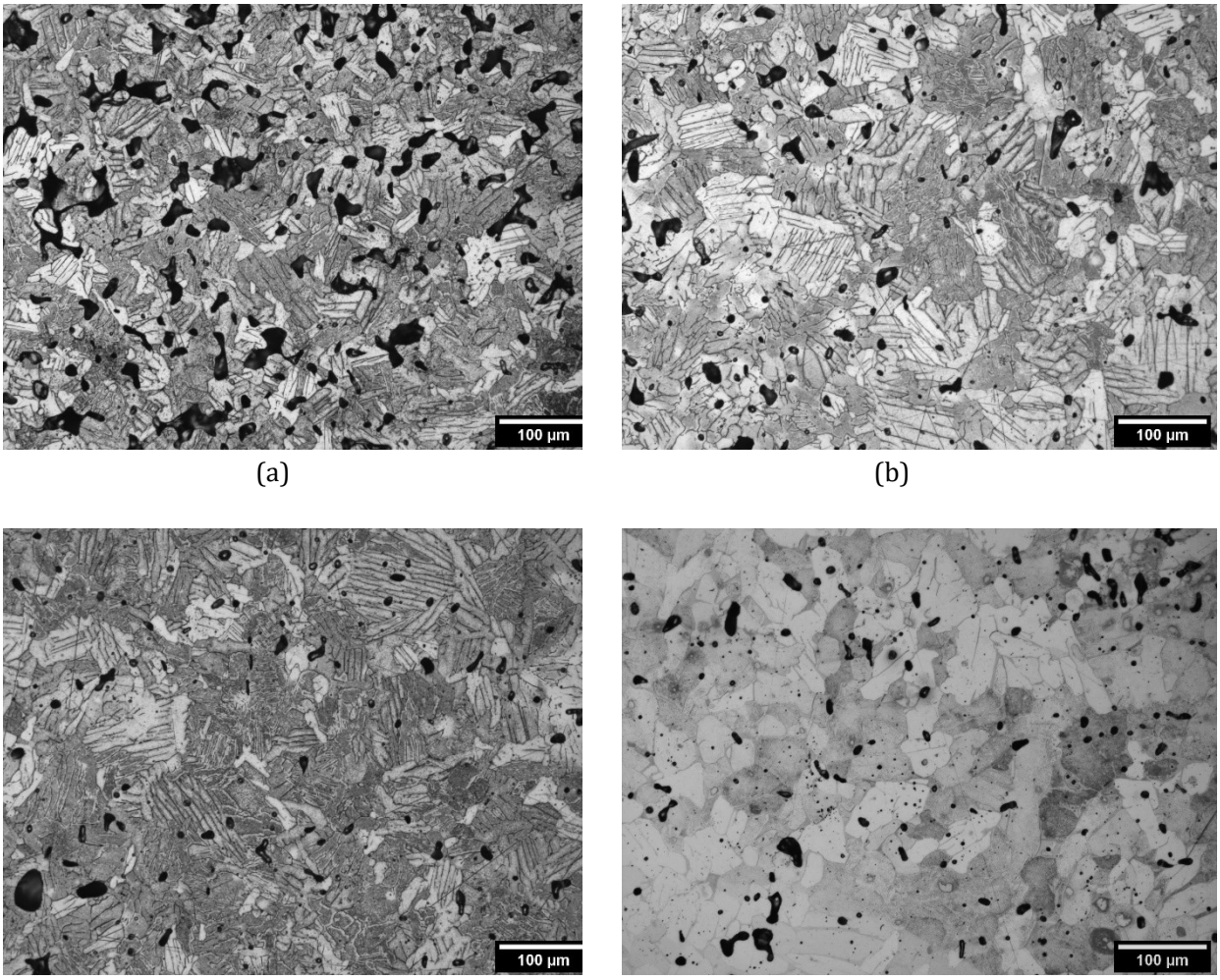


(a) (b)

(c) (d)

*Figure 6-3. Etched optical micrographs of Ti-xAl-yV samples compacted at (a) 160MPa (b) 370MPa (c) 620MPa and (d) Ti-xAl-yFe compacted at 620MPa, sintered for 1 hour at 1200 °C in the Sentrotech*

At higher magnifications, both the shape and amount of porosity can be observed; the porosity is rounded at all pressures for both alloys. At lower pressures, the porosity is irregularly shaped but becomes more circular as compaction pressure is increased. There is a platelike α-Ti microstructure with β-Ti retained at the grain boundaries observed in all Ti-xAl-yV samples as is expected in the material following furnace cooling. The rate of cooling changes throughout the duration of cooling from -10 to -2°C/min as the temperature gradient between the temperature within the tube furnace and room temperature impacts the rate of cooling. The microstructure of the Ti-xAl-yFe

alloy in Figure 6-3(d) does not correspond with any of the Ti-xAl-yV samples. Some platelike α-Ti structure is observed but at plate widths much larger and shapes more rounded than in the Ti-xAl-yV samples. The majority of the samples appear to have a more equiaxed structure.

## 6.2 Sintering Behavior of Roll Compacted Samples

Sintering trials were performed with samples cut from the green roll compacted strips of Ti-xAl-yV and Ti-xAl-yFe. They were heated at the 1200°C sintering temperature with hold times at temperature ranging from 0-120 min and optical density measurements were obtained. The initial trials performed using strips prepared by H. Kauffman and some samples were sourced from the end of the sample width. It was found however, that density gradients across the width of the sample still exist in the green state but are ameliorated through later cold rolling. In the repeat testing, the results of which are shown below in Figure 6-4, samples were sourced from the centre of the green strip. Corresponding microstructures are available in Appendix A.

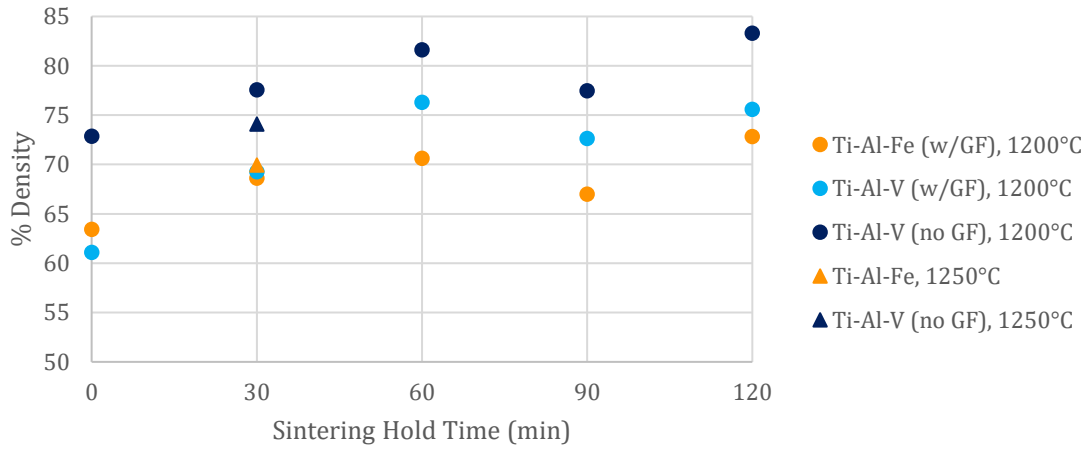


*Figure 6-4. Optical density measurements of samples sintered in the DSC at 1200 °C for various times from 0-120min and at 1250°C for 30min*

Sintering trials for Ti-xAl-yV was performed with strips compacted with and without the use of the 3D printed green feeder part while the Ti-xAl-yFe was compacted using the green feeder only. Comparing the two Ti-xAl-yV data sets, the densities are consistently higher when the feeder was not used as it was determined to restrict powder flow from the hopper to the rolls. For all conditions, density increased as sintering hold times were increased from 0-60 min. There was no notable difference in the density of the samples when sintered for 2 hours compared to 1 hour for any condition. The rate of densification was similar when comparing the Ti-xAl-yV with and without the use of a green feeder. While densities were similar for the different alloys compacted without the green feeder at lower hold times, at 60 min and greater, Ti-xAl-yV showed improved sintered density compared to the Ti-xAl-yFe. Increasing the temperature to 1250°C showed a minimal effect on the Ti-xAl-yFe density and a negative effect on the Ti-xAl-yV as it decreased from 77.57% to 74.10% with a 30 min hold. Note that the green and sintered densities of the RC samples are approximately the same as that of the press and sinter samples under a die compaction pressure of 150 MPa.

The 90-minute data of the above figure, appears lower for all alloys. This may be within the error of measurement. Ultimately, there was no significant benefit to densification by increasing the sintering time past one hour. An expanded discussion including Dilatometry (DIL) to support these conclusions is included in Appendix B.

# Chapter 7: Post Roll Compaction Process Optimization

Sample Set 1 was produced to optimize the sintering, cold rolling and annealing process following roll compaction. For this purpose, Ti-xAl-yFe and Ti-xAl-yV samples roll compacted with the green feeder were studied for comparison. The principal focus at this stage of research was the effect of processing on density, microstructure, and imposed strain resulting from variations in the heat treatments. Throughout this chapter, conditions are labeled as 1 h or 2 h, which refers to the dwell time during sintering after roll compaction. The distinction *S+A* indicates sinter + anneal where an additional 1 h annealing heat treatment was applied between the first and repeat rolling steps and *SO* indicates sinter before rolling only. Both S+A and SO samples undergo a final annealing step.

## 7.1 Density

The initial and final thicknesses ($t_i$ and $t_f$) were used to calculate % reduction. Density was measured optically. Table 7-1 and Table 7-2 show the results for Ti-xAl-yV and Ti-xAl-yFe respectively.

*Table 7-1. Initial and final thicknesses, % reduction, and density for Ti-xAl-yV*

| **Sample** | | **$t_i$** (mm) | **$t_f$** (mm) | **Reduction (%)** | **Density (%)** |
|---|---|---|---|---|---|
| **1h** | S+A | 1.21 | 0.55 | 54.90 | 99.76 |
| **1h** | SO | 1.21 | 0.55 | 54.88 | 99.79 |
| **2h** | S+A | 1.16 | 0.54 | 53.56 | 99.34 |
| **2h** | SO | 1.16 | 0.53 | 54.40 | 99.25 |
| **Ti-xAl-yV Average** | | 1.19 | 0.54 | 54.43 | 99.53 |

*Table 7-2. Initial and final thicknesses, % reduction, and density for Ti-xAl-yFe*

| Sample | | $t_i$ (mm) | $t_f$ (mm) | Reduction (%) | Density (%) |
|---|---|---|---|---|---|
| **1h** | S+A | 1.29 | 0.63 | 51.63 | 98.29 |
| **1h** | SO | 1.29 | 0.57 | 56.13 | 99.38 |
| **2h** | S+A | 1.23 | 0.65 | 47.14 | 97.80 |
| **2h** | SO | 1.23 | 0.60 | 50.99 | 99.20 |
| **Ti-xAl-yFe Average** | | 1.26 | 0.61 | 51.70 | 98.67 |

The amount of reduction achieved, and the resultant densities were more consistent in the Ti-xAl-yV samples compared to the Ti-xAl-yFe, where the variation is greater. In Ti-xAl-yFe, greater reduction achieved does correlate to improved densities; both are higher where the SO rolling path was used. Densities greater than 99% were observed in all Ti-xAl-yV samples but only some of the Ti-xAl-yFe. Sintering with a 2 hour hold time does decrease the initial strip thickness but has no observable affects on the resultant final densities compared to sintering with a 1-hour hold. Mechanical properties, including strength, elongation, fracture toughness, and fatigue are all impacted negatively by porosity [26]. Achieving high densities is a crucial step in optimizing the mechanical properties of the DPR material.

### 7.1.1 Strain

Figure 7-1 shows the relationship between strain imposed during cold rolling and resulting density for both alloys processed with different heat treatments. Sintered density of the strips is plotted as 0% strain.

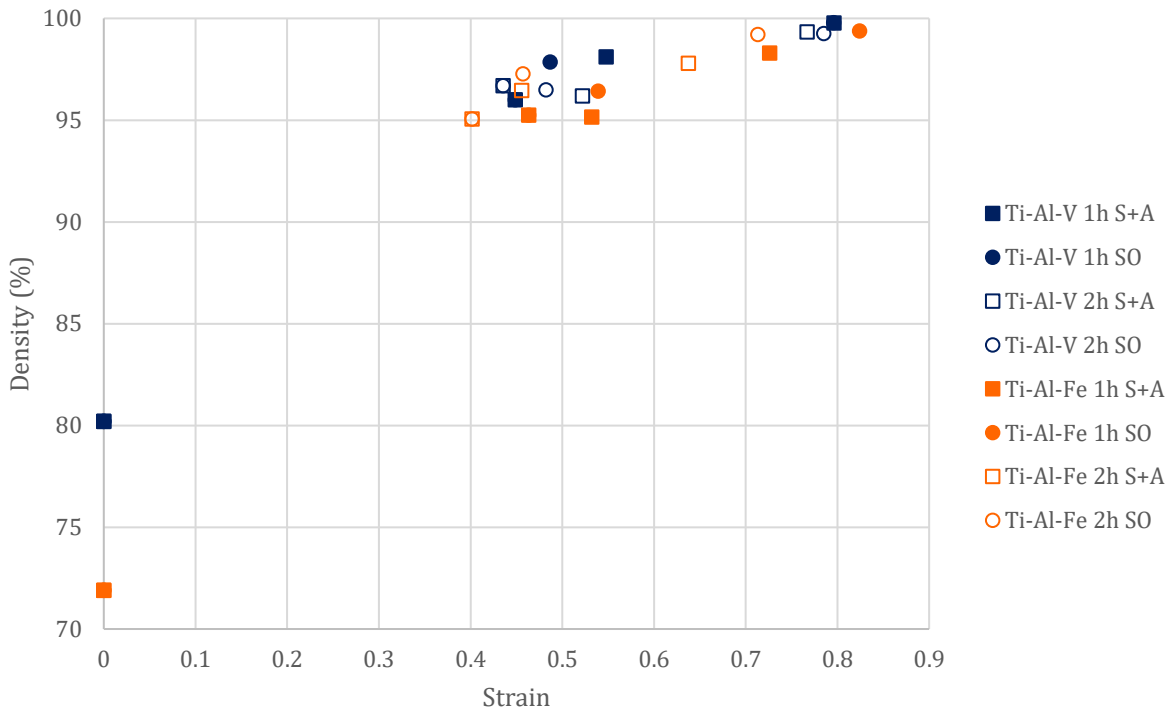


*Figure 7-1. Strain vs. density for Sample Set 1*

Despite using an equivalent roll force during roll compaction, the Ti-xAl-yV alloy yields a higher sintered density than the Ti-xAl-yFe. This is consistent with the preliminary sintering data of Figure 6-4. After only the first rolling step, ending with a pass at 0.05 mm GW, the disparity in sintered density is overcome and both alloys achieve densities of 95 to 96% theoretical. With subsequent reduction steps, increasing reduction strain results in increased density reaching greater than 99%. The amount of strain imposed on the Ti-xAl-yV samples is very consistent; note that the final data point for the Ti-xAl-yV 1h SO sample is directly behind that of Ti-xAl-yV 1h S+A and so is not visible. It can be concluded that densification during cold rolling is not influenced by the absence or presence of an intermediate annealing step. There appears to be a slightly better densification performance for samples that had only a 1 hour sintering step after roll compaction but before cold rolling.

## 7.2 Microstructure

### 7.2.1 Optical

Figure 7-2 shows the full cross section of the Ti-xAl-yFe 1h S+A sample as an example of an unetched microstructure following the final cold rolling step. The density is consistent throughout the majority of the sample, although the porosity does begin to increase approximately 1 mm from each edge.


*Figure 7-2. Ti-xAl-yFe 1h S+A full strip thickness after the final cold rolling step*

Four micrographs are given in Figure 7-3 which show one half of sample cross widths for a variety of Ti and Ti-alloys. Equivalent rolling force and speed was used during the roll compaction of each sample. Gap width was automatically adjusted to achieve the desired force in both cases. In all cases, sintering was performed under flowing argon atmosphere to 1200°C with heating rates of 5 K/min.

Ridged rolls were used to produce a strip of CP-Ti by O'Flynn in Figure 7-3 (a) [29]. There was no hold time at the sintering temperature for this sample. Cold rolling was performed in 0.1 mm steps with a final roll gap of 0.1 mm resulting in a strip thickness of approximately 0.9 mm. Figure 7-3 (b) and (c) are Ti-xAl-yFe and Ti-xAl-yV with a die and punch style set of rows in addition to the 3D printed green feeder part to direct powder flow from the hopper to the center of the rolls. Final strip thicknesses for (b) and (c) were 0.57 and 0.55 mm respectively. Figure 7-3 (d) is a Ti-xAl-yV sample also rolled with the die and punch rolls but without the green feeder which yielded a final thickness of 0.65 mm.

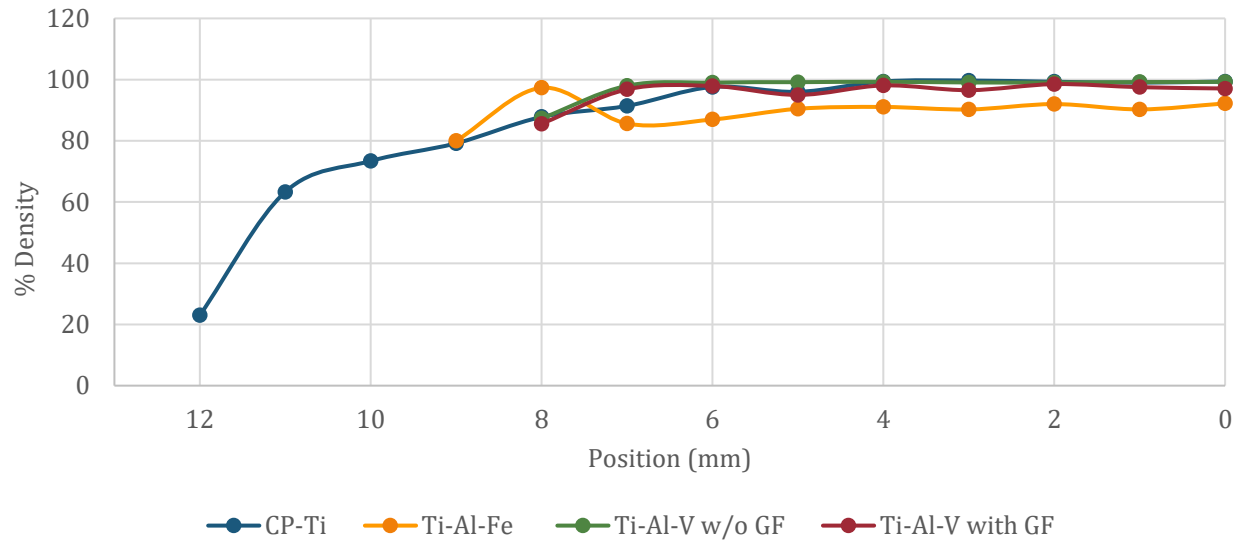


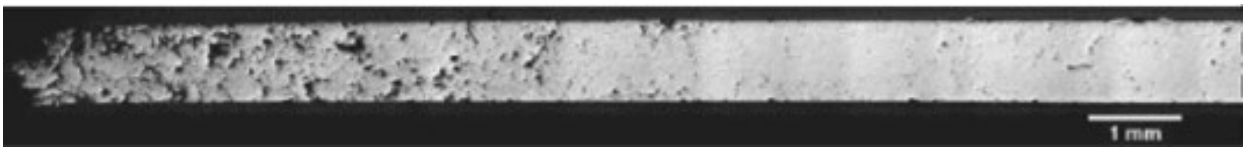


(a)

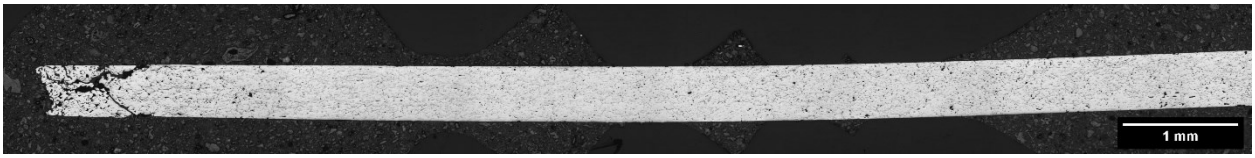


(b)

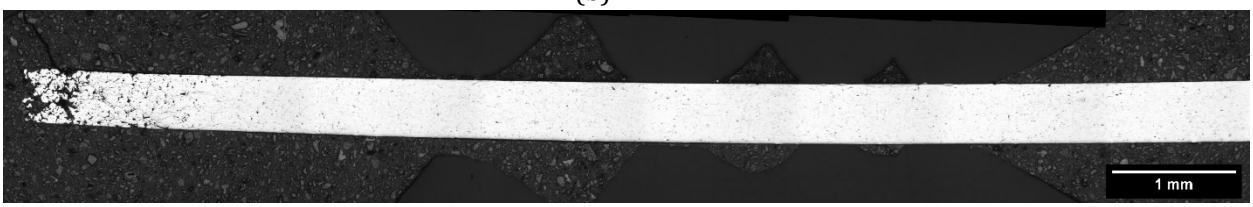


(c)

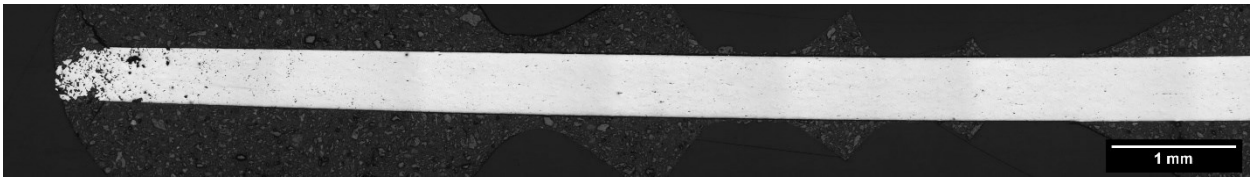


(d)

*Figure 7-3. Optical density from four micrographs of titanium and Ti-alloy roll compacted strips (a) CP-Ti with ridged rolls from [29] (b) Ti-xAl-yFe with die & punch and green feeder (c) Ti-xAl-yFe with die & punch and green feeder (d) Ti-xAl-yV with die & punch, without green feeder*

Samples (b) through (d) were produced by H. Kauffman. The green strips were then sintered and cold rolled as part of the current research. The (b) and (c) samples

with the 1h SO rolling path were chosen for this analysis as this path most closely matched that used to produce the CP-Ti sample. Sample (d) followed the S+A roll path. Optical density was used to measure the gradient of porosity across the samples at 1mm intervals which is also plotted in Figure 7-3 where the origin is at the mid-point of the sample (right side). Note that when die and punch rolls are used, the produced strips are approximately 4 mm narrower than when using the ridged rolls, resulting in differing scales of the images.

The implementation of the die and punch rolls does produce narrower green strips compared to the horizontally ridged rolls used in the CP-Ti study. When using the ridged rolls, the outermost regions of the CP-Ti were not significantly densified during rolling and would ultimately need to be removed, requiring an extra step in the production process, and increasing the amount of waste material. Implementing the die and punch is beneficial from both environmental and economical perspectives, since there is less material with insufficient density which must be removed.

The Ti-xAl-yV samples (c) and (d) both have comparable densities to the CP-Ti sample, although when rolled without the green feeder, the density is slightly more consistent while also producing a thicker strip. Ti-xAl-yFe sample (b), where the green feeder was also used, had yielded slightly lower densities compared to Ti-xAl-yV. The purpose of the green feeder addition into the hopper was to further guide the powder towards the center of the rolls and eliminate density gradients. Large portions of the flanges were able to be removed manually while the strips were still in the green state, and any remaining flange was flattened in the initial rolling step. The desired benefits of eliminating flanges and reducing gradients was not achieved using the GF; however,

it did appear to hinder the flow of the powder from the hopper reducing thickness and density. For future rolling not using the green feeder was preferred.

### 7.2.2 Ti-xAl-yV SEM

SEM was used to obtain a high magnification image of the microstructure of Ti-xAl-yV after the final annealing step following full cold rolling. The sample presented in Figure 7-4 was sintered for 1 hour and rolled without an intermediate annealing step. Six locations are marked where EDS (Energy Dispersive X-Ray Spectroscopy) spot analysis was performed, and results are presented in Table 7-3. An area scan of the micrographed region was also performed with results presented in Table 7-4.

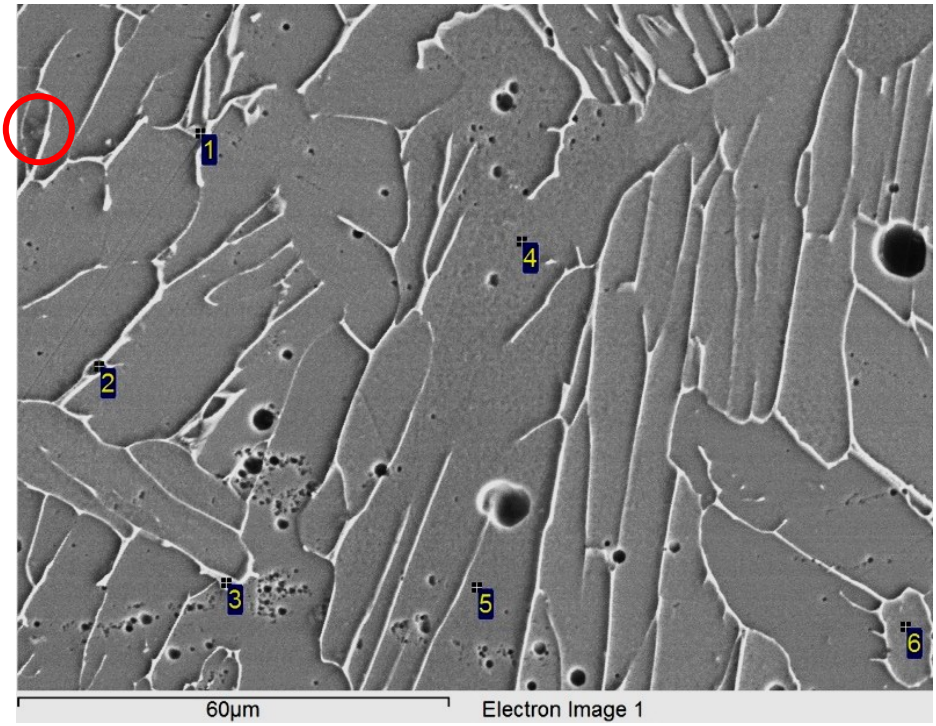


*Figure 7-4. SEM image of Ti-xAl-yV sintered for 1 hour SO*

*Table 7-3. EDS spectrum collected of spot scans of Ti-xAl-yV 1h SO at locations indicated in Figure 7-4 wt%*

| Location/Element | Al | Ti | V | Fe |
|---|---|---|---|---|
| **1** | 2.49 | 92.30 | 5.21 | – |
| **2** | 1.50 | 83.46 | 13.73 | 1.32 |
| **3** | 1.65 | 88.98 | 9.36 | – |
| **4** | 4.02 | 94.62 | 1.36 | – |
| **5** | 3.97 | 96.03 | – | – |
| **6** | 3.92 | 94.64 | 1.44 | – |

*Table 7-4. EDS spectrum collected over entire area of f Ti-xAl-yV 1h SO presented in Figure 7-4*

| Element | wt% | at% |
|---|---|---|
| **Al** | 3.67 | 6.34 |
| **V** | 2.80 | 2.56 |
| **Ti** | 93.53 | 91.10 |

For both spot and area scans, carbon was also detected; however, SEM-EDS is unable to perform adequate quantitative analysis of carbon and is therefore omitted from the analysis. Carbon was not purposely introduced as an alloying element it is not included in the quantitative analysis above. Results were normalized to elements Al, V, and Ti.

Qualitatively, the mapping feature of EDS was also used. The maps for aluminium, vanadium and carbon are given in Figure 7-5 for the same region as Figure 7-4. As expected, higher concentrations of vanadium are observed at the boundaries and higher concentrations of aluminium within the grains. The carbon is primarily concentrated in what appears to be the remnants of carbide impurities in the material and at grain boundaries. A clear example of carbon concentration can be identified in the carbon map in Figure 7-5 and is indicated by the red circle. A carbide in the corresponding location on the micrograph in Figure 7-4 is also highlighted. Note that

the bulk analysis of the area imaged in Figure 7-3 indicates a lower alloy composition than that of the target composition, Ti-6Al-4V. This will be discussed in more detail in Section 8.2.

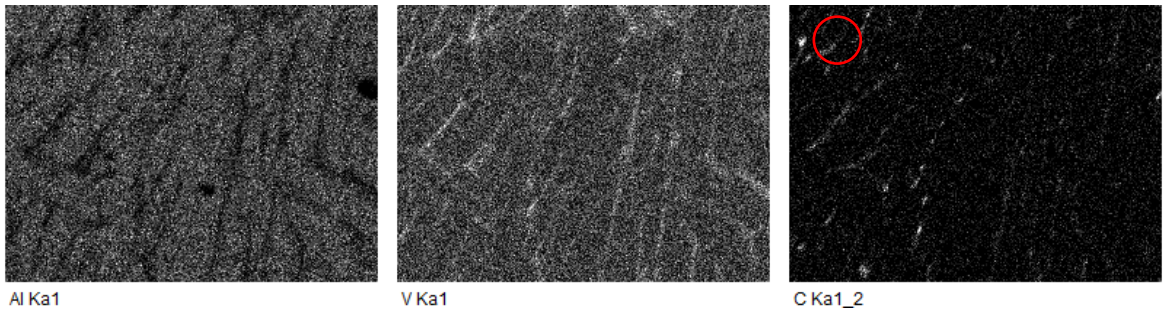


*Figure 7-5. EDS map results for Al, V, and C elements in Ti-xAl-yV for region shown in Figure 7-4*

### 7.2.3 Ti-xAl-yFe SEM

Figure 7-6 shows the SEM micrograph of Ti-xAl-yFe with six locations noted where EDS spot scans were performed. These results are presented in Table 7-5 along with an area scan of the full region in Table 7-6. Both sets of results are normalized to Al, Fe, and Ti.

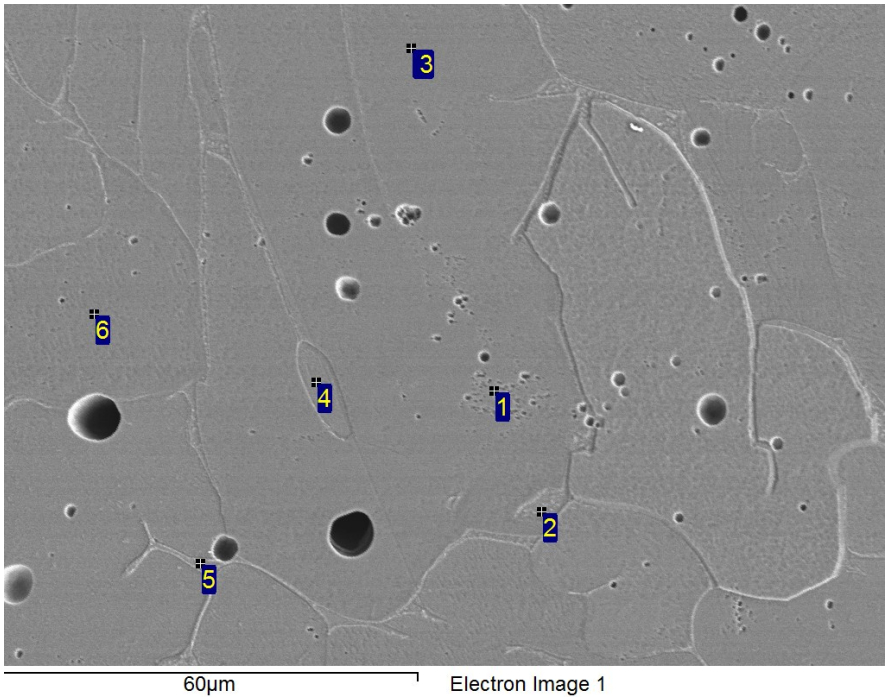


*Figure 7-6. SEM image of Ti-xAl-yFe sintered for 1h SO*

The β-Ti phase and grain boundaries in general are less prominent in the Ti-xAl-yFe microstructure shown in Figure 7-6 compared to Ti-xAl-yV in Figure 7-4. This may be partially attributed to there being a lower composition of β-Ti in this alloy resulting in less defined grain boundaries; however, it is at least partially related to the elemental contrast differences in the SEM. Iron and vanadium are both β-stabilizers which concentrate in the β phase; as Fe has a more similar atomic weight to titanium, it shows less contrast compared to vanadium in titanium.

*Table 7-5. EDS analysis of spot scan locations identified in Figure 7-6 in wt%*

| Location/Element | % Al | % Fe | % Ti |
|---|---|---|---|
| **1** | 3.49 | – | 96.51 |
| **2** | 1.01 | 19.66 | 79.34 |
| **3** | 3.35 | – | 96.65 |
| **4** | 3.38 | – | 96.62 |
| **5** | 0.75 | 21.56 | 77.69 |
| **6** | 3.34 | – | 96.66 |

*Table 7-6. EDS analysis of area scan over entire region presented in Figure 7-6 in wt% and at%*

| Element | Wt% | At% |
|---|---|---|
| **Al** | 3.18 | 5.53 |
| **Fe** | 1.88 | 1.57 |
| **Ti** | 94.94 | 92.90 |

The mapping function of EDS was also performed for the sample area of Ti-xAl-yFe shown in Figure 7-6. The results for Al, Fe, and C are given in Figure 7-7.

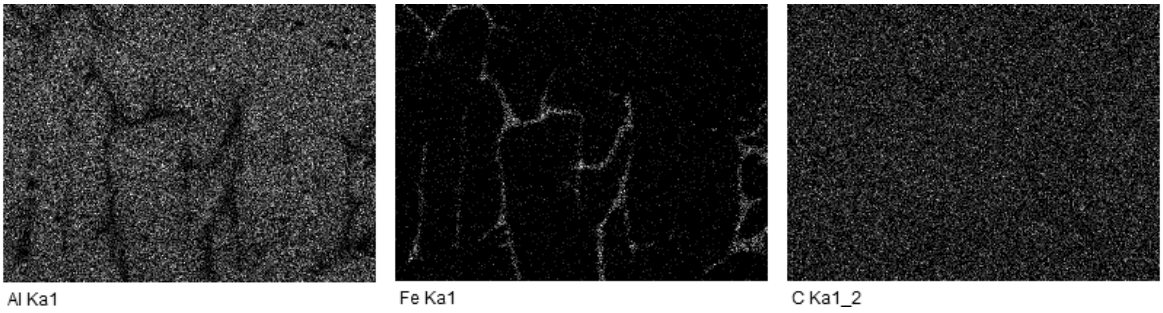


*Figure 7-7. EDS mapping analysis for Ti-xAl-yFe for region shown in Figure 7-6*

As expected, the concentration of Al in the grain boundaries is depreciated and that of Fe is elevated as they are α and β stabilizing elements respectively. The distribution of carbon in this alloy does not appear to be concentrated in any way or dependent on the microstructural features unlike in the Ti-xAl-yV. indicating that any levels measured by EDS can be attributed to regular sources of contamination. Again Table 7-6 indicates a bulk composition below the target composition of Ti-5Al-2.5Fe which will be discuss in more detail later in the thesis.

## 7.3 Grain Size

The grain size was measured from the polished cross section of the rolled strips after the final cold rolling step at a preloaded 0 GW and after the final annealing step. Table 7-7 shows these grain size measurements and the percent growth was calculated by (14):

$$\%\ growth = \frac{GS_f - GS_i}{GS_i} * 100 \tag{14}$$

*Table 7-7. Grain size measurement of sample cross sections*

| Alloy | Sinter Time (h) | Heat Treatment | Grain Size (μm) | | % Growth |
|---|---|---|---|---|---|
| | | | Before | After | |
| Ti-xAl-yV | 1 | S+A | 23.82 | 42.54 | 78.63 |
| | | SO | 18.60 | 34.52 | 88.05 |
| | 2 | S+A | 31.18 | 38.37 | 23.08 |
| | | SO | 21.15 | 31.63 | 49.57 |
| Ti-xAl-yFe | 1 | S+A | 24.02 | 31.81 | 32.46 |
| | | SO | 20.52 | 31.36 | 52.86 |
| | 2 | S+A | 16.99 | 20.79 | 22.35 |
| | | SO | 22.91 | 35.64 | 55.52 |

The % growth was greater in the SO samples due to the larger amount of cold work energy stored in these samples compared to the S+A which experienced an intermediate annealing step. Increased cold work has been quantitatively shown to reduce the activation energy of recrystallization in Ti and Ti-alloys as well as create dislocations and vacancies within the material [52], [53]. During annealing, these act as nucleation sites for dislocation free grains during recrystallization and results in a finer grain size distribution. Smaller grain size leads to a larger driving force during the grain growth stage which occurs after recrystallization. This, combined with the higher activation energy to achieve grain growth in the larger grains of the S+A material results in the more significant growth of SO samples.

The density and particularly the shape of the porosity in the samples prior to the final anneal may also have some effect. Figure 7-8 compares the microstructure after the final rolling step for two Ti-xAl-yFe samples. The SO samples which experienced no heat treatment during the cold rolling process have elongated, sharp pores from the shearing which occurs during deformation. In the case of S+A samples, much of the porosity has been rounded and some has been closed off prior to the final rolling steps.

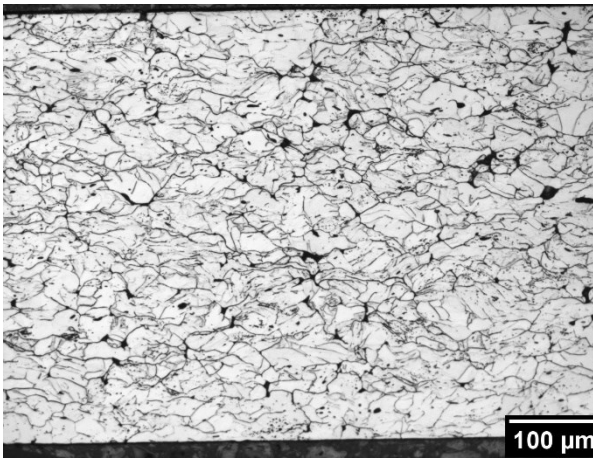


(a)

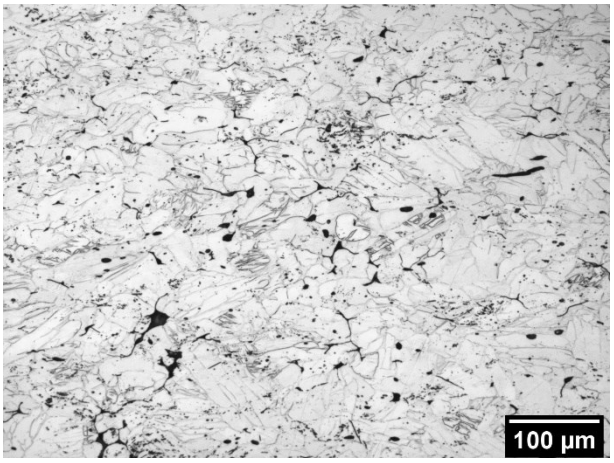


*(b)*

*Figure 7-8. Etched micrographs of Ti-xAl-yFe after final rolling step rolled under path (a) 1h SO and (b) 1h S+A*

As a result of the different heat treatments during rolling, the SO samples would have more surface area prior to the final annealing step throughout the bulk of the material where diffusion occurs at a notably higher rate. The driving force to close and make round the sharp porosity would also be greater in the SO compared to the S+A samples during the final anneal.

## 7.4 Sintering Support Observation

During sintering of strips, they were placed on their sides in the alumina crucible supported by zirshot, which are ceramic beads with a mesh size of -425, +300. After sintering when samples were removed from the furnace and from the crucible, zirshot beads were stuck to the sides of the strips. They were easily removed by brushing with a plastic bristle brush and light pressure. Small indents were observed on this side of the samples. Later, during rolling, crack initiation and propagation was observed to occur preferentially on these sides of the samples as shown in Figure 7-9. This did not appear to be an issue during the annealing stages at either intermediate or end stages

of the rolling procedure as the density of the strips were much higher and much less shrinkage and densification was occurring during the subsequent heat treatments.

*Figure 7-9. Photograph of preferential cracking example on cold rolled samples*

There is some cracking visible in this sample on the top edge of this sample, although it is contained to the outermost 1-2 mm and is parallel to strip rolling direction. This is likely the effects of flattening any remaining flange left over from the roll compaction step. On the bottom edge of the sample which was submerged in the zirsot during the initial sintering treatment, major cracking occurred and are circled in Figure 7-9. These cracks protrude sometimes over half of the width through the sample at angles close to 45°. Moving to the comb shaped wrought Ti sheet support described in the procedure contributed to eliminating this cracking issue.

# Chapter 8: Processing, Microstructure, and Property Relationships for Direct Powder Rolling of Titanium Alloys

## 8.1 Rolling Response

Table 8-1 is a reference for variations of the rolling paths being examined and the data markers used on plots throughout this chapter. A square indicated that an intermediate anneal heat treatment was performed and a circle indicates no anneal. A hollow marker indicates when the repeat rolling step, consisting of two passes at 0.05 mm GW was performed and a filled marker indicates no repeat roll step. The Ti-xAl-yV alloy data is shown in navy and Ti-xAl-yFe in orange.

*Table 8-1. Summary table of data markers*

| Symbol | Roll Path | Includes Repeat roll | Includes Mid-Anneal |
|---|---|---|---|
| ■ ■ | A | No | Yes |
| □ □ | B | Yes | Yes |
| ● ● | C | No | No |
| ○ ○ | D | Yes | No |

### 8.1.1 Reduction and Density

The observed density and cumulative % reduction of samples produced with the intermediate anneal are plotted in Figure 8-1 and for those without plotted in Figure 8-2. On both plots, the arrows overlayed on the graph show the range over which the data points are attributed to a particular step in the roll reduction. Samples rolled via Paths B and D have the additional repeat rolling step and are represented by closed data points on the plots in Figure 8-1 and Figure 8-2. There is some overlap between some

of the repeat roll step reductions with the ranges of the first and final roll steps, particularly for samples in Paths C and D.

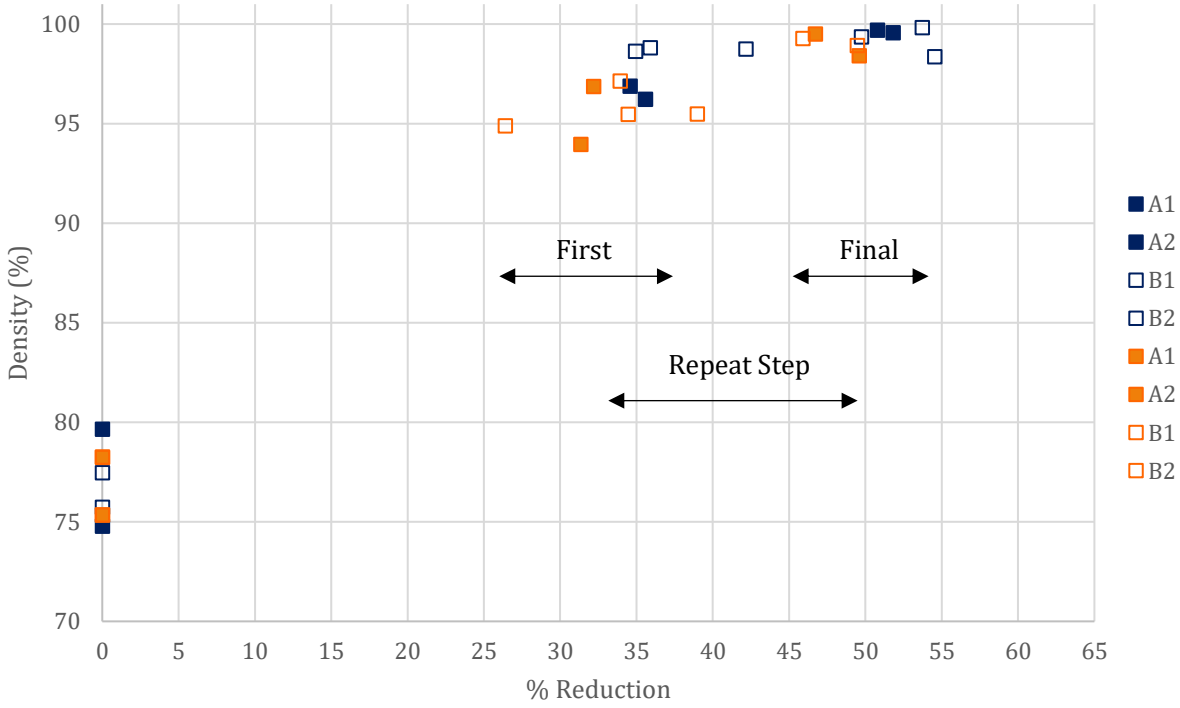


*Figure 8-1. % Reduction vs. density for rolling Paths A and B (with intermediate anneal)*

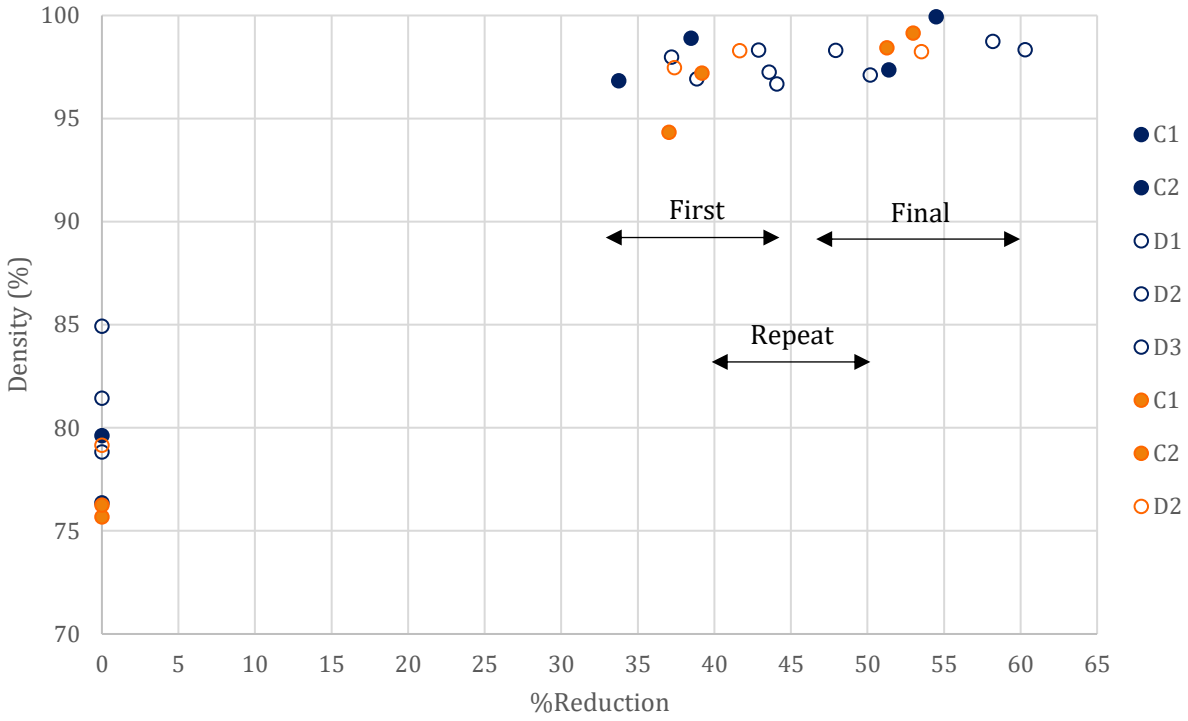


*Figure 8-2. % Reduction vs. density for rolling Paths C and D (without intermediate anneal)*

Whether the intermediate anneal is performed or not, the addition of two additional passes at 0.05mm in the repeat roll step result in increased % reduction compared to the same alloy rolled via Paths A and C. However, final densities after the final rolling step do not appear highly dependent on the presence or absence of the repeat rolling step.

The observed reductions are slightly less in the Path A and B samples than the C and D samples starting with the first rolling step and following through to the final rolling step. However, for all of Paths A, B, C, and D the first rolling step is identical. Therefore, the trend of increased reduction in the first rolling step of Path C and D series is likely due to experimental variations.

Comparing the data of the above two figures indicate that the final densities after cold rolling are higher when an intermediate anneal is included. This may be partly due to some sintering densification that took place during the annealing step. It also appears that less total reduction is needed to achieve the higher densities in the intermediate annealed samples. However, this may be due to the experimental variation mentioned above where the Path A and B data sets appear to be shifted to lower reduction ranges overall.

In an attempt to isolate the influence of the intermediate annealing on the subsequent rolling steps, Table 8-2 shows the average % reduction achieved by all the rolling paths with the first roll reduction values removed. The data of Table 8-2 indicates that there is no consistent trend between level of reduction and intermediate annealing.

*Table 8-2. % Reduction achieved during final roll step in Paths A and C or during cumulatively during repeat and final roll steps in Paths B and D*

| | **Ti-xAl-yV** | **Ti-xAl-yFe** |
|---|---|---|
| **A** | 16.22 | 16.39 |
| **B** | 20.21 | 17.25 |
| **C** | 16.82 | 14.00 |
| **D** | 15.59 | 17.99 |

After the final annealing step performed on the sheets of paths A, B, C, and D the sintered densities fell with the range of 98.74-99.57% in Ti-xAl-yV samples and 98.55-99.15% in the Ti-xAl-yFe alloy. The full evolution of density for all samples after processing samples is given in Appendix C.

### 8.1.2 Microhardness Evolution During Processing

In hardness testing performed by other researchers at Dalhousie University using the NANOVEA PB1000 machine, most consistent and reliable results were obtained when the sample was flat and polished to a mirror finish on both sides. This was not feasible for material in this study due to the thin gauge of the roll compacted sheets, in addition to small depth of some samples due to the need to conserve total strip length for tensile testing. For these reasons, the sample remained mounted in bakelite and only one side was polished to the mirror finish. The effects of the unideal sample preparation were mitigated by performing testing as close to the middle of the sample as possible as well as choosing an appropriate load and loading rate. Further, all samples have the same method of preparation, increasing the confidence in the data comparison between samples for the purposes of this research.

Initial testing was performed on the wrought Ti-6Al-4V as received material using a range of load forces with the one-sided preparation method. The goal was to create an indent as small as possible so that the effects of the bakelite on the relatively thin sample would be minimized. Initial indents were created using 0.5 N however the resolution of the loading curve was too low, and the results were highly varied and greatly influenced by human error. Using an increased load of 2.5 N, 12 indents were performed on the wrought as-received Ti-6Al-4V where the average was 345 HV with a standard deviation of 38 HV. This is very close to the reported hardness of 349 HV in the AMS Handbook [20], verifying the procedure for the purposes of this research.

The two rolling Paths A and C, which do not include the additional repeat roll were selected for hardness testing. The evolution of hardness for both roll compacted alloys and the wrought Ti-6Al-4V was examined by testing samples procured after each

rolling step. The average testing values are presented below in Figure 8-3. The wrought Ti-6Al-4V includes the additional material conditions of the as received material and after the initial annealing heat treatment which was performed to simulate the sintering step prior to cold rolling. Only the roll compacted samples rolled via Path A have an intermediate annealing step. Ti-xAl-yFe data is offset slightly to the left and Ti-xAl-yV slightly to the right of the wrought Ti-6Al-4V data point so that error bars and overlapping data points are clearly visible. Error bars indicate the maximum and minimum hardness values measured from each sample.

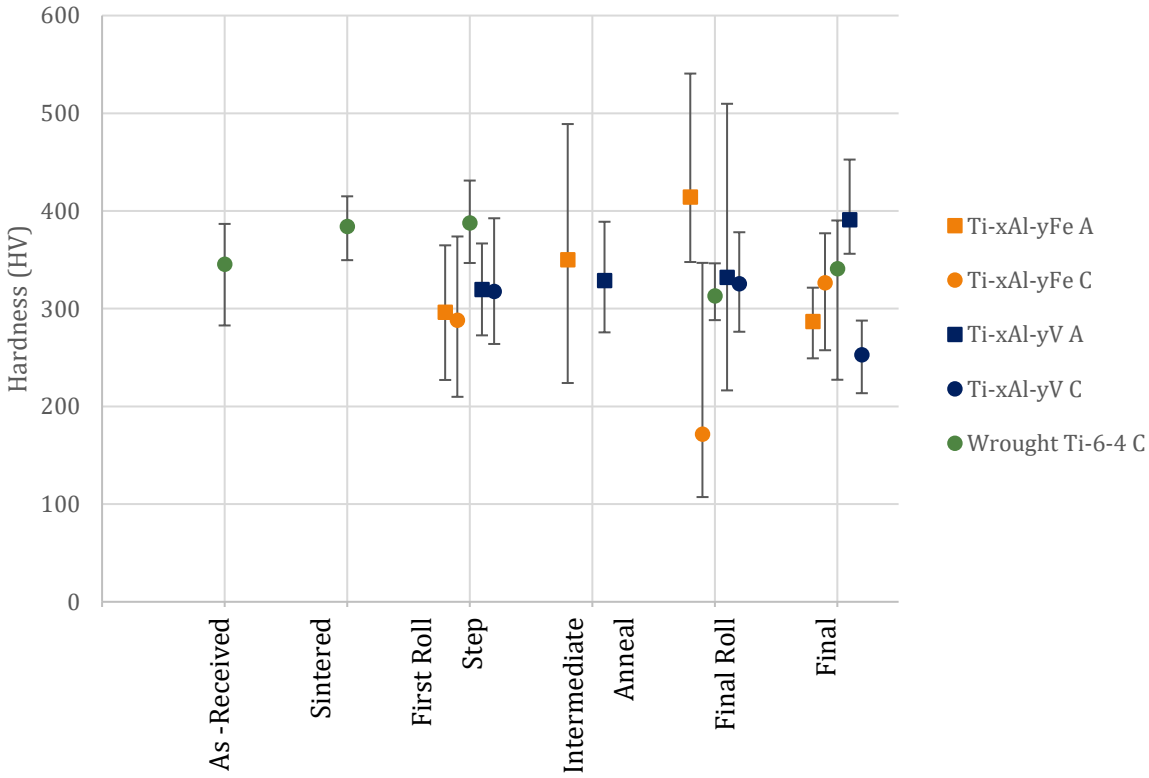


*Figure 8-3. Average hardness measurements after each step of the roll path*

Standard deviations of rolled wrought Ti-6Al-4V samples with the one-sided sample preparation ranged from 20-49 HV which was deemed an acceptable level of variation.

The inclusion of the intermediate annealing step does not appear to have an immediate effect on the Ti-xAl-yV A material as hardness is consistent between the first roll, intermediate anneal, and final roll steps. Values of Ti-xAl-yV C are also very similar to each other after the first and final rolling steps and to Ti-xAl-yV A. This is consistent with the data of the wrought Ti-6Al-4V alloy whose hardness is also not very sensitive to cold work or final annealing.

As titanium has an HCP crystal structure, it has fewer slip systems relative to BCC or FCC crystal structures. Fewer slip systems limit the paths on which dislocations can pile-up as a result of cold work imparted by the plastic deformation of cold rolling. This results in a low strengthening affect from cold working. Limited cold work which is achievable would occur in the initial rolling passes after sintering and initial annealing, but if maximum strengthening is occurring during a single rolling step, this would account for very similar hardness values throughout processing prior to the final annealing heat treatment. Following the final anneal, however, the hardness values diverge, However, this divergence seems to lie within the error range of the test.

A notable outlier in the data is the Ti-xAl-yFe alloy after the final roll step. The average hardness measured was 171 HV while the same material which underwent the intermediate annealing step shows the highest observed hardness at 414 HV. The indents of the Ti-xAl-yFe C after the final roll step were then examined under the optical microscope and images are shown below in Figure 8-4.

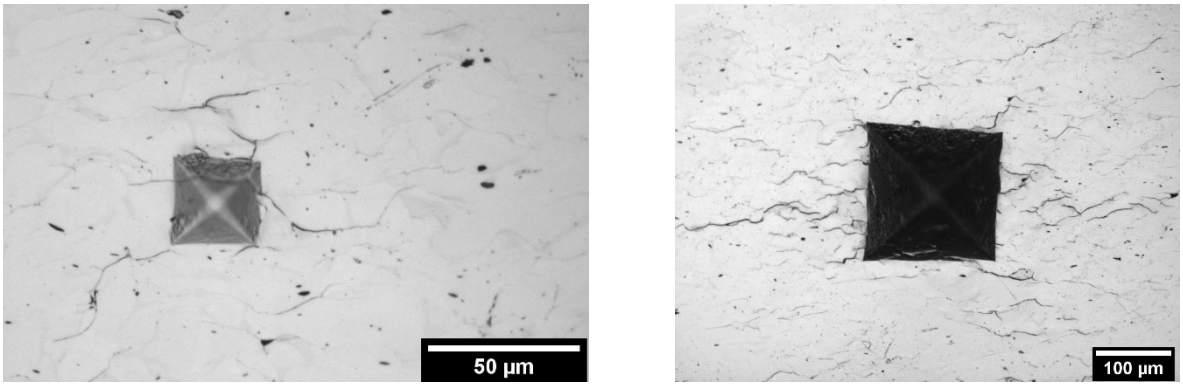


(a) (b)

*Figure 8-4. Micrographs of Vickers hardness indents in Ti-xAl-yFe C (a) 2.5N force at 50x magnification (b) approximately 30N force at 20x magnification*

Image Figure 8-4(a) shows one of the standard test indents using 2.5 N force. Even with this relatively low force, there are clearly cracks propagating from the indent. In Figure 8-4(b) an indent placed manually with a higher load of approximately 30 N shows the same, while more exaggerated cracking.

This material has undergone maximum amount of cold work during the rolling process but no heat treatments since the initial sintering step following compaction of the powders, at which the material had a relatively low density and many pores remaining. A schematic of the grain deformation which occurs during rolling is shown in Figure 8-5. Relatively equiaxed pores become flatter and more elongated along the rolling direction; this also applies to the porosity between grains where pores appear closed, but material is not necessarily fused. The deformation resulting from the cold work mechanically increases density.

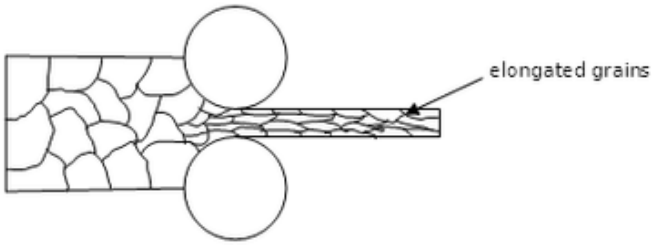


*Figure 8-5. Schematic of grain deformation during rolling [54]*

Figure 8-6 is a comparison of the microstructure of Ti-xAl-yFe after the final rolling step and after the final heat treatment. Porosity appears closed yielding high density measurements in Figure 8-6(a), and while some cold fusion has potentially occurred, the porosity is not healed until the following annealing heat treatment allows for a higher degree of material fusion.

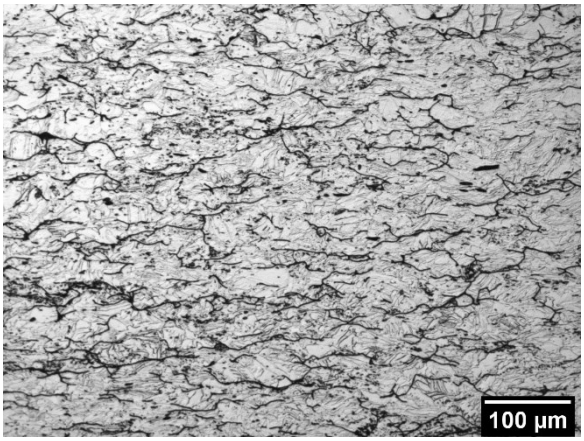


(a)

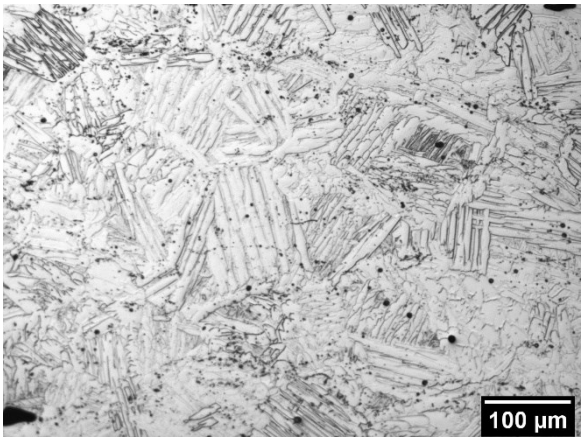


(b)

*Figure 8-6. Comparison of microstructures for Ti-xAl-yFe rolled via Path D (a) after the final rolling step and (b) after the final anneal*

This intergranular cracking is likely the cause for the low values reported for the Ti-xAl-yFe C final roll condition. The true hardness value of is likely similar if not higher than Ti-xAl-yFe A. Some mild cracking is observed in the Ti-xAl-yV final roll condition, as shown in Figure 8-7, but not to the same extent as in the Ti-xAl-yFe.

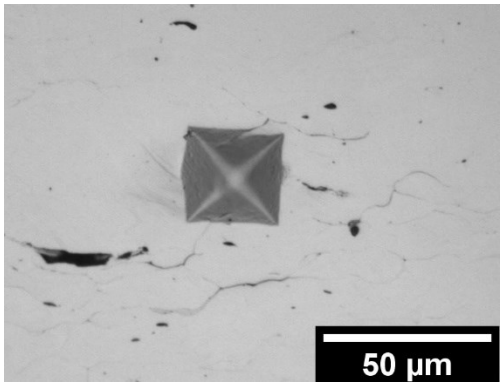


*Figure 8-7. Micrograph of 2.5N Vickers hardness indent in Ti-xAl-yV C roll compacted sample after the final rolling step*

Hardness values in the final condition are listed in Table 8-3. It was expected that the Ti-xAl-yFe would have lower hardness than the Ti-xAl-yV considering the reported hardness for the target alloys of Ti-5Al-2.5Fe and Ti-6Al-4V which were 268 and 349 HV respectively [20], [22]. When rolled via Path C, the Ti-xAl-yFe is comparable to the expected hardness; however, when rolled via path A, the observed hardness is greater than both roll compacted Ti-xAl-yV material and Ti-6Al-4V of literature.

*Table 8-3. Average hardness values and standard deviations for roll compacted and wrought materials following the final annealing heat treatment*

| Material | Roll Path | Hardness | Standard Deviation |
|---|---|---|---|
| **Ti-xAl-yV** | A | 287 | 33.0 |
| | C | 326 | 22.4 |
| **Ti-xAl-yFe** | A | 391 | 20.1 |
| | C | 253 | 38.0 |
| **Wrought** | C | 356 | 24.0 |

## 8.2 Material Composition

### 8.2.1 Wrought

The composition of the ingot from which the wrought Ti-6Al-4V sheet was obtained is presented in Table 8-4. This composition is an average of two

measurements taken from the top and the bottom of the ingot from which the sheet was produced. Testing was performed at TIMET [55] and results were provided by the manufacturer. This is considered the chemical composition of the wrought sheet in the as-received condition.

*Table 8-4. Elemental analysis of the wrought Ti-6Al-4V ingot performed by McMaster-Carr [55]*

| **Element** | **Fe** | **V** | **Al** | **C** | **O** | **N** | **Ti** |
|---|---|---|---|---|---|---|---|
| **%wt** | 0.13 | 3.94 | 6.4 | 0.0285 | 0.2 | 0.0075 | Bal. |

Additionally, inert gas fusion was performed to determine hydrogen content. In the as-received condition 50 ppm was measured [55].

Laser Ablation Inductively Coupled Plasma Mass Spectroscopy (LA-ICPMS) was performed at Dalhousie University by the MEC on pieces of material cut from the end of the fractured tensile bars. This allowed direct correlation of composition and measured tensile properties. Other elements were detected, however only in trace quantities. The results in Table 8-5 are normalized relative to titanium, aluminium, and vanadium. Duplicate testing was performed on the wrought Ti-6Al-4V. Averages of the three samples and standard deviations are presented.

*Table 8-5. Normalized LA-ICPMS results for wrought Ti-6Al-4V material*

| | **Al** | **V** | **Ti** |
|---|---|---|---|
| **Average** | 6.31 ± 0.03 | 3.80 ± 0.07 | 89.89 ± 0.08 |

Values for aluminium and vanadium are consistent between the ingot and tensile strip.

### 8.2.2 LA-ICPMS of Roll Compacted Samples

The results of LA-ICPMS are presented for the Ti-xAl-yV and Ti-xAl-yFe roll compacted samples in Table 8-6 and Table 8-7 respectively. Results are again normalized to titanium, aluminium, and iron or vanadium. Standard deviations are presented for the four samples which have duplicates.

*Table 8-6. Normalized LA-ICPMS results for roll compacted Ti-xAl-yV samples*

| | Al | V | Ti |
|---|---|---|---|
| **A1** | 5.20 ± 0.23 | 3.45 ± 0.17 | 89.81 ± 1.08 |
| **B1** | 6.27 | 4.26 | 89.41 |
| **C1** | 4.34 | 2.96 | 92.63 |
| **C2** | 3.20 ± 0.39 | 2.10 ± 0.99 | 95.94 ± 1.28 |
| **D1** | 2.71 | 1.83 | 95.41 |
| **D2** | 2.53 | 1.73 | 95.70 |
| **D3** | 4.47 | 3.04 | 92.43 |
| **Average** | 4.10 ± 1.37 | 2.77 ± 0.93 | 93.05 ± 2.75 |

*Table 8-7. Normalized LA-ICPMS results for roll compacted Ti-xAl-yFe samples*

| | Al | Fe | Ti |
|---|---|---|---|
| **A2** | 2.61 ± 0.29 | 3.36 ± 0.59 | 92.80 ± 1.44 |
| **B2** | 1.13 | 1.48 | 97.38 |
| **C1** | 2.77 | 1.90 | 95.32 |
| **C2** | 1.09 ± 0.04 | 1.48 ± 0.06 | 96.96 ± 0.33 |
| **D2** | 1.69 | 1.46 | 96.84 |
| **Average** | 1.86 ± 0.80 | 1.93 ± 0.82 | 95.86 ± 1.88 |

As expected, the homogeneity of the wrought material is more consistent than the roll compacted powder. The variance in chemical composition throughout the compacted powder samples has also been suggested during EDS analysis of samples created during the first set of roll compaction as well as observations of effects in the microstructures. The origins of this compositional variation are speculated to be a result of experimental design be discussed further in Section 10.2.

### 8.2.3 Oxygen Content

Table 8-8 presents the oxygen analysis for the as-mixed Ti-xAl-yV powder prior to roll compaction and sintering, the wrought Ti-6Al-4V sheet after the full treatment of sintering, cold rolling and the final anneal, and fully processed Ti-xAl-yV and Ti-xAl-yFe materials for all four processing paths.

*Table 8-8. Average oxygen content measured in powder, wrought, and roll compacted materials.*

| Material | | Average (ppm) |
|---|---|---|
| **Ti-xAl-yV Powder** | | 1962.05 |
| **Wrought Ti-6Al-4V** | | 1902.16 |
| **Ti-xAl-yV** | A | 2715.63 |
| | B | 2818.53 |
| | C | 2534.41 |
| | D | 3078.01 |
| **Ti-xAl-yFe** | A | 3121.06 |
| | B | 2628.56 |
| | C | 3783.28 |
| | D | 2978.26 |

For the wrought sheet, the average of three tests yielded an oxygen content of 0.1902%, which is both within the ASTM specifications for Grade 5 titanium (Ti-6Al-4V) and lower than the oxygen composition measured in the ingot. In the final condition, the tensile strip has undergone two 1-hour heat treatments in the Sentrotech furnace at 1200°C. Even at this elevated temperature for an extended period of time, there is negligible oxygen pickup by the wrought Ti-6Al-4V sheet, confirming that a very low $O_2$ content is achievable when sintering in the Sentrotech furnace with flowing high purity Ar.

Grade 5 Ti has a maximum oxygen limit of 0.2 wt% [20]; 0.33 wt% O has been cited as a critical level of oxygen, above which the loss of ductility occurs at a much more

severe rate [2]. Of the rolled samples, only the wrought sheet satisfies the requirement of 0.2 wt%. The mixed, pre-compacted Ti-xAl-yV powder contained 0.1962% O, which is within this specification. It should be noted that the oxygen content of the 60Al:40V master alloy (MA) powder used to make the Ti-xAl-yV powder blend was previously measured to be 0.25 wt% oxygen [39]. Given the 10% mass fraction of the MA powder used in the Ti-xAl-yV powder blend allows the oxygen content of the CP-Ti powder to be determined as 0.19%, slightly lower than the bulk blend analysis. Rolled strips of the Ti-xAl-yV made from the Ti-xAl-yV powder blend had oxygen contents ranging from 0.2534-0.3078% O which corresponds to 33-62% increase from the original powder.

The oxygen content of the elemental Al and Fe used to create the Ti-xAl-yFe powder blend has been previously measured to be 0.54 wt% [46] and 1.0 wt% [40] respectively. Given the determined oxygen content of 0.19 wt% for the Ti powder from above, the expected oxygen content of the bulk Ti-xAl-yFe pre-compacted blend would be 0.22 wt% O, slightly higher than that measured for the Ti-xAl-yV blend. The oxygen content of this alloy blend after full processing ranges from 0.2628 to 0.3783% O which corresponds to a 19-72% increase. When comparing the green densities of the Ti-xAl-yFe and measured $O_2$, a clear correlation is observed wherein oxygen pick-up increases as green density decreases. This trend is more evident in the Ti-xAl-yFe alloy due to its higher %Ti which increases the susceptibility to oxygen pick-up compared to Ti-xAl-yV.

For both alloys, the uptake of oxygen does not appear to be dependent on whether the rolling path did or did not include the intermediate annealing step. It is likely that the primary occurrence of oxygen pick-up takes place during the post roll compaction, initial sintering step when the surface area is highest due to lower green densities and

the presence of open porosity. This observation is supported by the wrought Ti-6Al-4V sample which has notably lower oxygen, equal to its certification composition of 0.2 wt%. Despite being annealed at 1200°C in the Sentrotech furnace for an hour on two occasions, it exhibited no oxygen pick-up due to its fully dense condition.

Observations regarding oxygen pickup are concurrent with the findings during sintering CIP CP-Ti compacts by Cooke et. al [42] summarized in Section 2.5.2. Green densities of CIP samples were approximately 75-80%, which is greater than many of the roll compacted samples whose green densities ranged from 63-89%. With lower green density, there is more surface area available during sintering, resulting in increased oxygen pickup in the roll compacted material compared to similar powders in the previous study of CIP compacted materials.

## 8.3 Microstructure

### 8.3.1 Wrought

Etched micrographs of the wrought Ti-6Al-4V in the as-received condition with a mill annealed microstructure are shown at different magnifications in Figure 8-8 (a) and (b).

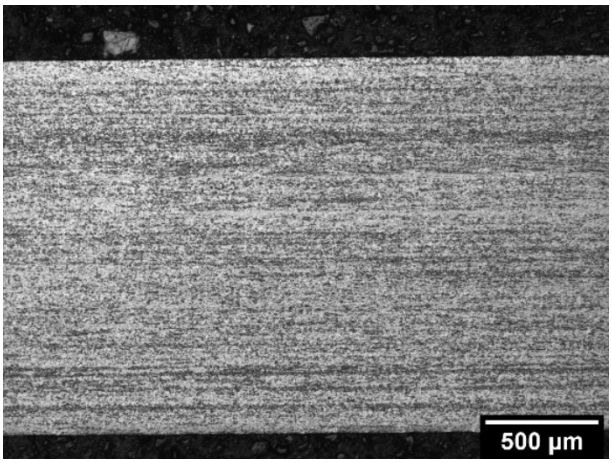


(a)

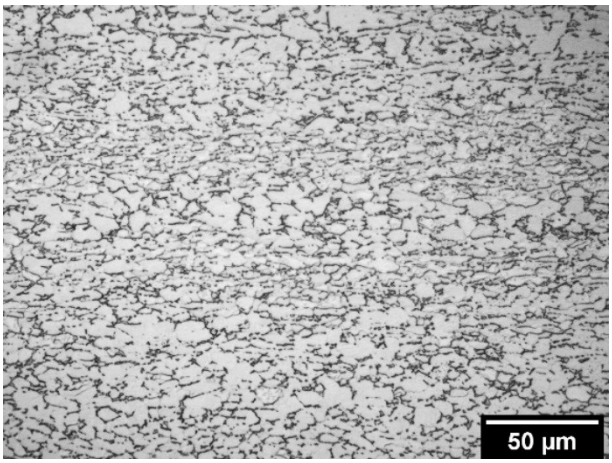


(b)

*Figure 8-8. Microstructure of high strength worught Ti-6Al-4V in the as-recieved condition from McMaster-Carr*

Initially, the wrought material begins with a large grain size. Significant rolling is required to produce the thin sheet and the deformation results in elongated grains in the rolling direction. If rolling is performed at elevated temperatures, recrystallization

and new grain formation occurs producing small and equiaxed grains [27]. The mill anneal designation is applied to an α-β titanium alloy that is hot worked, then annealed at 705°C for at least 30 min, up to several hours then air cooled and the resultant microstructure is an incompletely recrystalized α matrix with a small volume of small β particles [20].

Since mill annealing is not considered a full anneal, it can leave traces of cold or warm working [1], which is evidenced by the banding texture which remains in the as-received wrought material pictured in Figure 8-8(a). The mill annealed microstructure described above is observed, particularly in Figure 8-8(b), where the majority of the material appears as a light grey, which is the α-Ti matrix. Some small, distinct grains of β-Ti are observed as a bright white when etched with Kroll's reagent.

The as-received wrought material was annealed for one hour at 1200°C in the Sentrotech furnace to simulate the sintering heat treatment which the roll compaction samples undergo immediately after compaction. During heat treatment, the material undergoes the α-β transformation. The resultant microstructure in Figure 8-9 shows that the wrought Ti-6Al-4V alloy has undergone significant grain growth.

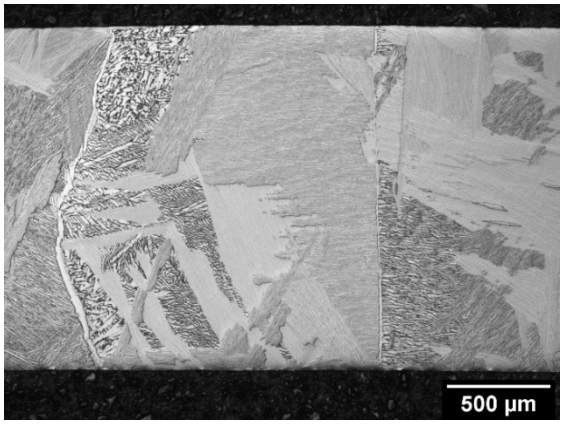


*Figure 8-9. Wrought Ti-6Al-4V after the simulated sintering treatment for 1 hour at 1200 ℃*

A furnace cool was performed, meaning that the heating elements were turned off and the furnace was allowed to return to room temperature, which produces a slow cooling rate. This method allows more time for diffusion of the alloying elements and yields microstructures more similar to equilibrium cooling, where α-Ti nucleates at the grain boundaries between retained β-Ti forming a coarse plate-like Widmanstätten microstructure.

The heat-treated wrought Ti-6Al-4V material was then rolled via Paths C and D. An example of the microstructure produced via Path C, including the final anneal, is presented in Figure 8-10.

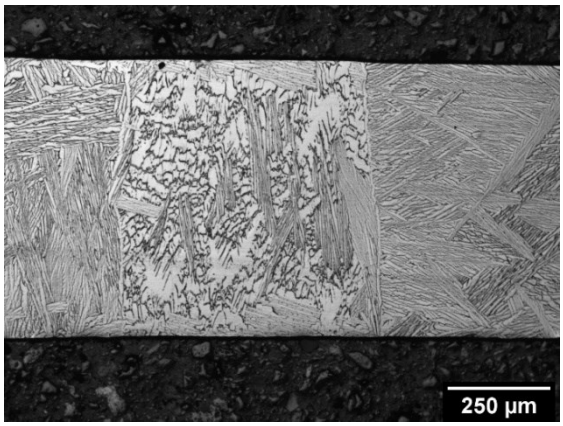


*Figure 8-10. Wrought Ti-6Al-4V after cold rolling Path C and final heat treatment*

Significant cold work was imparted during the rolling process which increases the internal energy of the material; wrought samples experienced reductions in thickness of 57-59%. During the recrystallization phase of annealing, new dislocation-free grains nucleate. Grains will continue to grow until no cold worked material remains. Since internal energy is a driving factor of nucleation, greater levels of cold work result in more nucleation sites and an overall finer grain size [56]. Despite the cold working induced during roll reduction, the microstructure of the final wrought sheet is similar to that of the as-sintered state. An estimate of the recrystallization temperature for an alloy is 0.4 to 0.5 $T_m$, where $T_m$ is the melting point of the alloy in Kelvin [57]. Given the melting point of Ti as 1941 K. the recrystallization temperature would be in the range of 776.5 to 970.5 K (503.5-697.5°C). Therefore, the sintering/annealing temperature of 1200°C used in the current study would be expected to recrystallize and cause significant grain growth, removing any influence of prior cold work on the final microstructure.

*8.3.1.1 Grain Size*

Grain size was not measured in the as-received condition as the mill-annealed microstructure cannot be directly compared to any of the other wrought or roll compaction conditions. However, Figure 8-8 is concurrent with a fine scale microstructure typical of a mill annealed heat treatment.

The grains of the sintered and Path C and D treatment are generally between half and full thickness of the sample. A micrograph of the complete cross section was obtained, and lines were superimposed at ¼, ½, and ¾ height. Intercepts with grain boundaries were counted to determine the average width of the grains in these

samples. In the as-sintered wrought sample, the average width of grains was 447 μm while the rolled samples after the final annealing heat treatment were smaller at 212 μm.

While both Figure 8-9 and Figure 8-10 have a Widmanstätten microstructure, the grain size estimation indicates that grains are much smaller in the final condition compared to the as sintered condition. This is likely due to the different starting conditions for both treatments. The as-received material was in the mill-annealed condition which would have less internal stress compared to the cold worked material resulting in a lower driving force for nucleation of new grains and a coarser grain size.

The majority of the deformation, and therefore cold work, occurs during the first and final rolling steps rather than the repeat rolling step since the intermediate anneal was not performed. Without the inclusion of an intermediate annealing step in either Path C or D, the grain size and overall microstructures are projected to be equivalent for these two paths and represented by the image of Figure 8-10, since all wrought Ti-6Al-4V samples experience similar levels of cold work.

### 8.3.2 Roll Compacted Alloys

#### *8.3.2.1 Grain Size*

The grain size of one sample of both roll compacted alloys after completing the final annealing step in each of the rolling paths A, B, C, and D was measured using the circular grain intercept method [50]. The values from multiple micrographs taken at various locations across the sample are averaged and presented in Table 8-9.

*Table 8-9. Grain size measurements of roll compacted samples in μm*

| Ti-xAl-yV | | Ti-xAl-yFe | |
|---|---|---|---|
| **A1** | 63.43 | **A2** | 44.91 |
| **B1** | 58.68 | **B2** | 35.28 |
| **C2** | 39.29 | **C2** | 29.58 |
| **D3** | 39.71 | **D3** | 27.55 |

The observed grain size is consistently larger in Ti-xAl-yV than the corresponding rolling path of Ti-xAl-yFe. Paths A and B which include the intermediate annealing step show larger grains than those samples rolled via Paths C and D. This is likely due to longer total times at high temperatures (i.e. 3 hours versus 2 hours) allowing for more significant grain growth. In addition, the samples without an intermediate anneal have more total cold work and thickness reduction built up prior to the final annealing step. In Path B, there is a repeat rolling step with two additional passes of 0.05 mm, following the intermediate annealing step where the additional cold work results in smaller grain sizes compared to Path A of the same alloy. In Paths C and D where there is no intermediate annealing step, the repeat rolling step shows less of an impact on the grain size.

It is interesting to note that the grain size of the powder metallurgy-based alloys is significantly lower than that of the wrought material processed in the same way. This will be discussed in more detail later in the thesis.

#### *8.3.2.2 Micrographs*

Samples were polished to a mirror finish using colloidal silica and etched with Kroll's Reagent for 8-10 seconds. Figure 8-11 and Figure 8-12 show the examples of the

microstructures in Ti-xAl-yV and Ti-xAl-yFe respectively. Images were chosen from Paths A and D where the largest and smallest grain sizes were measured.

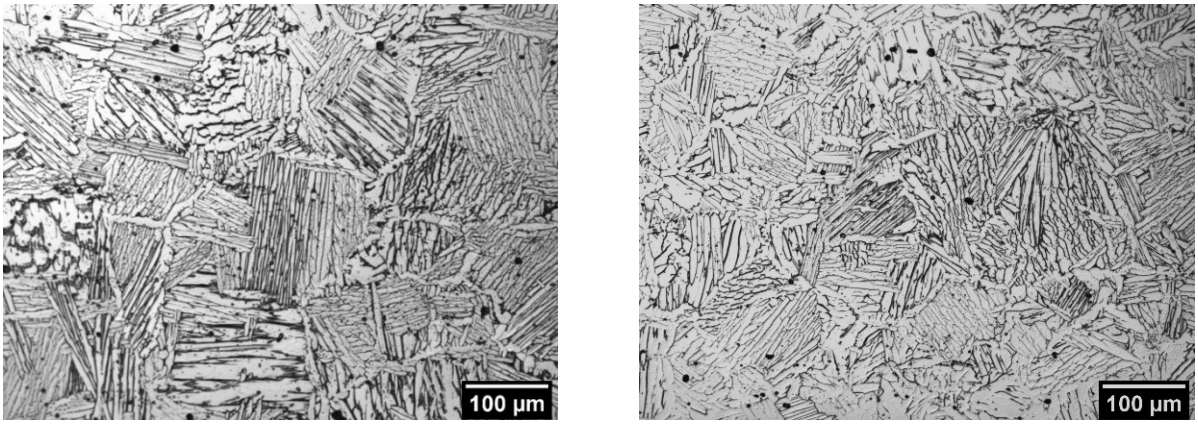


(a) (b)

*Figure 8-11. Micrograph of Ti-xAl-yV (a) A1 and (b) D3 after final annealing heat treatment*

Similar to observations in Set 1, the Ti-xAl-yV material has grains of Widmanstätten microstructure. The plate width is generally fine throughout the material although it is not entirely homogeneous and there are some grains where the plate width is slightly larger.

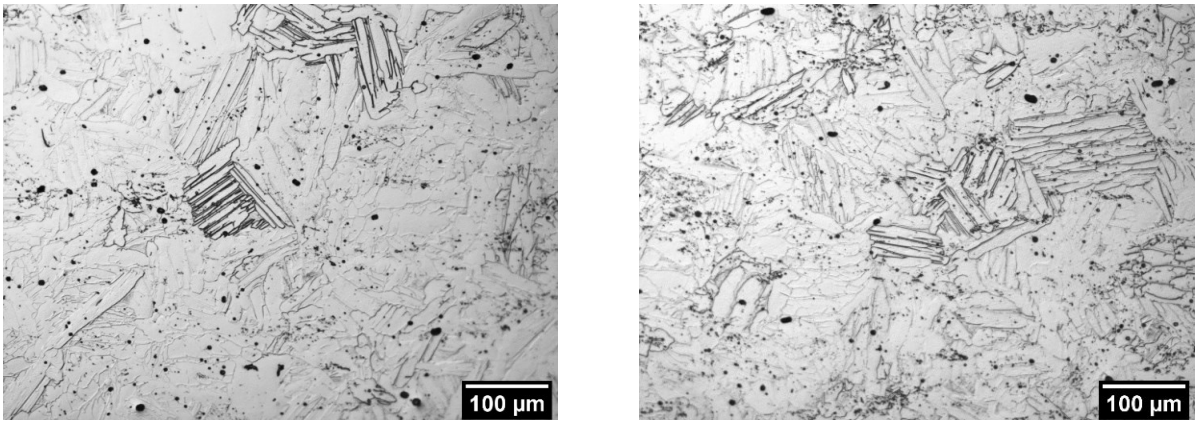


(a) (b)

*Figure 8-12. Micrograph of Ti-xAl-yFe (a) A2 and (b) D2 after final annealing heat treatment*

There are also some grains in Ti-xAl-yFe where the Widmanstätten plates can be clearly observed, although distance between plates is wider than in Ti-xAl-yV. Other grains are more equiaxed with little or no texture. As discussed in 8.2.2, the alloy content in the Ti-xAl-yFe material was often lower than the target composition. In areas where the Widmanstätten microstructure is observed, the grain boundaries tend to have better contrast than the grain boundaries of the equiaxed region. Increasing the etching time was not effective in improving contrast for in the Ti-xAl-yFe material; rather than accentuating grain boundaries, the whole surface became darker, giving a burnt appearance.

There is a small amount of porosity observed in both alloys. During the final annealing step, the flattened, elongated pores become more rounded and closed off. All sintering and annealing is performed under a flowing argon atmosphere which can lead to gas becoming trapped within the microstructure and residual porosity in the material [2].

## 8.4 Mechanical Properties

### 8.4.1 Wrought Ti-6Al-4V Tensile Results

The stress strain curves in Figure 8-13 show data for the sub-sized dog bone samples produced from the wrought Ti-6Al-4V. Mechanical properties derived from these tensile tests for processed samples are compared to those provided for the as-received material from the manufacturer in Table 8-10.

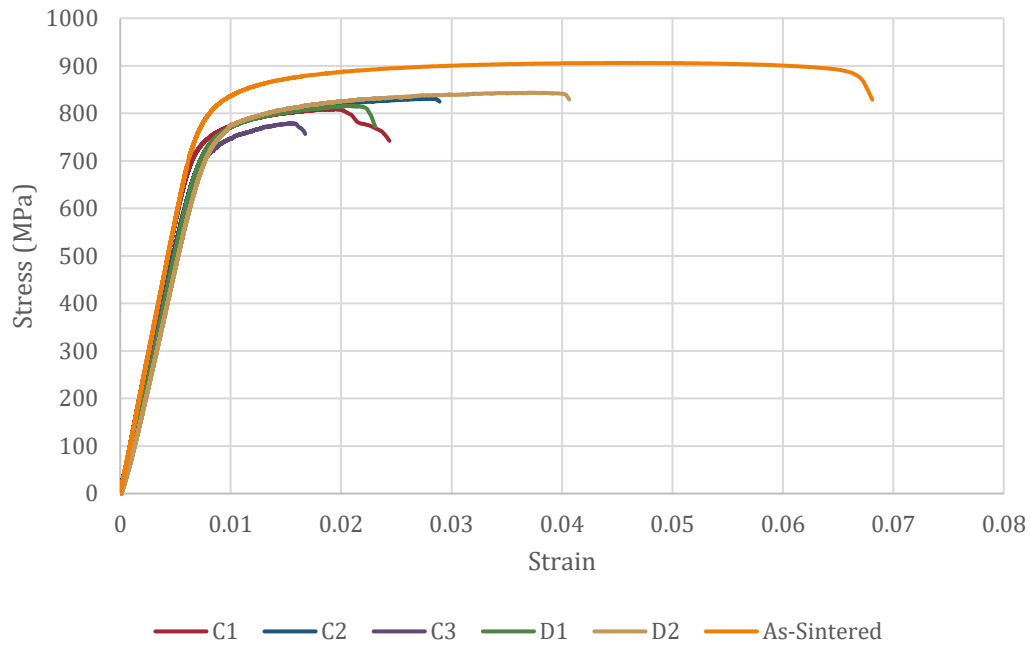


*Figure 8-13. Stress-strain curve of wrought Ti-6Al-4V samples in rolled and as-sintered conditions*

*Table 8-10. Comparison of wrought Ti-6Al-4V mechanical properties from a variety of processing conditions*

| | YS (MPa) | UTS (MPa) | %El | Reference |
|---|---|---|---|---|
| **As-received** | 1006 | 1062 | 13 | [55] |
| **As-sintered** | 822 | 906 | 6.8 | - |
| **Path C** | 752 | 806 | 2.3 | - |
| **Path D** | 760 | 791 | 2.47 | - |

The as-received material has both increased strength and ductility compared to the properties measured for the sheet after performing the processed condition of this study. This can be attributed to the finer grain size and finer scaled microstructure in the mill annealed condition. The significant grain growth and coarse Widmanstätten structure produced by both the simulated sintering step and to a lesser degree, final annealing after cold working (i.e. as-sintered and Paths C and D) lowers the strength of the alloy as would be expected. It also has a significant negative impact on ductility compared to the mill annealed microstructure.

### 8.4.2 Roll Compacted Tensile Results

The following, Figure 8-14 through Figure 8-17, show stress-strain curves for the roll compacted samples under differing rolling Paths A, B, C, and D. Results for samples which broke outside of the reduced section are excluded from the schematics in this chapter. Some of the outliers can clearly be attributed to machining defects where the blanks were exceptionally curved or small resulting in machining difficulties. At least one valid sample remains for each material and rolling condition.

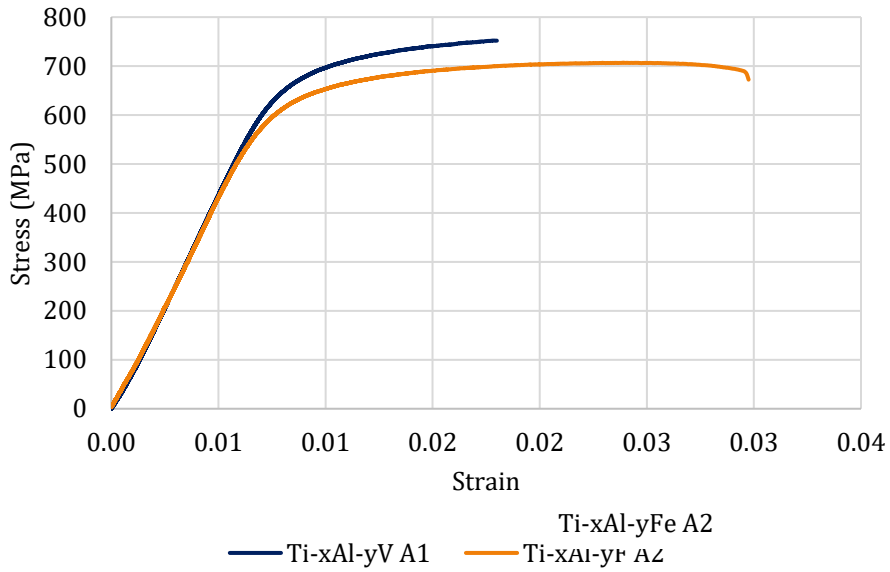


*Figure 8-14. Stress-strain curves for roll compacted samples processed via Path A*

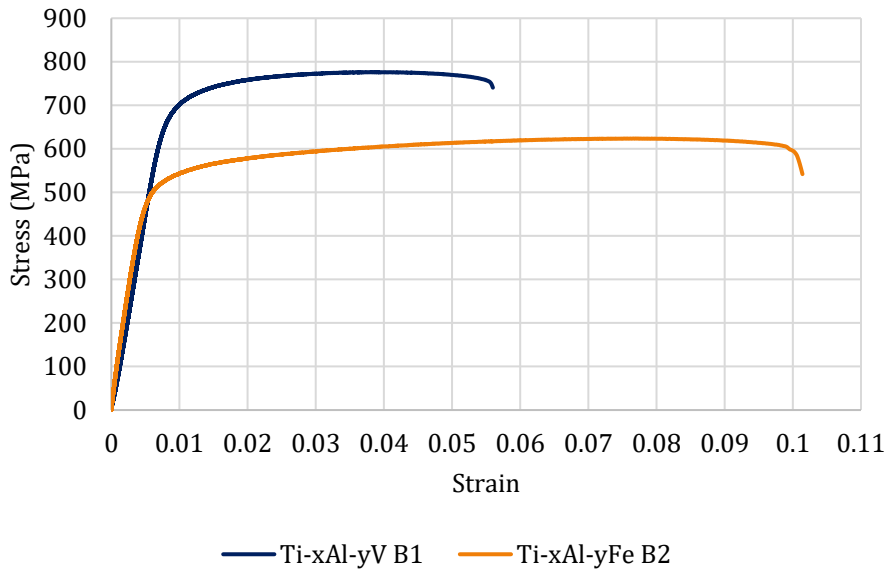


*Figure 8-15. Stress-strain curves for roll compacted samples processed via Path B*

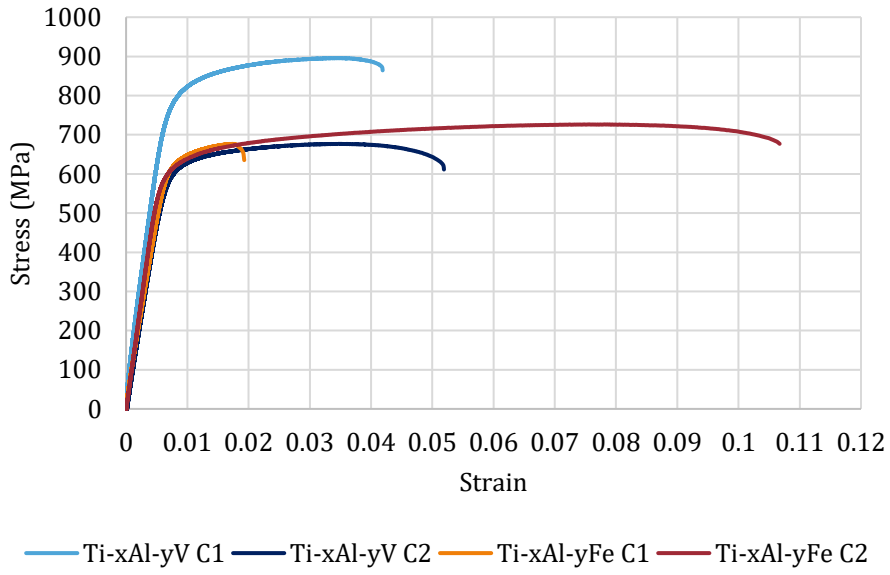


*Figure 8-16. Stress-strain curves for roll compacted samples processed via Path C*

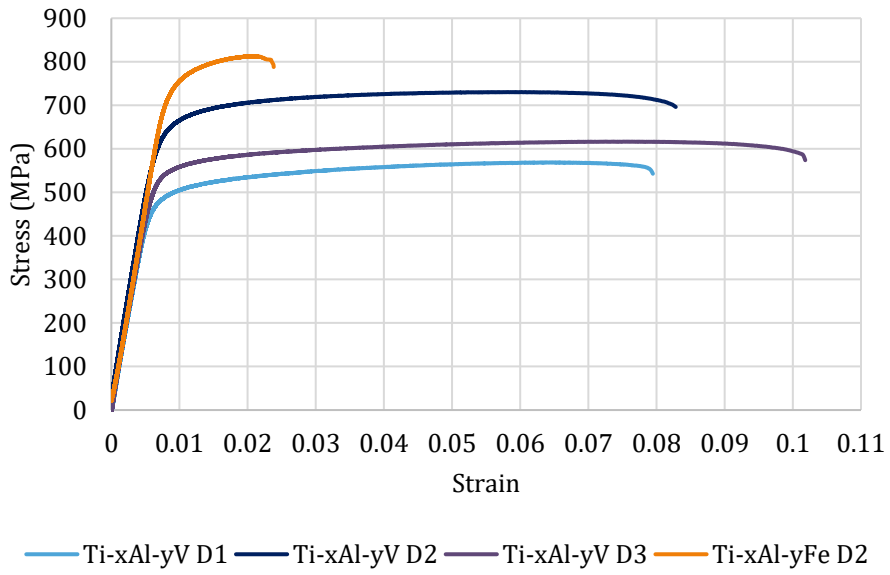


*Figure 8-17. Stress-strain curves for roll compacted samples processed via Path D*

Apart from rolling path D, the Ti-xAl-yFe shows greater ductility but lower tensile strength than Ti-xAl-yV.

## 8.5 Summary of Composition and Mechanical Properties

A summary of values obtained for compositions and mechanical properties are given in Table 8-11 that were presented in Sections 8.1 through 8.4. A legend for symbols used within the table is given below. The table highlights that there is wide variation in the mechanical properties from one sample to another. This is due to a number of changing variables, including alloy composition, $O_2$ ppm, grain size and processing path. The discussion section below will examine relationships and trends in more detail.

*Table 8-11. Summary of chemical compositions, oxygen content, mechanical properties, and grain sizes*

| Alloy | Sample | Ti % | Al % | V or Fe % | O ppm | Max Strain % | Offset Yield MPa | Max Stress MPa | Final Hardness HV | Grain Size µm |
|---|---|---|---|---|---|---|---|---|---|---|
| **Wrought** | C2 | 89.81 | 6.32 | 3.87 | 1902.16 | 2.89 | 761.68 | 831.00 | 340.79 | - |
| **Ti-xAl-yV** | A1 | 91.44 | 5.14 | 3.42 | 2715.63 | 1.80 | 688.13 | 752.04 | 390.70 | 63.43 |
| | A2** | - | - | - | - | 2.22 | 727.33 | 786.40 | - | - |
| | B1 | 89.47 | 6.27 | 4.26 | 2818.53 | 5.60 | 693.31 | 776.70 | - | 58.68 |
| | B2* | - | - | - | - | 0.54 | * | 428.22 | - | - |
| | C1 | 92.69 | 4.35 | 2.96 | 2534.41 | 4.19 | 804.64 | 895.88 | - | 38.59 |
| | C2 | 94.16 | 3.52 | 2.32 | - | 5.19 | 610.85 | 676.73 | 252.64 | 40.00 |
| | D1 | 95.45 | 2.71 | 1.84 | 3078.01 | 7.95 | 489.33 | 569.51 | - | - |
| | D2 | 95.39 | 2.89 | 1.72 | - | 8.28 | 654.45 | 730.84 | - | - |
| | D3 | 92.49 | 4.47 | 3.03 | - | 10.18 | 544.86 | 616.87 | | 39.71 |
| **Ti-xAl-yFe** | A1* | - | - | - | - | 0.19 | * | 114.09 | - | - |
| | A2 | 94.66 | 2.39 | 2.95 | 3121.06 | 2.98 | 642.09 | 706.95 | 296.09 | 44.91 |
| | B1* | - | - | - | - | 0.19 | * | 447.13 | - | - |
| | B2 | 97.39 | 1.13 | 1.48 | 2628.56 | 10.14 | 520.22 | 623.98 | - | 35.28 |
| | C1 | 95.33 | 2.77 | 1.90 | 3783.28 | 1.93 | 636.63 | 676.70 | - | - |
| | C2 | 97.49 | 1.06 | 1.45 | - | 10.67 | 613.11 | 726.46 | 326.40 | 29.58 |
| | D2 | 96.85 | 1.69 | 1.46 | 2978.26 | 2.38 | 758.92 | 813.21 | - | 27.55 |

* Broke before the plastic region during tensile testing

** Broke outside of the strain gauge during tensile testing

- No measurement obtained

## 8.6 Discussion

### 8.6.1 Mechanical Properties

Figure 8-18 compares the UTS and elongations for all roll compacted samples with measured tensile results. For ease of comparison, the two dashed lines plotted are the average UTS (horizontal lines) and % elongation (vertical line) for the wrought Ti-6Al-4V tensile samples produced using rolling Paths C and D.

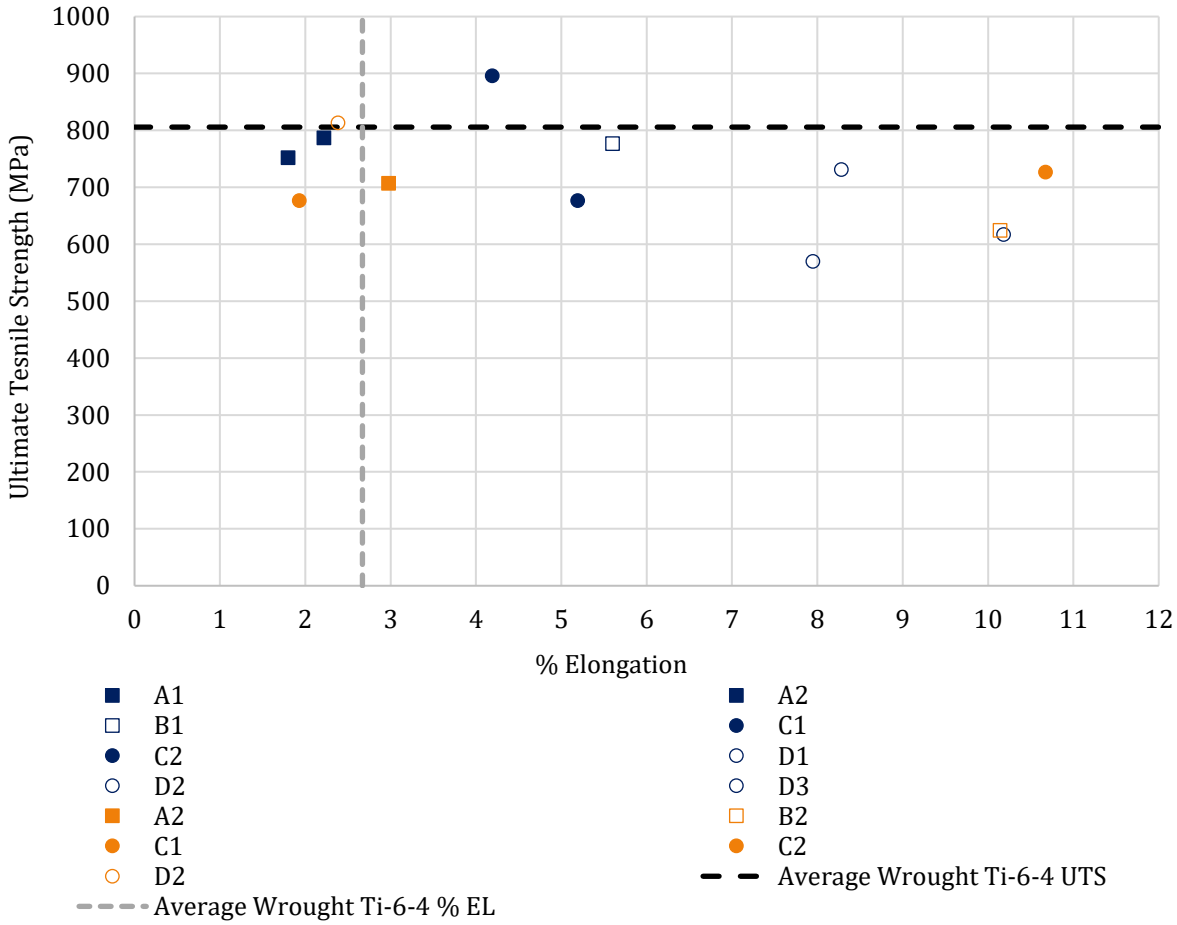


*Figure 8-18. UTS vs. % elongation for roll compacted samples with averages of tensile properties for wrought Ti-6Al-4V*

There is a general expectation that as strength increases, ductility will decrease. Although the data is not highly clustered, it does follow this general trend. In many samples, the UTS of the roll compacted samples are comparable to the wrought

Ti-6Al-4V material which was rolled under the same or similar conditions. All of the RC samples have elongations which are either comparable to those of the wrought samples, and in some samples much larger.

### 8.6.2 Composition and Grain Size

Figure 8-19 shows the plot of oxygen content compared to %Ti determined via LA-ICPMS in each of the samples. There appears to be a slight trend indicating greater levels of oxygen in samples where percentage of titanium composition is higher. This would make sense since Ti would be the most susceptible element to oxygen pick-up in either alloy.

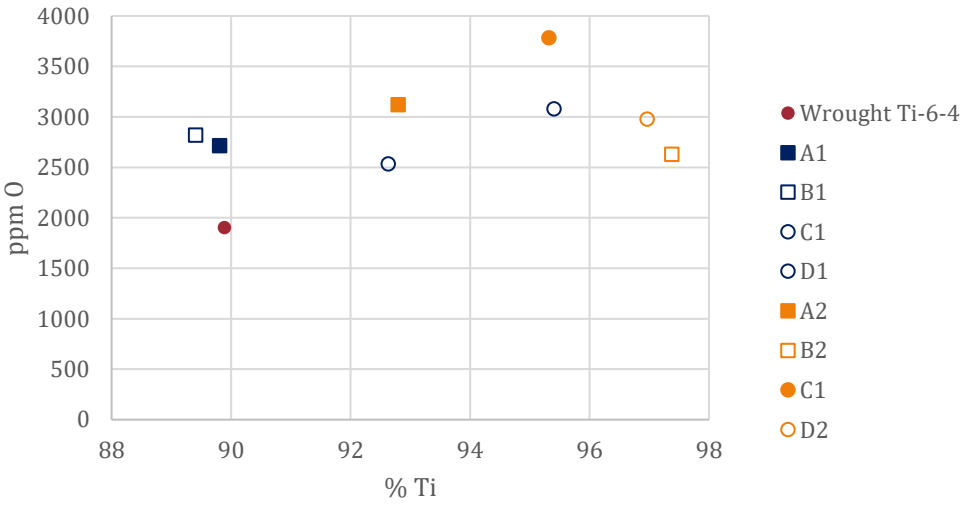


*Figure 8-19. ppm oxygen compared to %Ti from ICP*

Relationships of grain size and the amount of alloy content were examined to observe any correlations in Figure 8-20. Here, %Ti was determined from LA-ICPMS analysis for one sample from each alloy and rolling path, apart from Ti-xAl-yV C, where there is data for both C1 and C2 samples. For Ti-xAl-yV A and C2, and Ti-xAl-yFe A and C the ICP analysis is an average of three measurements. There does appear to be a broad

trend where greater alloy content yields larger grain sizes. The Ti-xAl-yFe samples have a smaller grain size than the Ti-xAl-yV, but this may be due to their generally lower alloy content rather than an effect intrinsic to iron or vanadium.

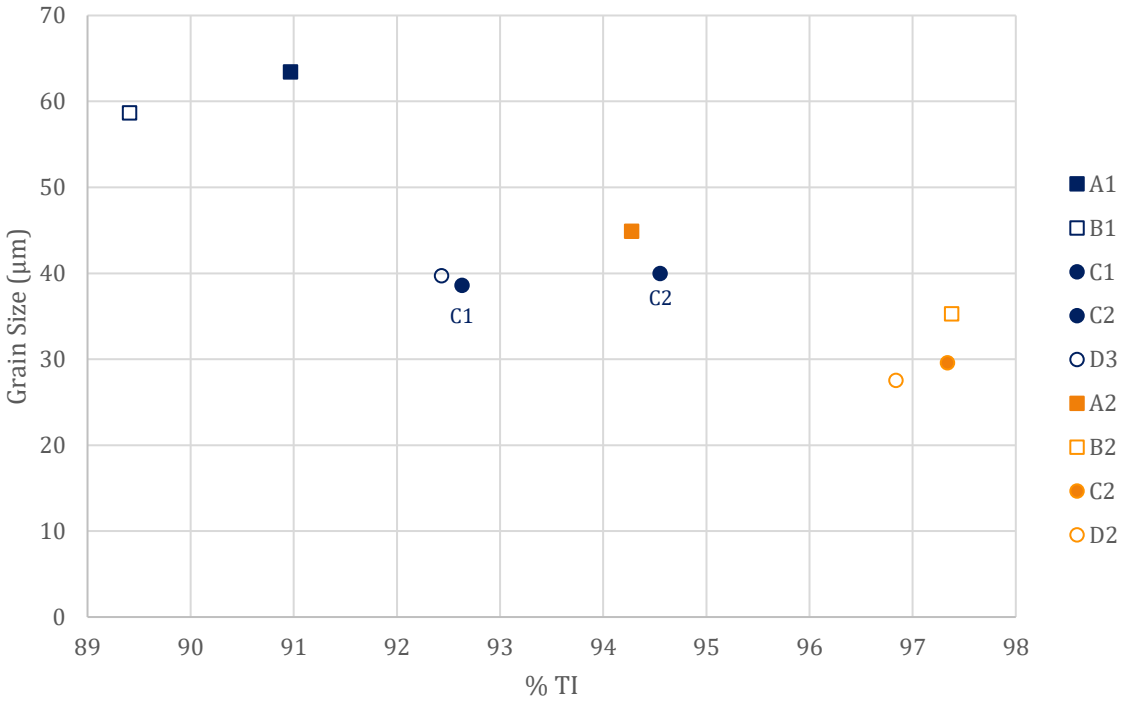


*Figure 8-20. Comparison of % Ti vs grain size*

Figure 8-21 plots the relationship between oxygen content and grain sizes for six samples where both measurements were obtained from the same strip. There does appear to be two distinct clusters with a distinct linear negative correlation; with increasing the oxygen content, there is a decrease in observed grain size.

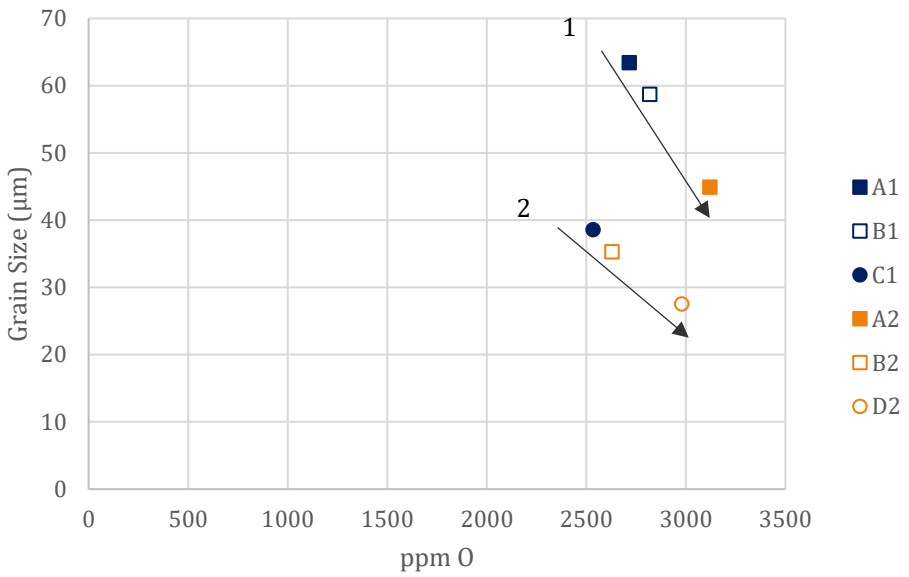


*Figure 8-21. Comparison of grain size and oxygen content*

The Ti-xAl-yV samples A1 and B1 in the first cluster have %Ti of 91.44 and 89.47% respectively. As part of the second cluster, the C1 sample has a greater titanium composition at 92.69%. The Ti-xAl-yFe A2 in the first cluster has a titanium composition of 94.66%. In the second cluster, Ti-xAl-yFe B2 and D2 have titanium compositions of 97.39 and 96.85% which are much higher than that of A1 which falls within the first cluster. In addition to oxygen alone, it seems that the amount of alloying additions also impacts grain size, where greater amounts of alloy additions inhibit grain growth. With limited data points of each alloy in each cluster, it is not possible at this time to determine whether the effect is strictly a function of the %Ti, or a more complex relationship between ratios of titanium, α, and/or β stabilizing additions.

Oxygen is an α stabilizing element; if it were to be present in the matrix as an interstitial element, it is expected that it would segregate to the α-Ti grains rather than β-Ti grain boundaries. This segregation effect of β and α stabilizers was evidenced by aluminium in the EDS mapping analysis shown in Figure 7-5 and Figure 7-7. However,

if oxygen were present in the form of an oxide, it would most likely be present from the as-received powder condition or formed at the particle surface in the initial sintering step which was determined to be the processing step most responsible for oxygen pick-up in RC material. During the initial sintering step, significant densification has not yet occurred, and many particle surfaces are exposed to the atmosphere yielding a much larger surface area compared to a wrought strip with the same dimensions. An oxide particle from either of these conditions is thermodynamically stable and will persist through subsequent processing steps. Even once near full density is achieved, oxide particles would remain at prior particle boundaries and act as pins to prevent movement of grain boundaries during intermediate and final heat treatments.

Conversely, the wrought material was fully dense upon initial sintering and had negligible oxygen pick-up during heat treatments. The oxygen in the wrought material is more likely to be distributed throughout the alpha matrix. With fewer oxide particles to effectively pin grain boundaries, the wrought material was much more susceptible to grain growth at higher temperatures compared to the RC material.

### 8.6.3 Composition and Mechanical Properties

A plot of ultimate tensile stress as a function of oxygen content is presented in Figure 8-22. Oxygen is highly effective in strengthening titanium as an interstitial element [15] so it is expected that as oxygen increases, the maximum stress will also increase. When the data is compared below, however, there is an unexpected and clear negative correlation between UTS and oxygen content.

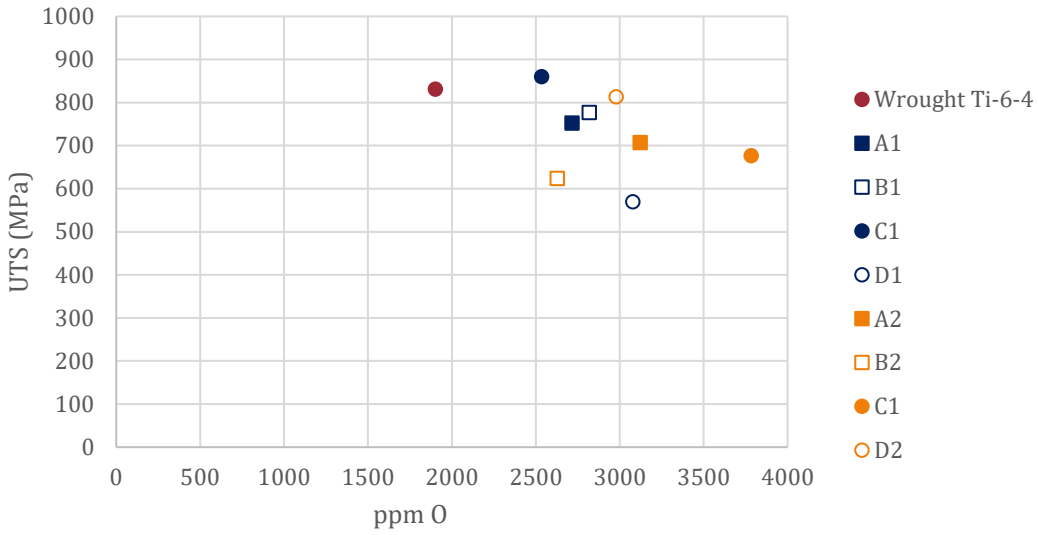


*Figure 8-22. Comparison of maximum stress and oxygen content*

Figure 8-23 shows the comparison of maximum strain compared to oxygen content for the same samples, where it is expected that increased oxygen would have a negative impact on ductility.

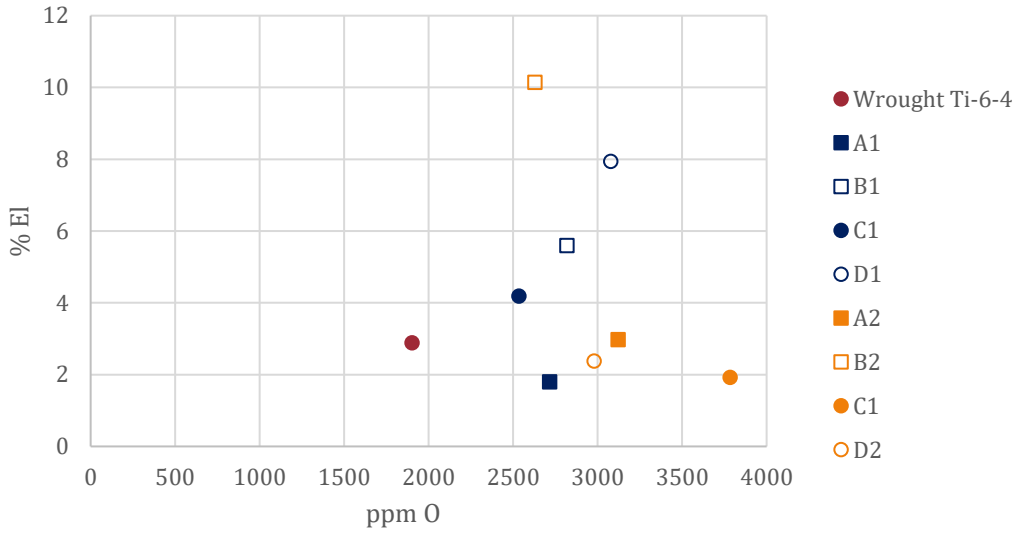


*Figure 8-23. Comparson of maximum strain and oxygen content*

There is not a clear trend in the Ti-xAl-yV alloy, although it is possible that the A1 data point is an outlier, giving a positive correlation among the other three sample

conditions. This is counter to the expectation that increased oxygen reduces ductility, but is an inverse correlation compared to the relationship between UTS and oxygen content. The elongation of Ti-xAl-yFe decreases as oxygen increases, which is in agreement with what is expected based on literature regarding ductility and oxygen.

Figure 8-24 plots the 0.2% offset yield in MPa compared to the %Ti measured using LA-ICPMS. Results were normalized to Ti, Al, and V or Fe dependent on the alloy. Data markers are labeled where more than one sample is plotted for the same preparation condition.

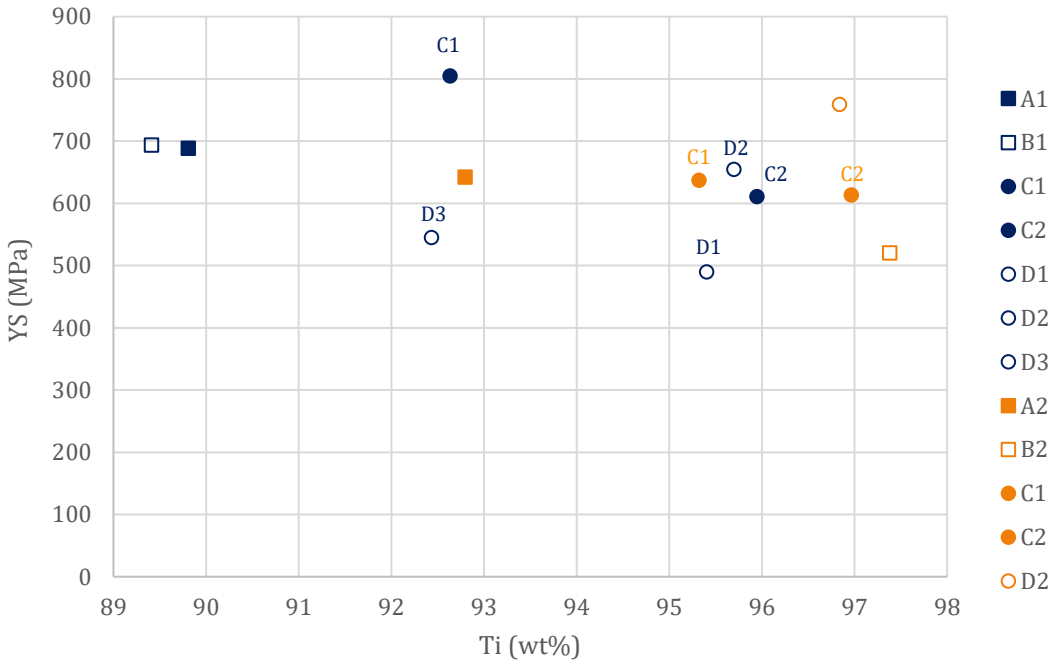


*Figure 8-24. Comparison of %Ti and yield strength*

The plot indicates that yield strength is not highly sensitive to %Ti, although a slight trend of increasing strength with increasing alloy content is suggested here.

In titanium alloys, aluminium is an α stabilizing element and segregates to the α-Ti grains, which strengthens via the solid solution strengthening mechanism. Vanadium

and iron promote the stabilization of the β-Ti phase, which strengthens material as a secondary phase. Therefore, as alloy content is increased, the strength of the alloy is expected to increase relative to the pure material. With increased levels of alloying additions though, the relative titanium content decreases, which correlates to a decrease in oxygen as was shown in Figure 8-20. Contradictory effects increasing titanium content and increasing alloy additions with respect to strength and ductility result in correlations are that are unclear or occasionally observed to be contrary to what is expected. As previously indicated, the oxygen content and grain size of the RC materials are also a function of alloy content. Since both these factors can further influence strength, interpretation of strength based on only one of these factors (i.e. composition) is made difficult.

### 8.6.4 Grain Size and Mechanical Properties

Figure 8-25 plots the grain size against yield strength. The average grain size of the samples rolled using Path A are approximately 50% larger than the same alloy rolled using Path C due to the intermediate annealing step.

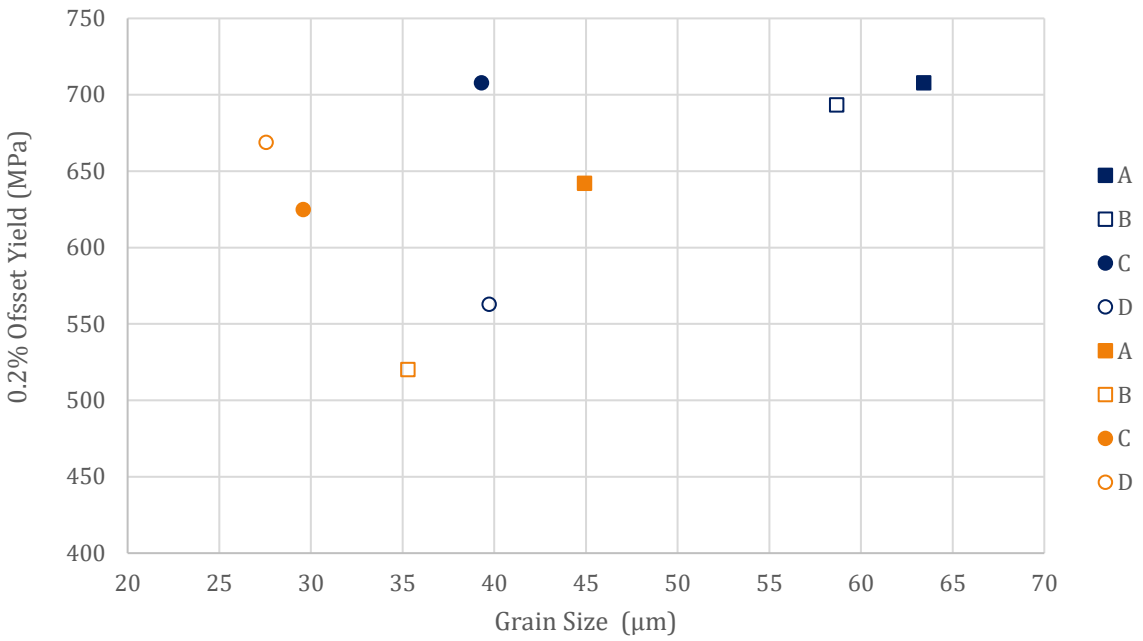


*Figure 8-25. Comparison of grain size and yield strength in roll compacted alloys*

The Hall-Petch relationship suggest that yield strength should increase as grain size decreases. Measured YS in Path C is equal to path A in Ti-xAl-yV and lower in Ti-xAl-yFe compared to Path A. This is contradictory to the Hall-Petch prediction. This would indicate that the grain size is not the principal factor influencing yield strength. If any general statements are made regarding the grain sizes are consistently larger when the additional intermediate anneal was performed, which is appropriate as these materials experience greater times at higher temperatures where grain growth can occur. As previously stated, several other variables are changing in the alloy series which can influence yield strength. This makes interpretation of the influence of only one variable on strength, in this case grain size, difficult.

# Chapter 9: Rolling Mechanics

## 9.1 Pressure and Density

### 9.1.1 Roll Compacted – Set 1

Flow stress was calculated and is plotted against observed density and is presented in Figure 9-1, where sintered density is again plotted as 0MPa.

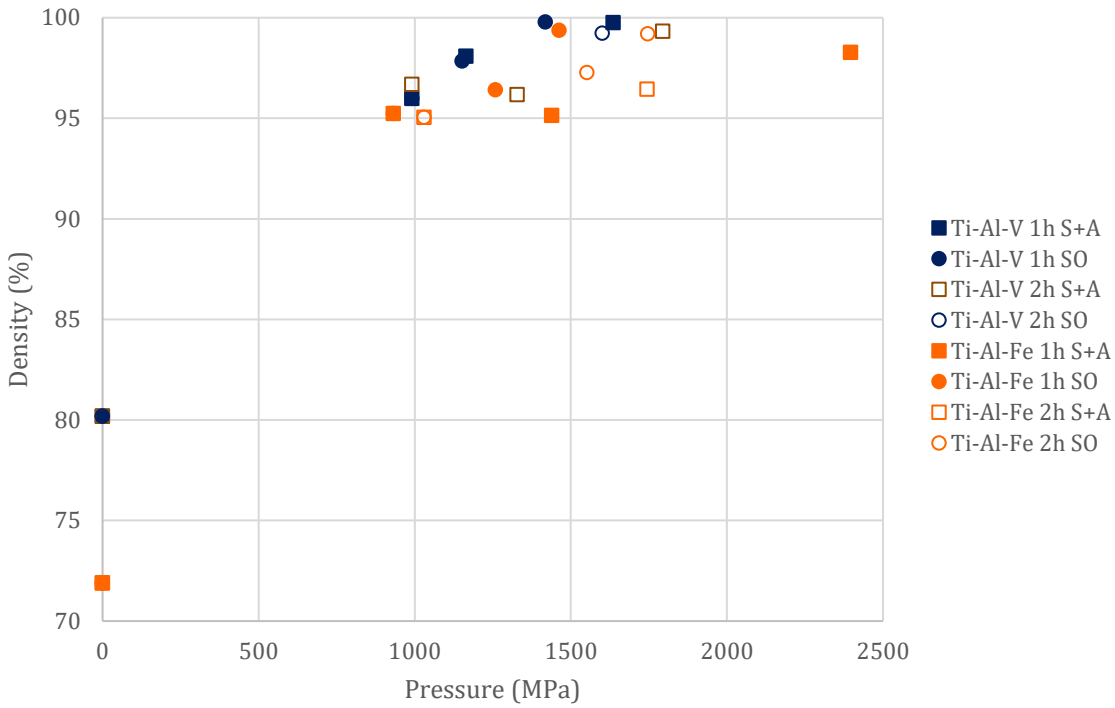


*Figure 9-1. Pressure vs. density graph for Sample Set 1*

Without the intermediate annealing step, all SO samples experience densification during all three rolling steps. For S+A samples, there is less or no densification occurring during the second rolling step.

### 9.1.2 Roll Compaction – Set 2

The comparison of roll pressure and density are divided into two plots for ease of viewing. Figure 9-2 contains data from rolling Paths C and D and Figure 9-3 contains data from Paths A and B. Density was measured optically using metallographic image

analysis of unetched polished sections and force applied was measured by load cells attached to both the top and bottom rolls of the rolling mill. The full evolution for density of roll compacted samples after each processing step is available in Appendix C. Roll force measurements were then used along with dimensions of the strip to calculate the roll pressure at each step using Equations 3-5 from Section 2.4. The sintered density prior to cold rolling is plotted as 0 MPa roll pressure.

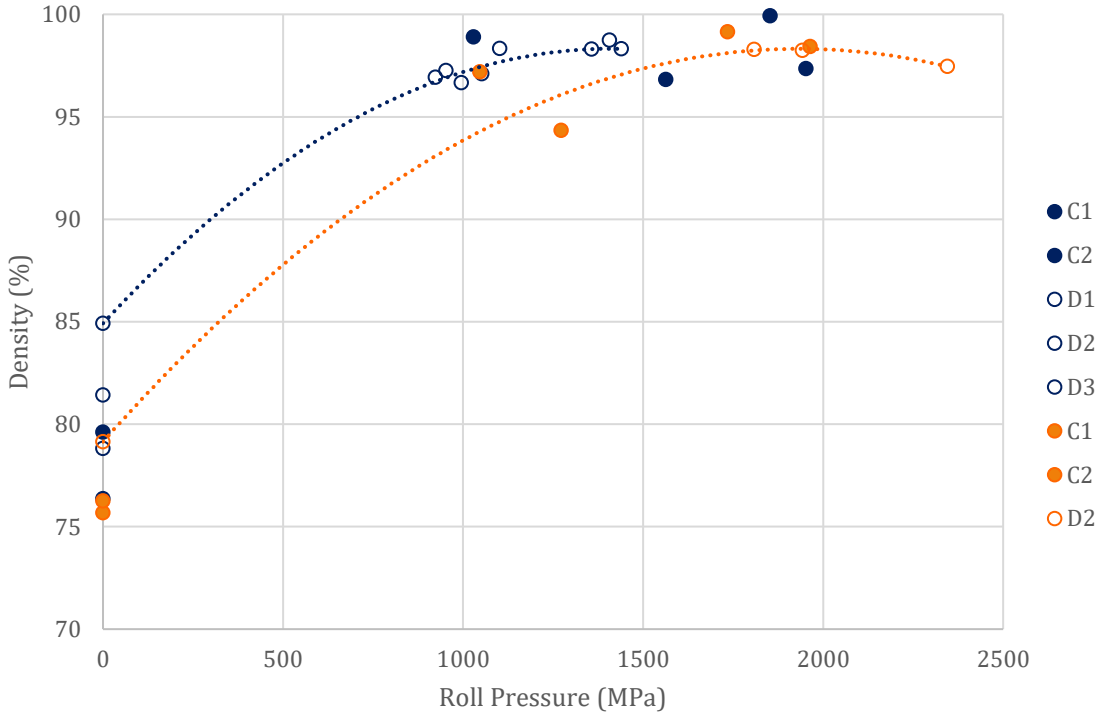


*Figure 9-2. Roll Pressure vs. density for samples rolled without intermediate anneal (Paths C and D)*

Even after the first rolling step with a roll gap of 0.05 mm, the density has increased significantly to greater than 90%. By the final rolling step, density is 99% or higher in Ti-xAl-yV and 98% or higher in Ti-xAl-yFe. Generally, Ti-xAl-yV achieves higher peak densities using lower roll pressures compared to Ti-xAl-yFe, and Ti-xAl-yFe experiences greater roll pressure.

The same trends regarding roll pressure and densification with respect to alloy composition are observed in roll paths A and B as in roll paths C and D.

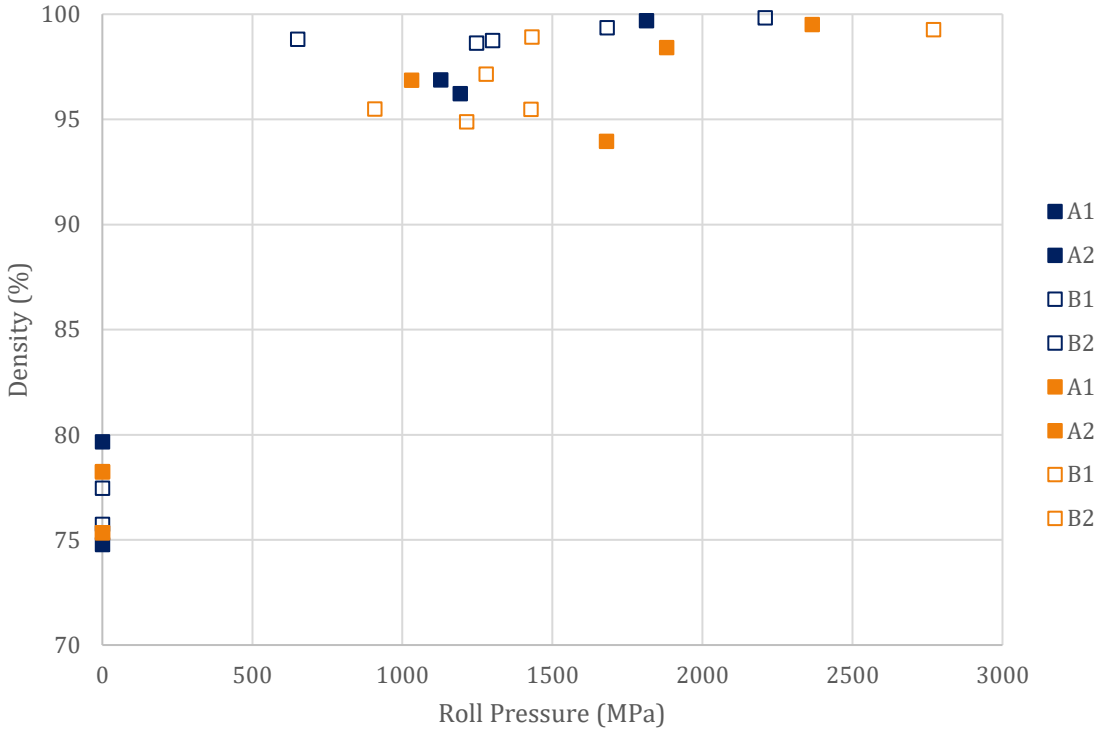


*Figure 9-3. Roll Pressure vs. density for samples rolled with intermediate anneal (Paths A and B)*

In each of the plots Figure 9-2 and Figure 9-3, a direct comparison of samples with and without the intermediate annealing step, with all other roll steps being equal is possible. There is no clear relationship between densification or roll pressure and whether or not the intermediate annealing step was performed for either subset of data.

There is one outlier in data; the final rolling step of the Ti-xAl-yV B2 sample which has a flow stress of 5120 MPa and so is not included in Figure 9-3. This is notably higher than any pressures observed in either RC alloy. The applied forces and gap widths were comparable to other samples; the high flow stress is attributed to the small contact length for this sample. The calculated contact lengths in other Ti-xAl-yV samples during

the two rolling passes of the final roll step range from 1.60-2.99 but is only 0.64 mm during the final pass of Ti-xAl-yV B2. The average thickness was measured as 0.64 mm after the first pass of the final roll step and only 0.63 mm after the repeat roll step, whereas other samples experienced a larger reduction, resulting in a larger contact length and a greater area of the sample undergoing the applied force from the rolls. Tensile testing was performed on the B2 strip; however, measurements were not obtained as the strip broke before the plastic region. Strain imparted during rolling was comparable to the other Ti-xAl-yV samples. As tensile measurements could not be obtained, this sample was not selected for LA-ICPMS analysis.

### 9.1.3 Comparison of Density as a Function of Methods

The relationship between density and applied pressure of roll compaction, cold rolling, and uniaxial press and sintering is combined and is presented below in Figure 9-4. Optical density was used for the press and sinter components and Archimedes density was used for the cold rolled strips. The value for tap density is used as the initial press and sinter data point at 0 MPa. In the case of uniaxial die compaction, pressure ($P$) was calculated knowing the cross-sectional area ($A$) of the die and the applied load ($F$) of the carver press.

The roll compaction step has a known applied force of 30 kN which is used in the calculation of the pressure or flow stress ($\bar{Y}$), given below. The diameter of the rolls is 200mm, and the grip angle, Θ was estimated as 7-8° by Dube [28], 7.5° was used for calculations. Draft and contact length are equal for both alloys, width measurements were averaged for Ti-xAl-yV and Ti-xAl-yFe strips. Individual compaction pressures for the die press and sintered samples were determined using equations (3)-(7) for Ti-xAl-

yV and Ti-xAl-yFe respectively. *F* is the uniaxially applied force and *A* is the area cross section of the die. In the case of roll compaction, the compaction pressure was calculated as shown here:

$$\Delta t = 2R(1 - \cos\Phi) = 2 * 100mm\ (1 - \cos(7.5)) = 1.71mm \tag{10}$$

$$L = \sqrt{R\Delta t}\ = \sqrt{100mm * 1.71mm} = 13.08mm \tag{11}$$
$$mm$$

$$\bar{Y} = \frac{F}{LW} = \frac{30000N}{1.15 * 18.08mm * 13.08mm} = 110.31\ MPa \tag{12}$$

$$\bar{Y} = \frac{F}{LW} = \frac{30000N}{1.15 * 18.52mm * 13.08mm} = 107.68\ MPa \tag{13}$$

Where *F* was the roll force used or measured, *L* is the contact length between the rolls and sheet, *W* is the sheet width, *Δt* is the sheet thickness reduction during each step and *R* was the radius of the rolls. The factor of 1.15 accounts for the plane strain conditions of the rolling process. A similar calculation was applied to cold rolling specimens accept that (3) was not necessary since *Δt* could be directly measured.

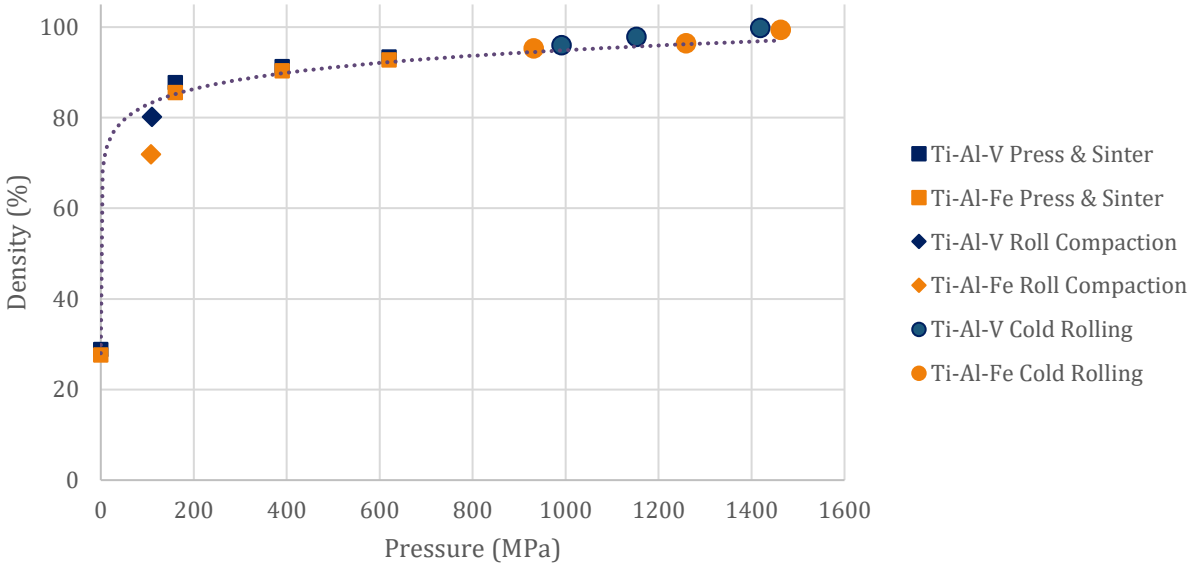


*Figure 9-4. Density and applied pressure for press and sinter and roll compacted parts of Ti-xAl-yV and Ti-xAl-yFe*

The force that can be applied using the uniaxial die and punch press method is limited, which also limits the green density that can be achieved in these alloys. Cold rolling of the roll compacted strips allows for the density to be measured as a function of higher applied forces. There is notable agreement between the three sets of data, apart from the roll compaction data point estimated for Ti-xAl-yFe, which is slightly lower than expected. The roll compaction data does involve some estimation, which is likely the cause of the deviation.

## 9.2 Wrought

Flow stress can be calculated using the work hardening (6), where $K$ is the strength coefficient and $n$ is the strain hardening coefficient.

$$\overline{Y} = K\varepsilon^n \tag{6}$$

Values for $K$ and $n$ in Ti-6Al-4V determined to be 1300 and 0.038 respectively and were obtained from *Strain hardening exponent and strength coefficients for aeroengine isotropic metallic materials* [58]. The as-received condition was not specified, although it was likely mill-annealed. Additionally, experimental data from the tensile testing of the as-sintered wrought Ti-6Al-4V was also used to calculate a $K$ of 1188.8 MPa and an $n$ of 0.0589. See Appendix D for the full analysis. The as-sintered tensile sample has a known microstructure, which is a large grained, Widmanstätten microstructure with coarse plate morphology, pictured in Figure 8-9.

As physical dimensions and applied roll force were recorded after each cold rolling step, both flow stress and strain could be calculated using (7) which was discussed originally in Section 2.4. The results of this calculation, using a Q value of 1,

for the wrought Ti-6Al-4V rolled strips which were rolled via Paths C and D and are presented in Figure 9-5.

$$\bar{Y} = \frac{F}{(1.15)Q_P LW} \tag{7}$$

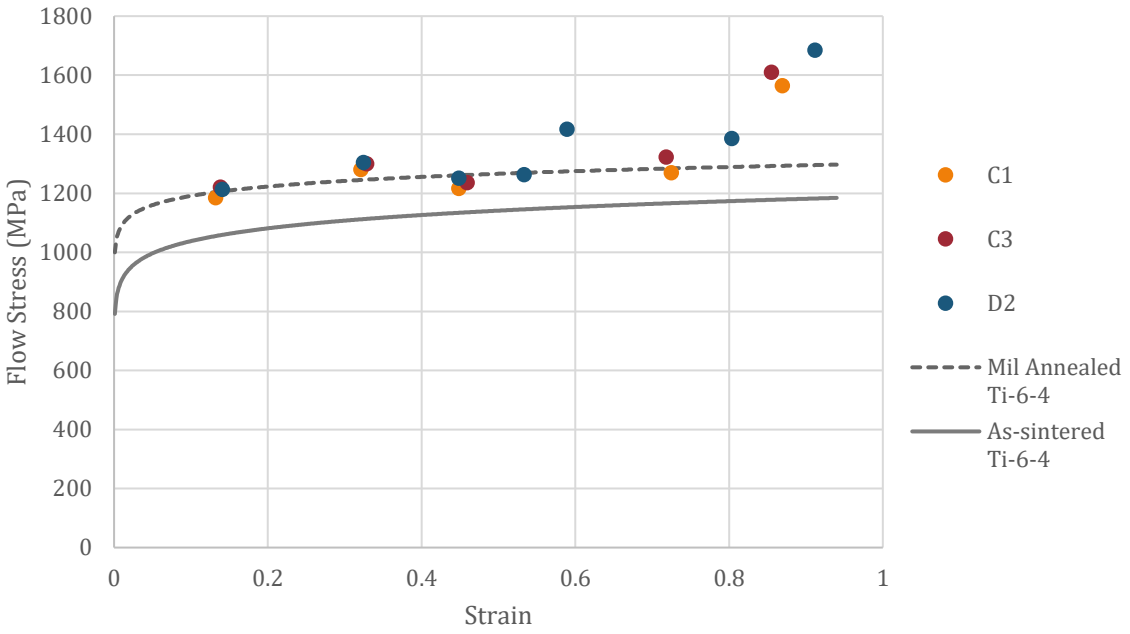


*Figure 9-5. Flow stress calculated from (7) and strain from wrought Ti-6Al-4V rolled strip data and theoretical Ti-6Al-4V flow stress using (6) using k and n values*

At lower strains, the calculations derived from experimental rolling measurements are a very good fit to the projected stress calculated via the strain hardening relationship and the mill annealed heat treatment. These calculations overestimate the flow curve for a sheet in the as-sintered state. None of the wrought samples had an intermediate annealing step. Roll Path D includes the repeat roll step, which is two additional passes at 0.05mm GW, whereas Path C proceeds directly to 0mm GW following the first roll step. The first pass following roll the first roll step continues to align with the mill anneal value whether it is part of the repeat or final step.

For all materials, the final rolling step at 0 GW diverge as observed flow stress is higher than what was calculated.

## 9.3 Cold rolling of Roll Compacted Materials

Figure 9-6 shows the flow stress-strain curve calculations using (7) from cold rolling the roll compacted samples for both alloys rolled via Paths C and D, which are the same conditions as the wrought samples in Figure 9-5. The theoretical strain hardening equation for Ti-6Al-4V is also included in the plots for reference.

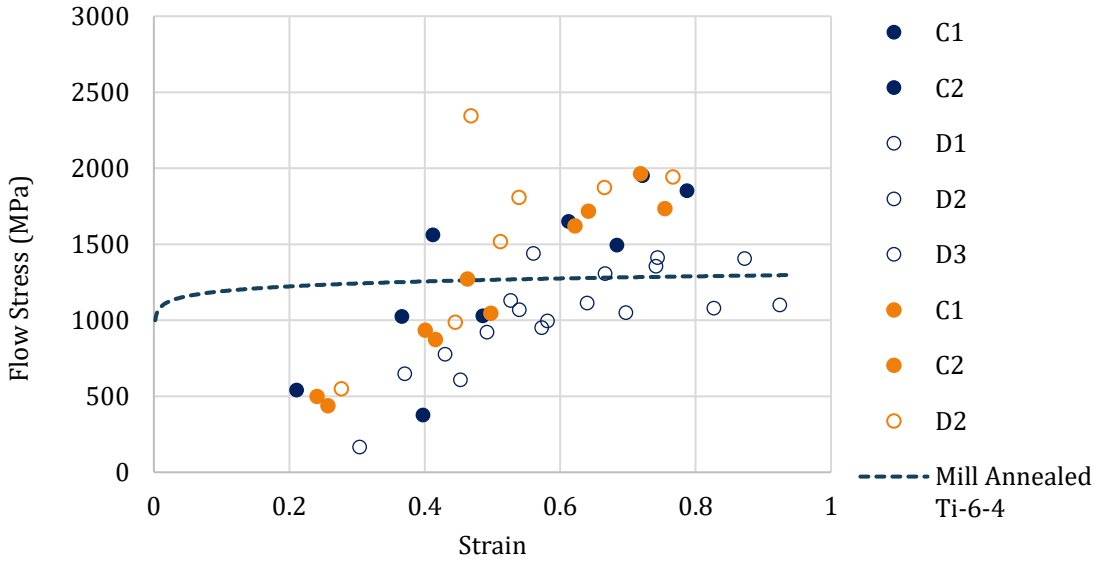


*Figure 9-6. Flow stress and strain comparison for all roll compacted samples with no intermediate annealing step (roll Paths C and D)*

Rather than following the exponential curve of the work hardening equation and the general trend of the wrought material, the roll compacted material follows a more linear upward trend. Unlike the wrought material, the roll compacted samples are not fully dense during the initial rolling passes. Sintered densities were measured between 75-85% and significant densification during the first, and sometimes into the repeat or final rolling steps occurred. This explains the lower flow stress in the roll compacted

material compared to the wrought material at low strains. At higher strains, once RC material is fully dense, it behaves similarly to the wrought material.

Figure 9-7 plots flow stress and strain data for all samples rolled via Paths B and D, which contain the repeat rolling step.

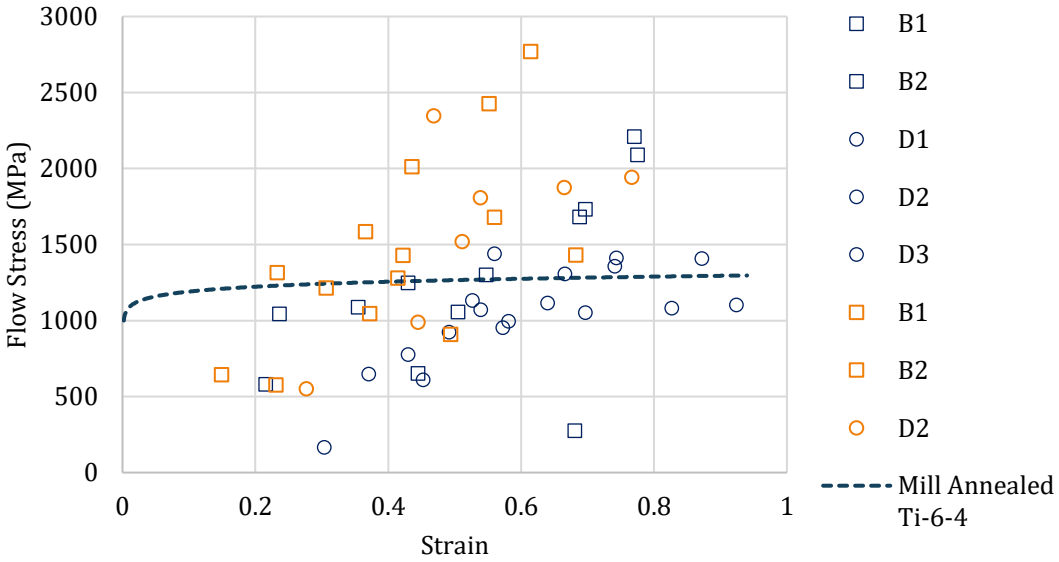


*Figure 9-7. Flow stress and strain comparison for all roll compacted samples with the repeat roll step (roll Paths B and D)*

Data is more widely scattered in this plot. The Ti-xAl-yFe alloy experiences higher flow stress and lower strains relative to the Ti-xAl-yV alloy. Additionally, annealed samples, from path B, generally experience higher flow stress compared to those from path D which were not annealed during the rolling process.

Figure 9-8 shows the samples rolled via paths A and C, which do not have the repeat rolling step. There are two distinct clusters of data belonging to the first roll step which includes one pass at 0.3 mm GW and two at 0.05 mm GW and the final roll step of two passes at 0 mm GW rolling steps respectively. The separation occurs at approximately 0.5 (or 50%) strain.

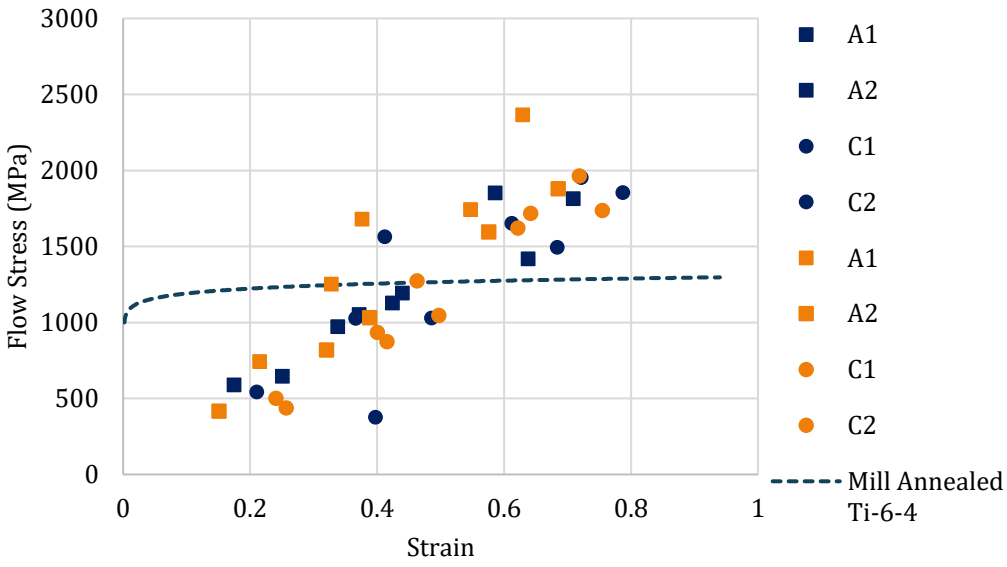


*Figure 9-8. Flow stress and strain comparison for all roll compacted samples rolled without the repeat roll step (roll Paths A and C)*

Comparing Figure 9-8 to Figure 9-7, the overall variation in this data is much less than when the repeat roll step is performed, and the correlation appears more linear. The inclusion of the repeat rolling step introduces variation of its own and potentially amplifies variation which results from alloy composition. While the other sub-sets of data diverge in the repeat and final rolling steps, this is not the case when the repeat rolling step is not performed such as in Paths A and C. Further, Path A had the intermediate anneal performed in the 50% strain gap while path C did not. Figure 9-8 indicates that the intermediate anneal has little influence over the flow behaviour developed during the final cold rolling steps. In the flow stress calculations performed using (7) were used to create Figure 9-5 through Figure 9-8, the pressure multiplication factor Q is assumed to be 1, as friction is considered to be zero. In reality, friction, although relatively low, is not zero during cold rolling.

## 9.4 Pressure Amplification

Literature cites potential ranges of friction coefficients (μ) between 0.05-0.3, and more specifically, 0.02-0.1 [27]. This section examines the effects of friction on flow stress calculations. The following schematic in Figure 9-9 plots $Q_p$ factors for a variety of μ. The three curves of 0.05, 0.1, and 0.15 are used to estimate the $Q_p$ for the purposes of this research. L/h on the x-axis is the ratio of contact length and sample height.

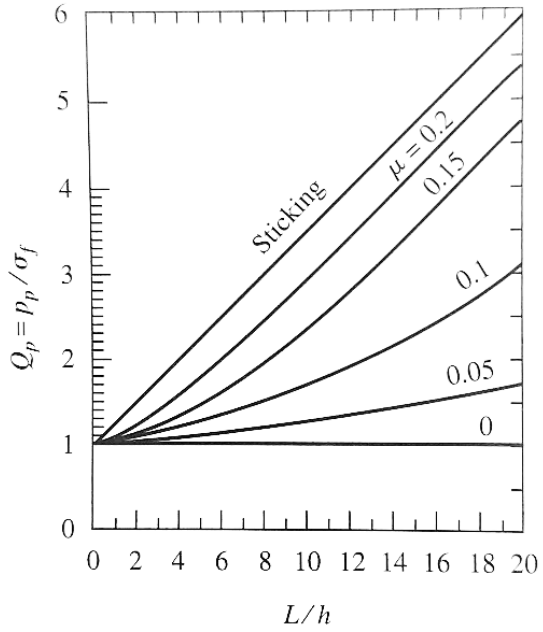


*Figure 9-9. Q and L/h for a variety of μ [56]*

The ratio of the contact length and sample thickness indicates the extent to which friction will affect the flow stress experienced by the part. As the L/h ratio increases, the pressure amplification factor, $Q$, also increases. Higher coefficients of friction between the rolls and the workpiece also increase the influence of the pressure multiplication factor.

The L/h was calculated for each roll step using experimental measurements of thickness reduction after each reduction step. Values of $Q_p$ were determined from each

of the three μ curves at the integer value of L/h. An interpolation equation was performed with the appropriate L/h bounds chosen for all three curves to obtain the $Q_p$ values. The application of the pressure multiplication factor to the flow stress equation are referred to here as *corrected*. The values presented in previous plots which negate the effects of friction are referred to as *uncorrected*. In the following sections, the wrought material and both alloys are examined. One sample of each roll condition is presented as an example.

### 9.4.1 Wrought

Figure 9-10 and Figure 9-11 show the comparisons of the pressure multiplication correction calculations in wrought Ti-6Al-4V samples for C1 and D1 respectively. The plots show the uncorrected flow stress values as previously presented, as well as the corrected calculations for the three chosen friction coefficients and stress calculations using the work hardening equation with coefficients for both mill-annealed and as-sintered microstructures for wrought Ti-6Al-4V.

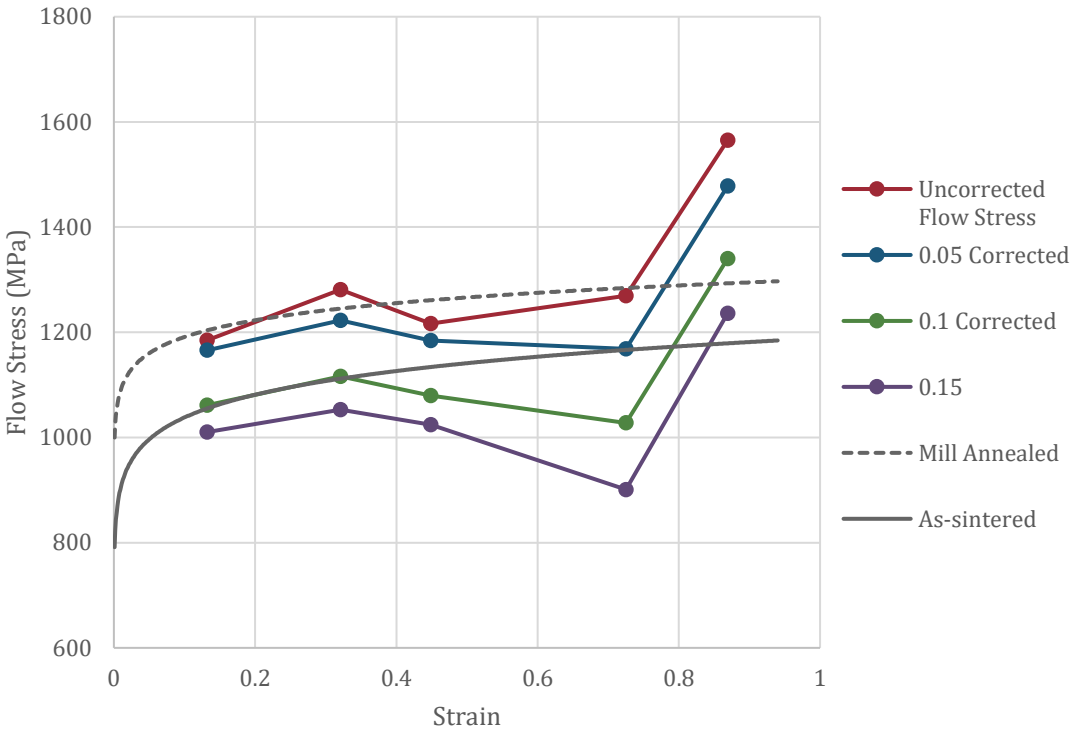


*Figure 9-10. Flow stress with pressure multiplication corrections for Wrought Ti-6-4 C1*

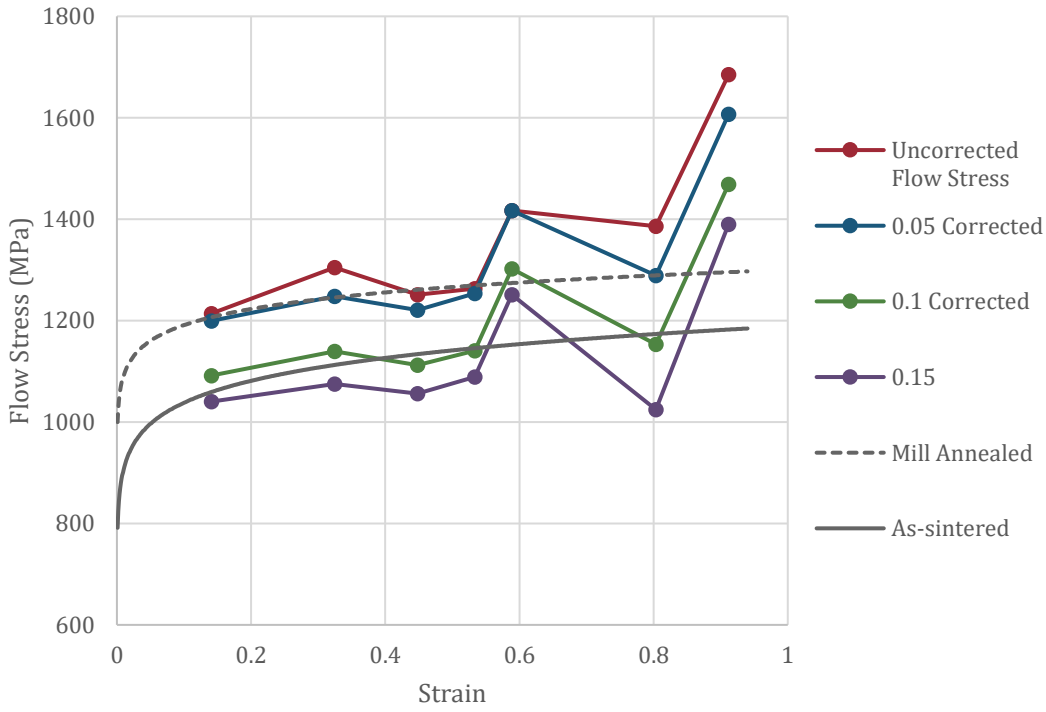


*Figure 9-11. Flow stress with pressure multiplication corrections for Wrought Ti-6-4 D1*

As previously observed in Figure 9-5, the uncorrected wrought Ti-6Al-4V flow stress very closely approximates the work hardening projection with the n and K values for mill annealed data from the literature. However, cold rolling was performed on wrought sheets in the as sintered state. It would be expected that the cold rolling calculations should more closely match the as-sintered k and n tensile test derived flow curve. Both the above figures for the C and D roll paths indicate that the use of a coefficient of friction of 0.1 most closely matches the as sintered wrought data. Therefore, using the wrought as sintered sheets as a calibration material leads to the conclusion that the coefficient of friction during cold rolling in this study is 0.1.

The second to final rolling pass is the first rolling pass with a 0GW and is also preloaded. The L/h ratio is most severe during this rolling step for all of the wrought samples. This correlates to a higher $Q_p$, especially at higher friction coefficients. Prior to this step, the material was rolled at a GW of 0.05 mm. The dip in the curve at this data point is attributed to the experimental design rather than material properties. It is hypothesized that if the gap widths had a more gradual step-down and more similar L/h through the duration of rolling that the curve would more closely approximate the exponential shape of the projected work hardening equations. Calculated L/h ratios and Q factors are given in Appendix E, along with graphed comparisons for selected roll compacted samples.

The application of the pressure multiplication correction does not correct or explain the deviation in the final rolling step of flow stress in the wrought material from the work hardening flow stress curve.

### 9.4.2 Ti-xAl-yV Roll Compaction

Figure 9-12. shows the flow stress curves with the pressure amplification corrections for a friction coefficient of μ = 0.1, as that was determined to be the most accurate from analysis of the wrought Ti-6Al-4V material. The mill annealed and as-sintered flow stress curves are also included.

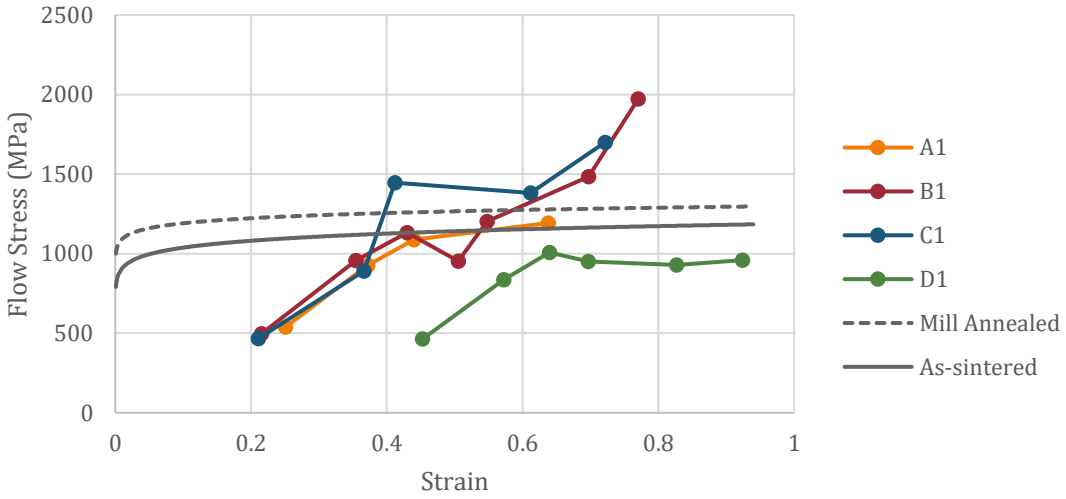


*Figure 9-12. Plot of flow stress curves for Ti-xAl-yV alloys with pressure multiplication (Q) for μ=0.1*

In the first and repeat roll passes, the flow stress in roll compacted Ti-Al-V material is lower than the work hardening flow stress curves, whereas the wrought material was in agreement. This is attributed to the densification which is occurring during those passes for roll compacted samples which does not occur in the fully dense wrought material.

In the third and fourth rolling pass of the first roll step, and both passes of the repeat roll step, the flow stress curves of the B1 sample flatten. In the final roll two passes, the flow stress is elevated compared to both the previous passes and the work hardening flow stress curves as was observed in the wrought Ti-6Al-4V material.

There does appear to be a good correlation between yield strength and flow stress where greater flow stress is observed in samples which exhibited higher YS.

The measured flow stresses of the Ti-xAl-yV D1 sample which are lower than both work hardening flow stress curves in Figure 9-12 is an outlier. It was the only strip of either wrought or roll compacted material which did not reach the flow stresses of at least the as-sintered work hardening flow stress regardless of if a pressure multiplication correction was applied. This sample did have the highest %Ti with 95.45%, where the next closest was sample C1 with 92.69%.

### 9.4.3 Ti-xAl-yFe Roll Compaction

The mill annealed and as-sintered work hardening flow stress curves are included in Figure 9-13 as well, although it should be noted that they are for Ti-6Al-4V rather than an aluminium-iron alloy. Ti-5Al-2.5Fe, which was the target composition for the Ti-xAl-yFe alloy in this research, was chosen as a potential alternative titanium alloy to Ti-6Al-4V because it is an α-β alloy with similar mechanical properties, so it is not unreasonable to estimate a similar response to rolling.

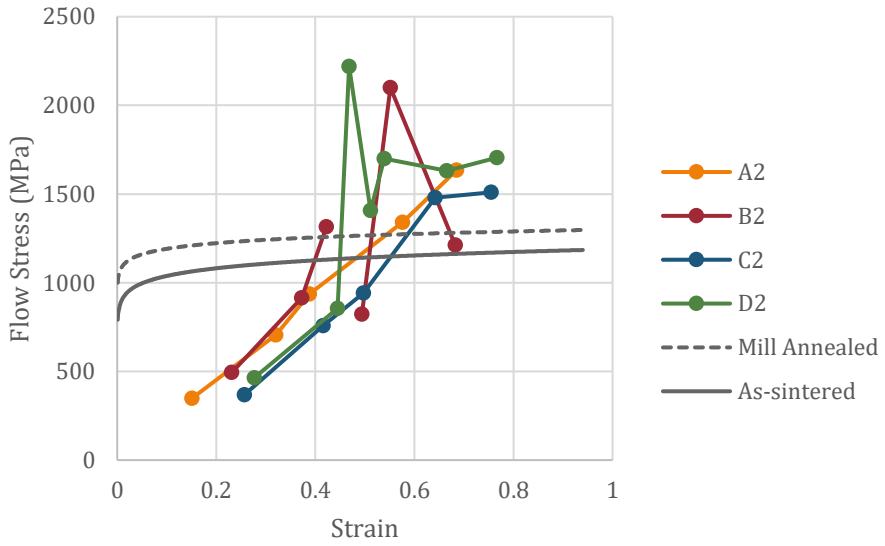

*Figure 9-13. Plot of flow stres curves for Ti-xAl-yFe alloys with a pressure amplification (Q) for μ=0.1*

A number of flow stress graphs in Ti-xAl-yFe continue to appear fully linear, even with the pressure multiplication corrections, where A2 is an example. Both occurred in samples without the repeat roll step. One interpretation of this pattern is that the Ti-xAl-yFe rolling response is not comparable to Ti-xAl-yV and that peak flow stress of Ti-xAl-yFe has not been achieved and so there is no plateau in the flow stress curve. An alternate explanation is that a plateau in data would be present at intermediate strains if there were additional rolling passes or the reduction in GW was more gradual. At high strains the up-tick measured in final rolling passes would be present as it is in Ti-6Al-4V wrought material and Ti-xAl-yV RC material for the same reason, although it is not yet known.

## 9.5 Discussion

The roll compaction flow stress measurements were consistently less than the work hardening flow stress curves or the measured values in the wrought Ti-6Al-4V samples in the first 1-2 rolling passes which is attributed to the densification of material which is occurring particularly during these rolling passes. Figure 9-14 shows a schematic comparing the general behavior of a fully dense material and a porous material. After the initial rolling passes, the roll compacted material reaches the point of full densification and behaves similarly to the fully dense wrought Ti-6Al-4V material.

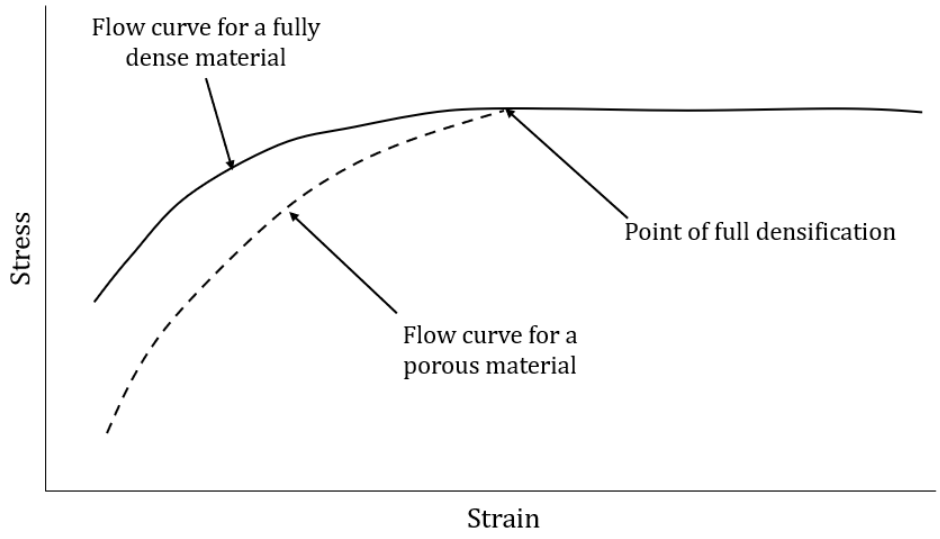


*Figure 9-14. Schematic of flow stress curves for pourus and fully dense materials*

In Figure 9-10 and Figure 9-11 which show flow stress curves for the rolled wrought material, there is one dip which occurs in the first rolling pass at 0GW, which is attributed to the experimental design. In the roll compacted samples there are more often deviations from the work hardening flow stress curves and they occur at different roll passes. All through the roll mechanics of the RC material does respond slightly less predictably than the wrought material, the general shapes of flow stress curves tend to be in agreement. It is reasonable to expect more variation in the roll compacted samples at this stage in development as there are variations in strip densities and compositions of the strips, and as a result of different roll paths.

The applied force measured by the rolling mill during each rolling pass is the maximum force. The actual force applied over the length of the strip may vary slightly. The current model also does not take the stiffness of the rolls.

# Chapter 10: Conclusions

## 10.1 Summary

The principal motivation for this study was to determine the capability of direct powder roll compaction as a production method for Ti-6Al-4V sheet or strip which would offer immense economic and environmental benefits when compared to the traditional methods of manufacturing these products. While Ti-6Al-4V is the most widely used titanium alloy, Ti-5Al-2.5Fe was also examined as an alternate α/β alloy in effort to further reduce cost of materials and improve biocompatibility while having similar mechanical properties. The initial metric used by which to determine the legitimacy of DPR in the process optimization stage was density and general microstructural categorization, then expanded to include mechanical properties obtained via tensile testing and chemical analysis later in the study.

The process optimization stage yielded strips with high densities overall and minimal density gradients for both alloys, while also providing useful information to improve quality and make the process more efficient. It was determined that one hour was an effective sintering time, and that further increasing the dwell time offered no additional densification. Other important insights include the addition of a rolling pass at 0.3mm GW in the first rolling step to reduce the thickness at a more gradual rate and changing the sintering support from zirshot material to a CP-Ti sheet comb shape. The combination of these additions reduced crack propagation from sheet edges in later rolling passes. Additionally, it was determined that benefits of the 3D printed green feeder in reducing the density gradients across the strip width were limited compared to the determent to overall powder flow and so it was not used in subsequent roll

compaction. Rolling with and without and intermediate annealing step both produced high densities and it was determined this was a variable which required further study when mechanical properties were to be considered and if its impacts would be amplified if a more aggressive path were to be used.

In the second iteration of strip production, the inclusion of the repeat rolling step which consisted of two additional passes at 0.05GW was varied, in addition to the intermediate annealing step to analyse a total of four rolling paths. Strips of wrought Ti-6Al-4V were also rolled and heat treated following two of these roll paths and were used as a benchmark for mechanical properties and to validate certain experimental procedures and analysis. Again, fully dense strips were obtained across multiple rolling paths for both alloy mixtures and the alterations to the experimental designed from the process optimization stage previously discussed were successful in improving quality of the strips produced with improved powder flow from the hopper and less severe cracking during cold rolling.

At this time, analysis of chemistry, hardness, and tensile properties were included in addition to density, and rolling response. Microstructural analysis was also expanded to include grain size analysis. LA-ICPMS and oxygen analysis were performed following the complete production and tensile testing of the material, and it was at this time that it was discovered that the target compositions of Ti-6Al-4V and Ti-5Al-2.5Fe were not achieved and that composition was varied between strips, which is why alloys have been described by Ti-xAl-yV and Ti-xAl-yFe throughout this report. While this was certainly undesirable, it does highlight the importance of powder traceability and necessity for further considerations of powder flow behavior. Since composition was

measured, the effects of varying compositions have been taken into consideration throughout the analysis. Oxygen did exceed the specifications of a Ti-6Al-4V alloy in some cases but did not approach critical levels at which severe loss of ductility occurs. It did not appear to be a function of which of the rolling paths were performed on the strip, as the primary incident occurred during the initial sintering stage which was undergone by all samples.

Alloy composition, and more specifically the presence of oxygen in the roll compacted strips has also been attributed to oxide grain pinning effects that are significant in the material's ability to resist excessive grain growth at high temperatures. Secondary to composition, elimination of the intermediate annealing step was also effective in refining the grain structure, whereas the repeat roll step had minimal impact.

Oxygen increases strength through both interstitial solid solution strengthening and grain refinement via oxide pinning. Alloying additions also offer strengthening through other mechanisms. Increased oxygen effects occur at the expense of reduced alloying additions. These competing factors made it difficult to distinguish strong trends with respect to strength and ductility as a function of roll path due to unintended variances in compositions.

Tensile strengths of the roll compacted alloys were generally comparable to the wrought material and the ductility was comparable or in some cases, far exceeded that of the wrought samples rolled under the same conditions even while oxygen content was high. UTS was inversely correlated to oxygen and UTS and ductility showed a slight inverse correlation between them. Ductility was not as greatly affected by oxygen as

was expected based on literature or the relationship between UTS and ductility. Yield strength was not highly sensitive to %Ti or grain size. Significant and offsetting impact of composition did make it difficult to discern some trends with certainty.

## 10.2 Recommendations for Future Work

### 10.2.1 Roll Compaction

One of the principal motivations of this study was to create a method of roll compaction which is more environmentally friendly. One approach by which this can be accomplished is reducing wasted material. Some suggestions for accomplishing this include creating longer strips during the compaction process, since the start and end of each strip must be discarded. The beginning includes the titanium granules that were used to prevent the free flow of powder prior to the beginning of rolling and the end of the strip is less than full width and becomes less dense. Creating longer strips reduces the amount of run-on and run-off material which becomes waste. Compaction with larger batches of powder and/or reviewing the use of the auger mechanism to control powder flow through the hopper may be avenues by which this could be achieved. The decision to work without the auger mechanism was made based on results of the CP-Ti study and similar sized batches. Flowability of the alloyed powder mixture may be different than the CP-Ti alone. The auger would potentially better regulate the powder flow when a large batch of powder is used compared to the force changing as the powder level changes in the hopper.

### 10.2.2 Composition

In next steps of the roll compacted process, a more consistent alloy composition is required, specifically achieving the target compositions of Ti-6Al-4V and Ti-5Al-2.5Fe. The potential for composition gradients throughout a single roll compacted strip

should be studied. Potential sources for the observed discrepancy are that it was a function of powder recycling or due to separation of powder in the hopper resulting from the bimodal powder size distribution.

Uncompacted powder was collected and recycled as part of the current work in an effort to conserve material. While there were no immediately apparent effects on the mechanical properties during this research other than being the potential source of composition variation, the effects should be more purposely studied in future work. To improve quality control when recycling powder, a robust powder traceability should be created.

The amount of alloying additions in the current study were lower than the target compositions. Reaching target compositions would result in a lower %Ti, and further reduce the amount of oxygen pick-up during sintering and aiding in producing material which meets Grade 5 Titanium specifications.

### 10.2.3 Cold Rolling

Being able to measure the force applied during cold rolling was advantageous in determining the rolling mechanics of the different materials. For a more thorough understanding, continuous load cell measurements across the full length of the sample should be enabled rather than a discreet measurement of maximum load.

In future stages of work, an alteration to the roll path should be considered such that there is a more gradual reduction in gap widths rather than the current roll path with more drastic reductions and repeated passes at the same gap widths.

## 10.3 Closing Remarks

There is still work to be done to improve the knowledge base and optimize the rolling parameters for titanium and titanium alloys. DPR of titanium, while still early in development has the potential to create viable engineering materials which are more environmentally and economically feasible than those currently commercially available.

# References


[1] M. J. Donachie, Jr., *Titanium: A Technical Guide*. ASM International, 2000.

[2] M. Quian and F. H. Froes, *Titanium Powder Metallurgy*. Elsevier Butterwork-Heinemann, 2015.

[3] S. M. Sapuan, N. K. Mun, A. Hambali, H. Y. Lok, A. M. Fairuz, and M. R. Ishak, "Prototype expert system for material selection of polymeric composite automotive dashboard," *Int. J. Phys. Sci.*, vol. 6, no. 25, pp. 5988–5995, 2011, doi: 10.5897/IJPS11.939.

[4] Francois Cardarelli, *Materials Handbook: A Concise Desktop Reference*, 2nd ed. London, New York, Heidelberg: Springer, 2008.

[5] S. F. Corbin, "Toward A Reduction in the Environmental Impact of Materials and Manufacturing used in Automotive and Aerospace Applications," Unpublished.

[6] H. Takebe, K. Mori, K. Takahashi, and K. Fujii, "Effects of Thickness and Grain Size on Tensile Properties of Pure Titanium Thin Gauge Sheets," *Proc. 13th World Conf. Titan.*, pp. 491–494, 2016, doi: 10.1002/9781119296126.ch77.

[7] W. H. Peter *et al.*, "Titanium sheet fabricated from powder for industrial applications," *Jom*, vol. 64, no. 5, pp. 566–571, 2012, doi: 10.1007/s11837-012-0309-1.

[8] A. A. Luo, "Advanced Light Metals and Manufacturing for Automotive Lightweighting," 2020, [Online]. Available: https://academy.cim.org/cim/2020/com-2020/309015/alan.luo.advanced.light.metals.and.manufacturing.for.automotive.lightweighting.html?f=menu%3D14%2Abrowseby%3D8%2Asortby%3D2%2Amedia%3D1%2Aspeaker%3D803417.

[9] M. Steytler and R. Knutsen, "Identifying challenges to the commercial viability of direct powder rolled titanium: A systematic review and market analysis," *Materials (Basel).*, vol. 13, no. 9, 2020, doi: 10.3390/ma13092124.

[10] A. Govender, C. Bemont, and S. Chikosha, "Sintering high green density direct powder rolled titanium strips, in argon atmosphere," *Metals (Basel).*, vol. 11, no. 6, 2021, doi: 10.3390/met11060936.

[11] S. Chikosha, T. C. Shabalala, and H. K. Chikwanda, “Effect of particle morphology and size on roll compaction of Ti-based powders,” *Powder Technol.*, vol. 264, pp. 310–319, 2014, doi: 10.1016/j.powtec.2014.05.033.

[12] N. S. Muchavi, S. Chikosha, H. K. Chikwanda, and E. M. Makhatha, “Determination of roll compaction parameters required for high green density , defect free Ti-6Al-4V strips,” *Conf. South African Adv. Mater. Initiat.*, vol. 430, 2018, doi: 10.1088/1757-899X/430/1/012026.

[13] G. Lütjering and J. C. Williams, *Titanium*, Second. Velag, Berlin, Heidburg: Springer, 2007.

[14] R. Boyer, G. Welsch, and E. W. Collings, “Classification of Titanium Alloys,” in *Materials Properties Handbook: Titanium Alloys1*, ASM International, 994.

[15] W. F. Smith, *Structure and Properties of Engineering Alloys*, 1st ed. McGraw-Hill, 1981.

[16] D. Kuroda, M. Niinomi, M. Morinaga, Y. Kato, and T. Yashiro, “Design and mechanical properties of new β type titanium alloys for implant materials,” *Mater. Sci. Eng. A*, vol. 243, no. 1–2, pp. 244–249, 1998, doi: 10.1016/s0921-5093(97)00808-3.

[17] T. Sjafrizal, A. Dehghan-Manshadi, D. Kent, M. Yan, and M. S. Dargusch, “Effect of Fe addition on properties of Ti–6Al-xFe manufactured by blended elemental process,” *J. Mech. Behav. Biomed. Mater.*, vol. 102, no. May 2019, p. 103518, 2020, doi: 10.1016/j.jmbbm.2019.103518.

[18] N. Mitsuo, “Mechanical properties of biomedical titanium alloys,” *Mater. Sci. Eng. A*, vol. 243, no. 1–2, pp. 231–236, 1998, [Online]. Available: http://www.sciencedirect.com/science/article/pii/S092150939700806X.

[19] M. O. Bodunrin, L. H. Chown, and J. A. Omotoyinbo, “Development of low-cost titanium alloys: A chronicle of challenges and opportunities,” *Mater. Today Proc.*, vol. 38, pp. 564–569, 2021, doi: 10.1016/j.matpr.2020.02.978.

[20] E. L. Rooy and J. H. L. Van Linden, “ASM Metals Handbook, Vol 02 Properties and Selection: Nonferrous Alloys and Special-Purpose Materials,” pp. 3330–3345, 1990.

[21] C. A. I. Handbook, "ASM Metals Handbook, Volume 09 Metallography and Microstrustures Handbook," *ASM Int.*, vol. 9, p. 2733, 2004, [Online]. Available: http://www.worldcat.org/oclc/42469467.

[22] R. Yamanoglu, E. Efendi, and I. Daoud, "Sintering Properties of Mechanically Alloyed Ti-5Al-2.5Fe," *Int. Sch. Sci. Res. Innov.*, vol. 11, no. 5, pp. 360–364, 2017.

[23] M. Jia, C. Blanchard, and L. Bolzoni, "Microstructure and mechanical properties of Ti-5Al-2.5Fe alloy produced by powder forging," *Key Eng. Mater.*, vol. 770 KEM, pp. 39–44, 2018, doi: 10.4028/www.scientific.net/KEM.770.39.

[24] R. P. Siqueira, H. R. Z. Sandim, A. O. F. Hayama, and V. A. R. Henriques, "Microstructural evolution during sintering of the blended elemental Ti-5Al-2.5Fe alloy," *J. Alloys Compd.*, vol. 476, no. 1–2, pp. 130–137, 2009, doi: 10.1016/j.jallcom.2008.09.004.

[25] ASM International, *Volume 7: Powder Metal Technologies and Applications*, vol. 7. ASM International, 1998.

[26] R. M. German, *Powder Metallurgy Science*. Princeton, New Jersey: Metal Powder Industries Federation, 1984.

[27] Serope Kalpakjian and S. R. Schmid, *Manufacturing Processes for Engineering Materials*, Sixth. Pearson, 2016.

[28] R. K. Dube, "Metal strip via roll compaction and related powder metallurgy routes," *Int. Mater. Rev.*, vol. 35, no. 1, pp. 253–292, 1990, doi: 10.1179/095066090790323993.

[29] J. O'Flynn and S. F. Corbin, "Effects of powder material and process parameters on the roll compaction, sintering and cold rolling of titanium sponge," *Powder Metall.*, vol. 62, no. 5, pp. 307–321, 2019, doi: 10.1080/00325899.2019.1651505.

[30] R. M. German, *Sintering Theory and Practices*. New York: John Wiley and Sons, 1996.

[31] R. M. German and A. Bose, *Injection Molding of Metals and Ceramics*. Princeton, New Jersey: Metal Powder Industries Federation, 1997.

[32] S. Kang and L. Suk-Joong, "Sintering Processes," in *Sintering Densification, Grain Growth, and Microstructure*, Amsterdam: Elsevier Butterwork-Heinemann, 2005, pp. 3–8.

[33] R. M. German, *Sintering: From Empirical Observations to Scientific Principals*, 1st ed. Waltham: Elsevier Butterwork-Heinemann, 2012.

[34] R. Goodall, J. F. Despois, and A. Mortensen, "Sintering of NaCl powder: Mechanisms and first stage kinetics," *J. Eur. Ceram. Soc.*, vol. 26, no. 16, pp. 3487–3497, 2006, doi: 10.1016/j.jeurceramsoc.2005.12.020.

[35] M. Momeni, C. Gierl, and H. Danninger, "Study of the oxide reduction and interstitial contents during sintering of different plain carbon steels by in situ mass spectrometry in nitrogen atmosphere," *Mater. Chem. Phys.*, vol. 129, no. 1–2, pp. 209–216, 2011, doi: 10.1016/j.matchemphys.2011.03.076.

[36] M. Groover, "Fundementals of Modern Manufacturing Materials,Processes and Systems," *John Wiley Sons*, p. 493, 2010.

[37] G. D. Mistry and K. B. Judal, "Literature review of the stress, strain and separating force evaluation during hot bar rolling of different types of steels," *Mater. Today Proc.*, vol. 57, pp. 636–642, 2022, doi: 10.1016/j.matpr.2022.02.058.

[38] G. Steedman, S. F. Corbin, and J. O'Flynn, "Distinguishing the influence of aluminium and vanadium additions on microstructural evolution and densification behaviour during the sintering of ti6Al, ti4V and ti6al4v," *Powder Metall.*, vol. 61, no. 4, pp. 301–312, 2018, doi: 10.1080/00325899.2018.1501946.

[39] G. Steedman and S. F. Corbin, "Determining sintering mechanisms and rate of in situ homogenisation during master alloy sintering of Ti6Al4V," *Powder Metall.*, vol. 58, no. 1, pp. 67–80, 2015, doi: 10.1179/1743290114Y.0000000110.

[40] J. O'Flynn and S. F. Corbin, "The influence of iron powder size on pore formation, densification and homogenization during blended elemental sintering of Ti-2.5Fe," *J. Alloys Compd.*, vol. 618, pp. 437–448, 2015, doi: 10.1016/j.jallcom.2014.08.134.

[41] B. Peiraggi, "Diffusion of Solid State Reactions," in *Developments in High Temperature Corrosion and Protection of Materials*, Woodhead Publishing, 2008, pp. 9–35.

[42] R. W. Cooke *et al.*, "The influence of sintering atmosphere on the processing and properties of comercially pure titanium components," Unpublished, 2013.

[43] N. S. Muchavi, S. Chikosha, H. K. Chikwanda, and E. M. Makhatha, "Determination of roll compaction parameters required for high green density , defect free Ti-6Al-4V strips," *Conf. South African Adv. Mater. Initiat.*, vol. 430, no. 1, Oct. 2018, doi: 10.1088/1757-899X/430/1/012026.

[44] H. B. Kaufman, *Cold Rolling of Roll Compacted Titanium Sponge*. 2019, Unpublished.

[45] MEC at Dalhousie University, "ADMA CP-Ti and AlV MA Powder Size Analysis." Unpublished .

[46] J. Lapointe, "Influence of Blended Elemental Aluminum and Titanium-Aluminum Master Alloy Additions on the Sintering Behaviour of Titanium-6 Aluminum Alloy," 2016.

[47] MEC at Dalhousie University, "Fe Powder Analysis." 2013, Unpublished.

[48] S. Preibisch, S. Saalfeld, and P. Tomancak, "Globally optimal stitching of tiled 3D microscopic image acquisitions," *Bioinformatics*, vol. 25, no. 11, pp. 1463–1465, 2009, doi: 10.1093/bioinformatics/btp184.

[49] J. Schindelin *et al.*, "Fiji: An open-source platform for biological-image analysis," *Nat. Methods*, vol. 9, no. 7, pp. 676–682, 2012, doi: 10.1038/nmeth.2019.

[50] ASTM International, "Standard Test Methods for Determining Average Grain Size," *Astm E112-10*. pp. 1–27, 2010, doi: 10.1520/E0112-13.1.4.

[51] ASTM E8, "ASTM E8/E8M standard test methods for tension testing of metallic materials," *Annu. B. ASTM Stand. 4*, vol. 9, no. C, pp. 1–27, 2010, doi: 10.1520/E0008.

[52] H. Conrad, M. Swintowski, and S. L. Mannan, "Effect of cold work on recrystallization behavior and grain size distribution in titanium," *Metall. Trans. A*, vol. 16, no. 5, pp. 703–708, 1985, doi: 10.1007/BF02814821.

[53] Q. He *et al.*, "Effect of cold rolling reduction on grain growth kinetics of TB8 titanium alloy during annealing heat treatment," *Mater. Res. Express*, vol. 6, no. 11, 2019, doi: 10.1088/2053-1591/ab4af2.

[54] R. Jones, "Rolling Deformation Schematic," *An overview of metals processing methods | Materials Properties*, 2020. .

[55] TIMET, “Titanium Metals Corperation Approved Certificate 0.063" SQ Sheet,” Toronto, OH, 2020.

[56] J. A. Schey, *Introduction to Manufacturing Processes*. McGraw-Hill, 2000.

[57] W. D. Callister and D. G. Rethwisch, *Materials Science and Engineering: An Introduction*, Seventh. John Wiley and Sons, 2007.

[58] R. Rajendran, M. Venkateshwarlu, V. Petley, and S. Verma, “Strain hardening exponents and strength coefficients for aeroengine isotropic metallic materials – a reverse engineering approach,” *J. Mech. Behav. Mater.*, vol. 23, no. 3–4, pp. 101–106, 2014, doi: 10.1515/jmbm-2014-0012.

# Appendix A: Microstructure as a Function of Sintering Time

The Ti-xAl-yV alloy was produced by mixing ADMA CP-Ti Grade 5 sponge powder and an Al:V master alloy. The MA particles had a blocky, irregular shape and appear bright white after etching as noted in Figure A1. The contact points between MA and CP-Ti powder became highly alloyed and results in an extremely fine Widmanstätten structure as shown in Figure A2. Further away from these contact points, the plates became wider.

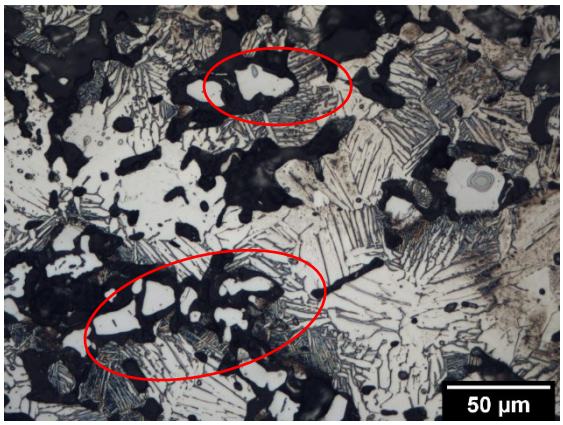


*Figure A1. MA particles in a roll compacted Ti-xAl-yV sample sintered for 30 minutes at 1200 °C*

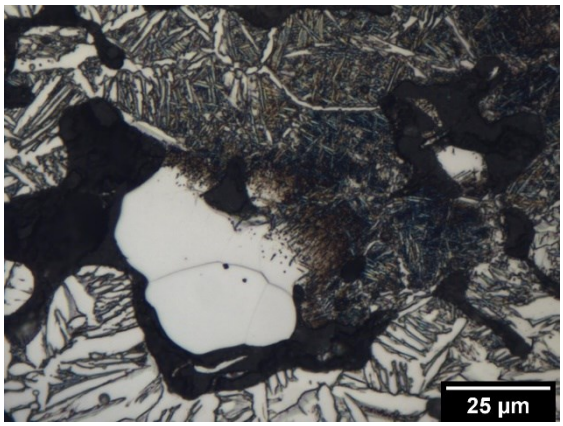


*Figure A2. Contact between MA and CP-Ti powder in Ti-xAl-yV alloy after 30 minute hold at 1200 °C*

Figure A3 shows a series of micrographs obtained from roll compacted samples of Ti-xAl-yV sintered with varying hold times at 1200°C from 0-120 minutes. MA

particles are clearly visible with hold times of 0-30 minutes (a, b). With no hold, some regions appear unalloyed or lightly infiltrated Al and V while others have a very fine Widmanstätten structure indicating a high content of the alloying elements. As time progresses, the microstructure becomes more homogeneous, and the plate widths become more consistent.

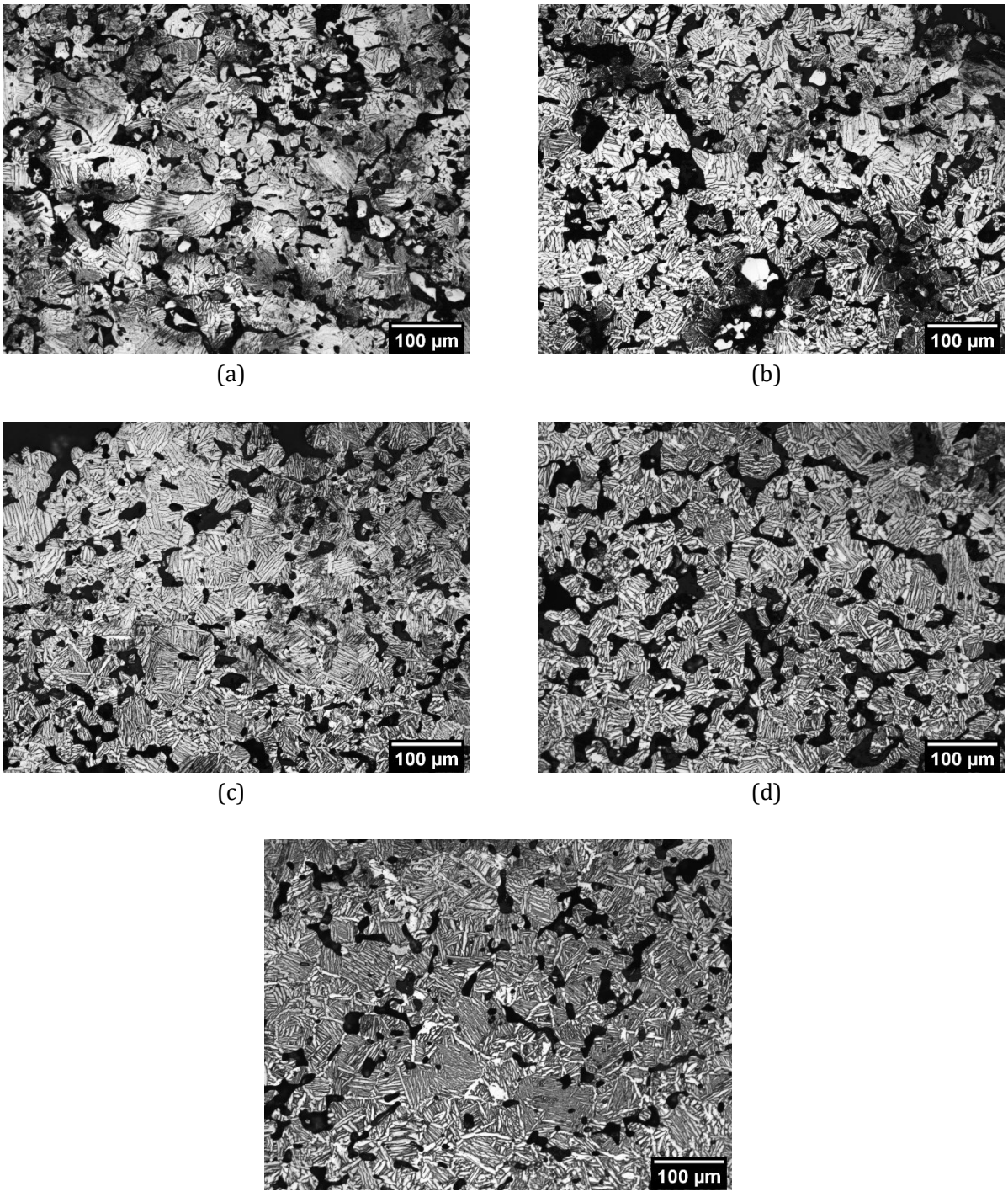


(a) (b)

(c) (d)

(e)

*Figure A3. Samples of roll compacted Ti-xAl-yV strips without feeder sintered at 1200°C or a range of times (a) 0min (b) 30min (c) 60min (d) 90min (e) 120min*

The Ti-xAl-yFe alloy was prepared by mixing three elemental powders: CP-Ti, Al, and Fe. When sintered, no aluminium particles remain in the microstructure as the melting point of the elemental powder occurs at 660°C. The rate of diffusion of iron in titanium is significantly faster than that of titanium in iron. In previous works by O'Flynn et. al on die pressed and sintered Ti-2.5Fe compacts, the Ti-Fe eutectic reaction was observed to occur. Insipient melting at 1092°C which further increased diffusion as rates are higher through a liquid than through a solid. Above 1094°C, pores were observed where iron particles had been. A region of β-Ti was observed around these pores with no isothermal hold due to the increased alloying content that had not yet diffused. There are still iron particles which remain at hold times as long as 90min, as shown in Figure A4. This is attributed to lower green density and fewer contact points of particles in the roll compacted components compared to the die pressed Ti-2.5Fe study.

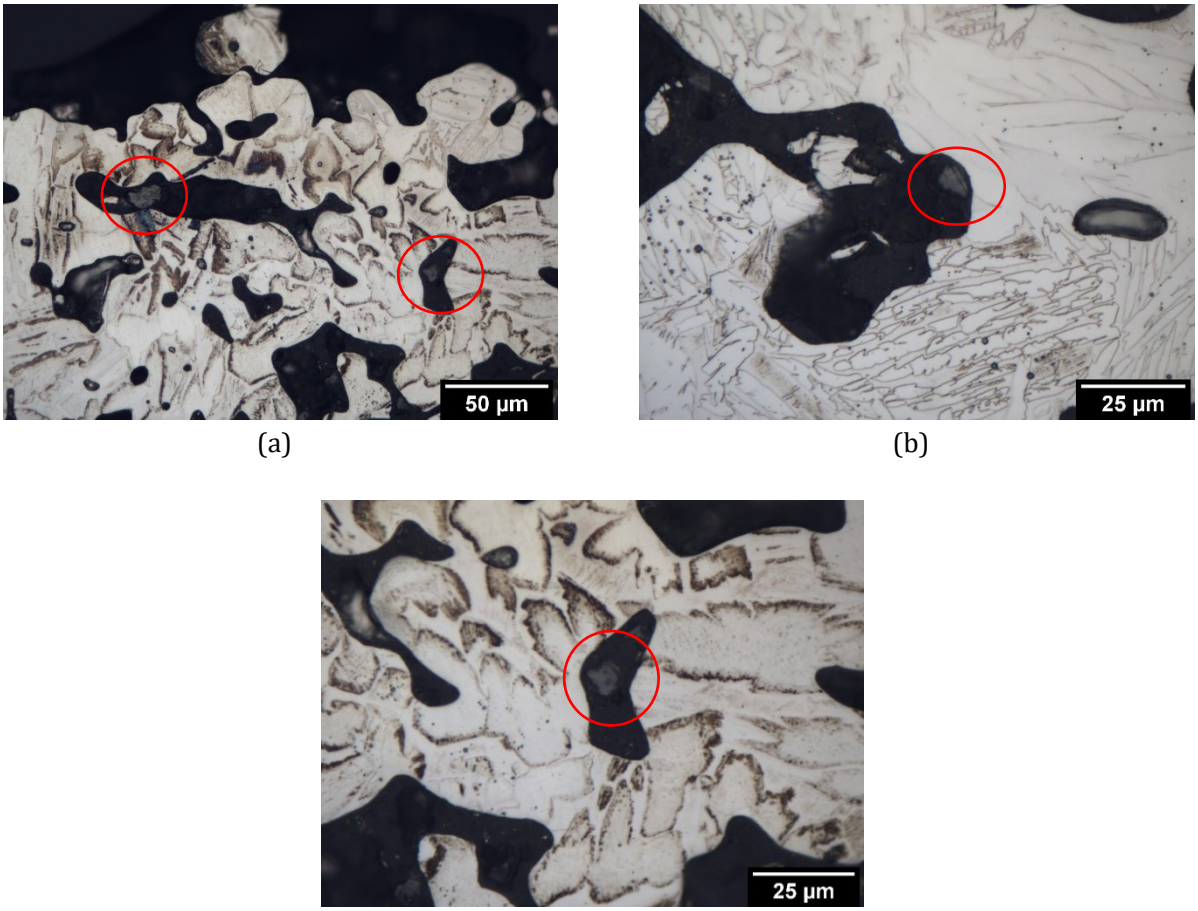


(a) (b)

*Figure A4. Sample of roll compacted Ti-xAl-yFe sintered with a 90 minute isothermal hold at the 1200 °C sintering temperature*

Figure A5. shows the samples of roll compacted Ti-xAl-yFe sintered with a range of hold times from 0-120 minutes. The size of the plates in Ti-xAl-yFe is consistently less homogeneous compared to the Ti-xAl-yV counterpart sintered for the same amount of time. The shape of the plates observed in the Ti-xAl-yFe are often more rounded and less needle like than the Ti-xAl-yV as in the pressed and sintered DIL samples. Lower observed densities in these micrographs correlate to the measured values.

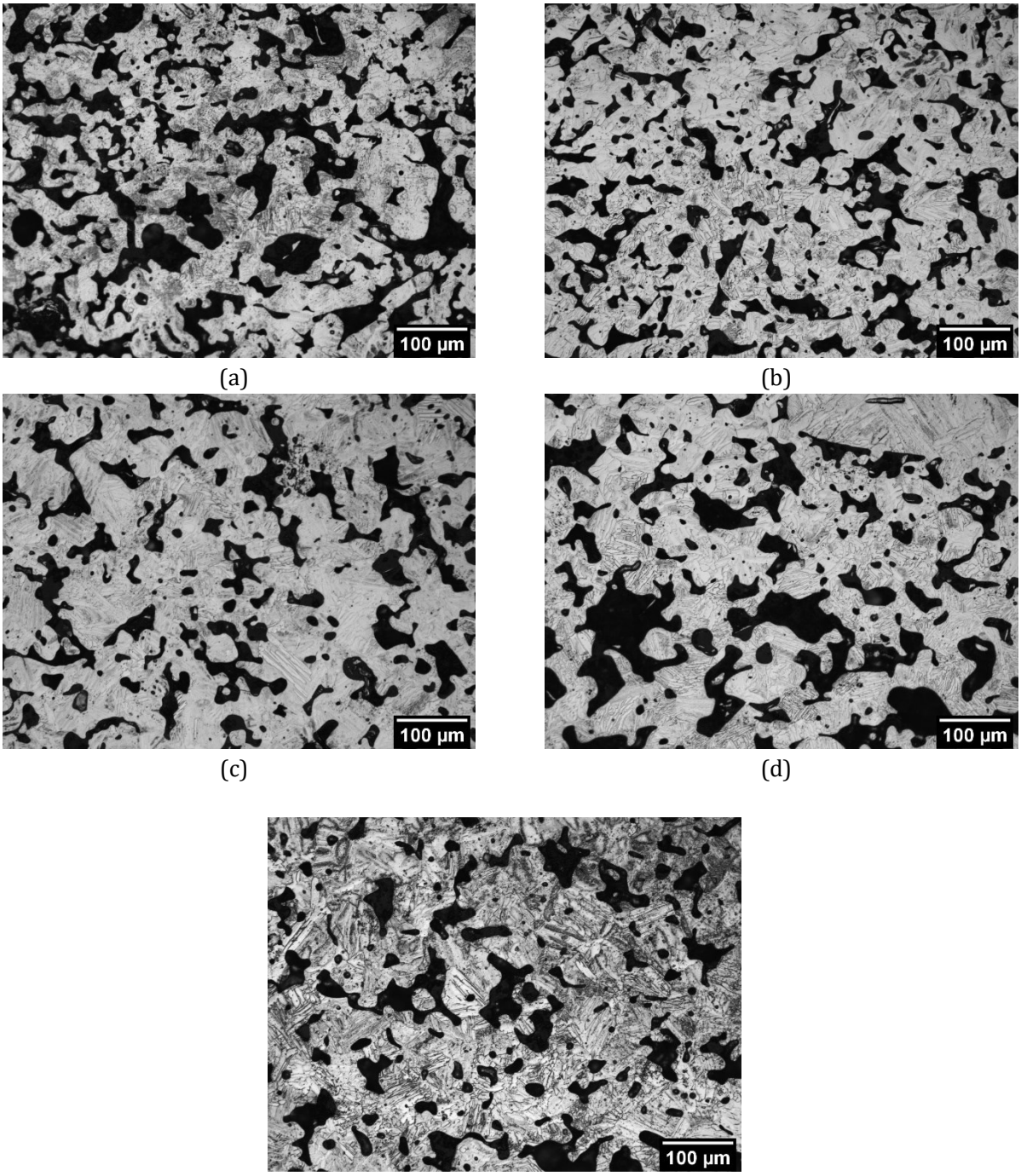


*Figure A5. Samples of roll compacted Ti-xAl-yFe strips without feeder sintered at 1200°C at (a) 0min (b) 30min (c) 60min (d) 90min and (e) 120min*

# Appendix B: Dilatometry and Densification Discussion

Separate dilatometry samples from the compaction study were created by pressing approximately 600mg of the Ti-xAl-yV powder mixture; cylindrical parts produced had a diameter of 6.37mm and were approximately 6.75mm long. A small amount of Licowax C was used as a die wall lubrication to reduce die-wall friction. The DIL samples were pressed to 120MPa using the *Carver Laboratory* manual hydraulic press. This pressure was chosen as the resulting green density most closely matches that of a roll compacted green strip.

A *Netzsch 402 C* dilatometer was used. Alumina disks and platform were used to hold the titanium sample in place. The DIL chamber was evacuated once and refilled, then evacuated again to a minimum pressure of $10^{-5}$ mbar prior to beginning the test. A piece of Ti foil was placed before the sample in the chamber to act as an oxygen getter. Under a flowing argon atmosphere of 50ml/min, samples were heated at 10K/min to 100°C, 20K/min to 1200°C and held isothermally for 3 hours before being cooled to room temperature at 40K/min. A 2h hold was added at room temperature to ensure that the chamber was able to reach room temperature prior to stopping argon gas flow. A correction was performed with a 6mm alumina cylinder using the above methodology prior to running samples.

Three samples of the Ti-xAl-yV alloy were compacted using a manual hydraulic press, and die and punch to a pressure of 120MPa. In Figure, the relative change in the sample length for each sample is plotted as a function of time, the dotted lines show the heat profile in degrees Celsius which remain consistent between samples.

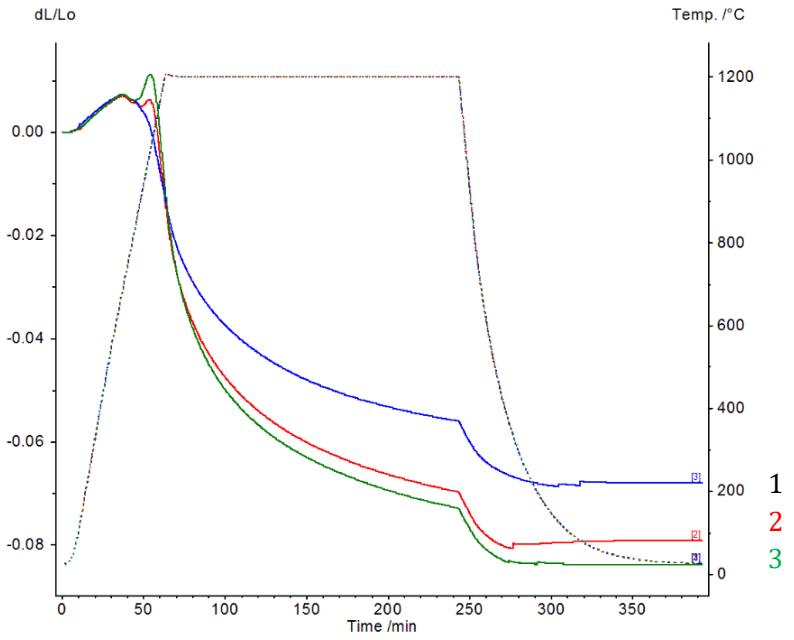


*Figure B1. Dilatometry of Ti-xAl-yV samples compacted at 120MPa*

There is some variation between measurements observed during the event which occurs at approximately 50 minutes, which corresponds with the onset of the BTT of 890°C. Possible reasons identified include normal variations in sample composition of a mixed powder, pressure applied in a manual process, and difference between starting length of the sample and the standard alumina cylinder used for the correction run. The most likely reason seems to be the progressively cleaner atmosphere as the furnace was used more regularly at high temperatures with a flowing argon atmosphere and titanium getter after a period of rest with valves open to the atmosphere. Oxygen is a β-stabilizing element; its presence in higher quantities during earlier testing would result in the β-transformation taking place over a greater temperature range and the resulting expansion occurring concurrently with densification and shrinkage of sintering. With a progressively cleaner atmosphere, the transformation takes place over a shorter temperature range closer to the cited BTT of CP-Ti and prior to sintering.

The optical density measurements presented in Figure 6-4 are discrete measurements on different materials, each sintered for a different amount of time, while the DIL results in Figure B.1 are a continuous measurement throughout the duration of sintering. Looking more specifically at the densification behavior during the isothermal hold as reported by the DSC, the curve is smooth and the change in length is consistently decreasing. While change in length cannot be entirely equivalated to densification, there does not appear to be any de-densification or expansion between 1 and 2 hours as could be suggested by the 90-minute DSC results.

Samples for DSC testing were produced by cutting a cross section of the full width of a roll compacted strip, which was then sectioned into smaller rectangular pieces which could fit in the DSC crucible. While the edges were discarded, there is potential for a density gradient across the width of the green strip. While unlikely, it is possible that the three samples used for the 90-minute sintering trials had a lower green density which translated into a lower sintered density. Order of testing is not the source of error in this case; the five samples belonging to each series were tested consecutively. Within each series, the order of testing was randomized. The other potential source of error occurs during density measurements using the *Fiji ImageJ* software. The image is transformed to a binary, where the light region corresponds with the unetched titanium, and the dark is porosity, and the area fraction is calculated. The resolution of the measurement is limited to that of the camera which takes the micrographs. Should there be a pore, defect, carbide, etc. which is appears dark and present in a higher quantity with a 90-minute sintering hold, this would be counted as porosity as artificially decrease the density measured.

# Appendix C: Evolution of Density in Set 2 Samples

Optical density measurements were performed mounted and polished cross sections after each rolling at heat treatment step. Green and sintered samples were cold mounted in epoxy due to low density. Samples from the first roll step and forward were mounted in bakelite. The results for Ti-xAl-yV samples are presented in Table C1 and Ti-xAl-yFe in Table C2.

*Table C1. Optical denity measurements in Ti-xAl-yV cross sections after each heat treatment and rolling step*

| Sample ID | Green | Sintered | Step 1 | Intermediate Anneal | Step 2 | Step 3 | Final Anneal |
|---|---|---|---|---|---|---|---|
| **A1** | 75.77 | 79.65 | 96.62 | 97.14 | – | 99.57 | 99.33 |
| **A2** | 63.61 | 74.78 | 96.87 | 97.44 | – | 99.69 | 99.57 |
| **B1** | 63.85 | 77.46 | 98.63 | 98.93 | 98.74 | 99.82 | 99.17 |
| **B2** | 63.61 | 75.73 | 98.81 | 98.88 | 99.35 | 98.35 | 99.18 |
| **C1** | 63.61 | 79.06 | 96.83 | – | – | 97.35 | 98.74 |
| **C2** | 80.88 | 76.36 | 98.98 | – | – | 99.93 | 99.54 |
| **D1** | 75.77 | 81.43 | 97.26 | – | 97.10 | 98.34 | 99.22 |
| **D2** | 68.56 | 84.92 | 97.98 | – | 98.31 | 98.30 | 99.09 |
| **D3** | 72.75 | 78.82 | 96.92 | – | 96.67 | 98.74 | 98.98 |

*Table C1. Optical denity measurements in Ti-xAl-yFe cross sections after each heat treatment and rolling step*

| Sample ID | Green | Sintered | Step 1 | Intermediate Anneal | Step 2 | Step 3 | Final Anneal |
|---|---|---|---|---|---|---|---|
| **A1** | 75.67 | 75.33 | 93.95 | 95.87 | – | 99.50 | 98.78 |
| **A2** | 84.44 | 78.67 | 96.32 | 96.86 | – | 98.41 | 98.89 |
| **B1** | 75.67 | 75.33 | 94.88 | 96.44 | 97.14 | 99.27 | 98.71 |
| **B2** | 89.44 | 78.23 | 95.48 | 98.77 | 98.52 | 98.91 | 98.98 |
| **C1** | 78.62 | 75.68 | 94.33 | – | – | 98.42 | 98.57 |
| **C2** | 84.44 | 76.25 | 97.20 | – | – | 99.15 | 98.55 |
| **D2** | 89.44 | 79.15 | 97.47 | – | 98.29 | 98.24 | 99.15 |

# Appendix D: Calculation of Work Hardening Coefficients

The strain hardening coefficient ($n$) and strength coefficient ($K$) that are used in the work hardening (6) were calculated from the experimentally collected tensile data for the as-sintered wrought Ti-6Al-4V sample.

The first step in calculating these values was to create a plastic stress-strain curve which was accomplished by subtracting the linear elastic region of the stress-strain curve for the material which was presented in Section 8.4.1. These values are the engineering stress and engineering strain.

The next step was to calculate the true stress ($\sigma_{true}$) and true strain ($\varepsilon_{true}$) values for the plastic region using the following equations:

$$\sigma_{true} = \sigma\,(1 + \varepsilon) \tag{15}$$

$$\varepsilon_{true} = \ln(1 + \varepsilon) \tag{16}$$

The logarithmic values of both $\sigma_{true}$ and $\varepsilon_{true}$ values were then obtained and plotted in Figure D1.

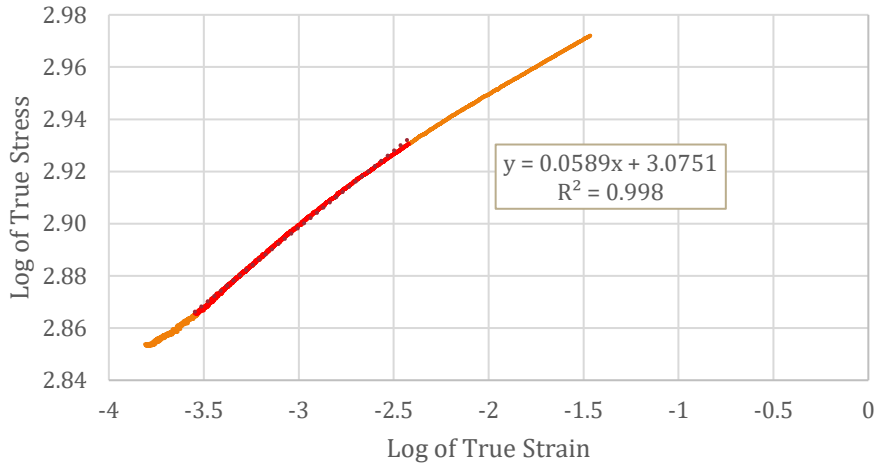


*Figure D1. Plot of logarithmic value of true stress and logarithmic value of true strain from as-sintered wrought Ti-6Al-4V sample tensile data*

A middle section of the data was chosen to be certain to avoid any possibility of elasticity or necking and is highlighted in red. A linear line of best fit was overlayed to this data selection which can be described by the equation:

$$y = 0.0589x + 3.0751 \quad (16)$$

The slope of the linear equation represents the strain hardening coefficient, *n.* The y intercept of 3.0751 is the logarithmic value of *K*. The value of K was determined to be 1188.8MPa.

$$K = 10^{3.0751} = 1188.8\ MPa \quad (17)$$

# Appendix E: Pressure Amplification Corrections

Thickness and width measurements were obtained with calipers and a digital micrometer following each cold rolling pass for all samples. The contact length between the strip and rolls could then be calculated using the following equation:

$$L = \sqrt{R\Delta t} \tag{5}$$

Table E1 and Table E2 show the measured thicknesses, calculated L and L/h, and flow stress, and estimated Q values for the Ti-xAl-yV and Ti-xAl-yFe alloys respectively.

*Table E1.Thickness, contact length, and pressure amplification corrections for selected Ti-xAl-yV samples with a range of friction coefficients*

| Sample | Thickness | L | L/h | Uncorrected Flow Stress | $Q_{0.05}$ | $Q_{0.10}$ | $Q_{0.15}$ |
|---|---|---|---|---|---|---|---|
| **A1** | 1.04 | 4.05 | 3.91 | 644.65 | 1.07 | 1.20 | 1.34 |
| | 0.97 | 2.61 | 2.70 | 1051.40 | 1.03 | 1.13 | 1.20 |
| | 0.97 | 1.86 | 1.92 | 1192.62 | 1.00 | 1.10 | 1.14 |
| | 0.79 | 2.99 | 3.77 | 1417.90 | 1.07 | 1.19 | 1.32 |
| **B1** | 1.19 | 3.95 | 3.32 | 579.89 | 1.06 | 1.17 | 1.26 |
| | 1.03 | 2.81 | 2.71 | 1088.38 | 1.04 | 1.14 | 1.20 |
| | 0.96 | 1.95 | 2.04 | 1246.88 | 1.00 | 1.10 | 1.15 |
| | 0.89 | 1.89 | 2.12 | 1054.82 | 1.00 | 1.11 | 1.16 |
| | 0.85 | 1.37 | 1.61 | 1299.85 | 1.00 | 1.08 | 1.12 |
| | 0.73 | 2.46 | 3.34 | 1731.64 | 1.06 | 1.17 | 1.26 |
| | 0.68 | 1.63 | 2.39 | 2208.69 | 1.02 | 1.12 | 1.18 |
| **C1** | 1.11 | 3.58 | 3.21 | 541.87 | 1.06 | 1.16 | 1.25 |
| | 0.95 | 2.86 | 3.00 | 1025.87 | 1.05 | 1.15 | 1.22 |
| | 0.91 | 1.47 | 1.62 | 1562.85 | 1.00 | 1.08 | 1.12 |
| | 0.75 | 2.90 | 3.90 | 1651.20 | 1.07 | 1.19 | 1.34 |
| | 0.67 | 1.98 | 2.97 | 1952.02 | 1.05 | 1.15 | 1.22 |
| **D1** | 0.96 | 5.30 | 5.51 | 609.22 | 1.11 | 1.31 | 1.55 |
| | 0.85 | 2.35 | 2.76 | 952.49 | 1.04 | 1.14 | 1.20 |
| | 0.80 | 1.68 | 2.11 | 1114.23 | 1.01 | 1.11 | 1.16 |
| | 0.75 | 1.50 | 1.99 | 1051.72 | 1.00 | 1.11 | 1.16 |
| | 0.66 | 2.16 | 3.27 | 1080.94 | 1.06 | 1.16 | 1.26 |
| | 0.60 | 1.77 | 2.95 | 1101.77 | 1.05 | 1.15 | 1.22 |

Only homogeneous rolling is examined as very few passes did not satisfy the condition of $\frac{t_f}{L} < 1$. In the table, when the condition Q is not estimated, and that data point is excluded from any plots.

*Table E2.Thickness, contact length, and pressure amplification corrections for selected Ti-xAl-yFe samples with a range of friction coefficients*

| Sample | Thickness | L | L/h | Uncorrected Flow Stress | $Q_{0.05}$ | $Q_{0.10}$ | $Q_{0.15}$ |
|---|---|---|---|---|---|---|---|
| A2 | 1.11 | 4.30 | 3.89 | 415.86 | 1.07 | 1.19 | 1.34 |
| | 0.93 | 2.97 | 3.18 | 817.39 | 1.05 | 1.16 | 1.24 |
| | 0.87 | 1.77 | 2.03 | 1030.53 | 1.00 | 1.10 | 1.15 |
| | 0.72 | 2.76 | 3.82 | 1595.52 | 1.07 | 1.19 | 1.33 |
| | 0.65 | 1.95 | 3.01 | 1880.09 | 1.05 | 1.15 | 1.22 |
| | 0.63 | 0.65 | 1.02 | 5120.41 | 1.00 | 1.05 | 1.08 |
| B2 | 1.07 | 3.56 | 3.33 | 575.61 | 1.06 | 1.17 | 1.26 |
| | 0.93 | 2.68 | 2.88 | 1045.88 | 1.04 | 1.14 | 1.21 |
| | 0.88 | 1.52 | 1.72 | 1428.69 | 1.00 | 1.09 | 1.13 |
| | *0.82* | *0.77* | *0.93* | *2025.38* | - | - | - |
| | 0.78 | 1.59 | 2.05 | 907.68 | 1.00 | 1.10 | 1.15 |
| | 0.68 | 1.53 | 2.25 | 2336.26 | 1.01 | 1.11 | 1.17 |
| | 0.64 | 2.20 | 3.45 | 1421.53 | 1.06 | 1.17 | 1.28 |
| C2 | 1.12 | 4.20 | 3.75 | 437.96 | 1.07 | 1.19 | 1.32 |
| | 0.96 | 2.90 | 3.03 | 873.27 | 1.05 | 1.15 | 1.22 |
| | 0.88 | 1.96 | 2.22 | 1046.44 | 1.01 | 1.11 | 1.17 |
| | 0.76 | 2.46 | 3.22 | 1717.12 | 1.06 | 1.16 | 1.25 |
| | 0.68 | 2.04 | 2.99 | 1735.09 | 1.05 | 1.15 | 1.22 |
| D2 | 1.14 | 4.22 | 3.70 | 549.89 | 1.07 | 1.19 | 1.31 |
| | 0.96 | 3.00 | 3.11 | 987.96 | 1.05 | 1.16 | 1.23 |
| | 0.94 | 1.06 | 1.13 | 2345.33 | 1.00 | 1.06 | 1.08 |
| | 0.90 | 1.42 | 1.58 | 1518.46 | 1.00 | 1.08 | 1.12 |
| | 0.88 | 1.12 | 1.27 | 1808.31 | 1.00 | 1.06 | 1.10 |
| | 0.77 | 2.30 | 2.98 | 1874.35 | 1.05 | 1.15 | 1.22 |
| | 0.70 | 1.95 | 2.79 | 1942.96 | 1.04 | 1.14 | 1.21 |